Controlling Nanostructures of Globular Protein-Polymer Block Copolymers in Bulk Solutions and in Thin Films

by

Dongsook Chang

B.S. Chemical and Biological Engineering, Seoul National University, 2006
M.S. Interdisciplinary Program in Bioengineering, Seoul National University, 2008

Submitted to the Department of Chemical Engineering
in partial fulfillment of the requirements for the degree of

Doctor of Philosophy in Chemical Engineering

at the

MASSACHUSETTS INSTITUTE OF TECHNOLOGY

December 2015 [February 2016]

Signature of Author: ______________________ Signature redacted
Department of Chemical Engineering
December, 2015

Certified by: ______________________________ Signature redacted
Bradley D. Olsen
Associate Professor of Chemical Engineering
Thesis Supervisor

Accepted by: ____________________ Signature redacted
Richard D. Braatz
Professor of Chemical Engineering
Chairman, Departmental Committee on Graduate Students

Controlling Nanostructures of Globular Protein-Polymer Block Copolymers in Bulk Solutions and in Thin Films

Dongsook Chang

Submitted to the Department of Chemical Engineering on December 4, 2015
in partial fulfillment of the requirements of the degree of
Doctor of Philosophy in Chemical Engineering

Abstract

The self-assembly of globular protein-polymer diblock copolymers represents a promising technology for protein nanopatterning. The self-assembled materials have a high density of proteins and internal nanostructures that serve as continuous transport pathways for substrates, products, cofactors, and/or charges. The polymer block can act as a protective matrix for the protein, improving its stability and longevity in materials. The self-assembly of protein-polymer diblock copolymers is substantially different from that of traditional synthetic diblock copolymers due to the globular and rigid shape, heterogeneous composition, and anisotropic interactions of proteins. This thesis focuses on the control of nanostructures in self-assembled materials with a goal to gain a better understanding of the governing principles in self-assembly.

This thesis presents experimental studies on the effect of modulated interactions between protein and polymers on the self-assembly of globular protein-polymer block copolymers. Bioconjugates composed of a model red fluorescent protein, mCherry, and a synthetic homopolymer with different chemical moieties are synthesized. Modulated interactions between protein and polymer by introducing polymer blocks with different hydrogen bonding capabilities change order-disorder transition concentrations in solution and the type of nanostructures formed. Bioconjugates with a weakly segregating polymer block are found to form a double gyroid structure with $Ia\bar{3}d$ symmetry, as opposed to perforated lamellae of bioconjugates with a strongly segregating polymer block. Common phase behaviors are also revealed, including the order of lyotropic order-order transitions and a re-entrant disordering behavior at high concentrations. Birefringence of the disordered solutions with increasing protein fraction suggests the formation of a nematic liquid crystalline phase arising from protein interactions. Self-assembly of protein-zwitterionic polymer bioconjugates shows that electrostatic segregation of mCherry constitutes one of the major driving forces for microphase separation. Nanostructures of the conjugates are further controlled by changing solvent selectivity.

Important considerations in preparing bioconjugate thin films are also presented and discussed. Surface effects as well as kinetics such as solvent evaporation rate and film coating speed are shown to have a large impact on the long-range order of self-assembled nanostructures.

Thesis supervisor: Bradely D. Olsen, Paul M. Cook Career Development Associate Professor of Chemical Engineering

Acknowledgements

First and foremost, I am very grateful for my thesis adviser, Professor Bradley Olsen. I was able to learn much from him, and I am grateful for the opportunity to work on many exciting projects while growing to be a better researcher under his mentorship. I also sincerely thank my thesis committee Professor Robert Cohen, Professor Hadley Sikes, and Professor Alfredo Alexander-Katz for their helpful advice and guidance.

I sincerely thank all Olsen group members who were also very critical for success of my graduate study. I very much enjoyed working in truly collaborative environment in Olsen group. I especially thank many earlier Olsen group members including Carla Thomas, Matthew Glassman, Mitchell Wang, Charlotte Stuart-Sloan, Christopher Lam, Shengchang Tang, Yin Fan, Michelle Sing, and Dr. Minkyu Kim for all their help with experiments, discussion, and being truly supportive colleagues. I also greatly enjoyed working with Dr. Guokui Qin, Dr. Allie Obermeyer, Aaron Huang, and Reginald Avery, as well as many newer group members. I appreciate help from all ISN staff members as well as Lionel Moh for their helpful advice on various materials characterizations. I also would like to thank Professor Paula Hammond, Zhiyong Poon, Amanda Engler, Dan Bonner, and Dr. Xiaoyong Zhao for all their support with my initial endeavor at MIT on a nanoparticle drug delivery project and for many fond memories.

I could not have achieved any of these without support of my family - I send my best wishes to my mother, little sister Seulji, and my father.

Table of Contents

List of Schemes

List of Tables

List of Figures

Chapter 1. Introduction and Background

Section 1.1 is adapted from a book chapter *Protein Nanopatterning* by Christopher N. Lam, Dongsook Chang, and Bradly D. Olsen in *Carbon Nanomaterials for Biomedical Applications*, M. Zhang et al. (eds.), Springer International Publishing Switzerland 2016.

1.1 Motivation

Enzymes have evolved to catalyze reactions that are beneficial to the survival of various organisms. Their ability to catalyze unique reactions that cannot be easily accessed using a synthetic route, high specificity towards a target molecule, regio- and stereospecificity which is crucial for production of pharmaceuticals and fine chemicals, and the mild reaction conditions—mild temperature, pressure, and environmental friendly solvent, water—are advantageous in addressing multiple industrial challenges. Enzymes can be used as molecular sensors—for example, glucose[1,2] and neurotoxin sensors[3–5]—and as a critical component in the enzyme-linked immunosorbent assay (ELISA). Enzymes have also proven to be beneficial for synthesizing drug compounds in the pharmaceutical industry,[6] and they have found utility in numerous industrial applications as biocatalysts for laundry and dishwasher detergents,[7] industrial synthetic chemistry,[8–10] and the food industry.[11] Biocatalytic devices for carbon sequestration,[12] carbon dioxide reduction,[13–15] and hydrogen production[16–18] have also been proposed utilizing enzymes. Biofuel cells have attracted significant attention, offering the possibility of consuming biomass as fuel and eliminating the need for both transition metal catalysts and electrolyte membranes due to the high specificity of the enzymatic reactions on both electrodes.[19,20] Beyond biocatalysis, reaction centers,[21] photosynthetic complexes,[22] and fluorescent proteins[23] can be incorporated into light harvesting materials for bioelectronics and energy applications. Protein materials have also found utility in developing surfaces for studies of cell growth and cell-surface interactions and for biomedical applications including tissue engineering.[24,25]

The function of biosensors, biocatalysts, bioelectronics, and biomedical materials can be improved through control over the position, orientation, and density of proteins presented within a bioactive material. Because proteins are fairly large compared to transition metal catalysts, it is often desirable to achieve a high density of proteins localized within a small area, improving catalytic rate in biocatalysts or signal to noise in sensors. The orientation of the protein and transport through thin film or bulk materials must be carefully controlled to enable efficient transport of substrates, products, cofactors, or charges through the device, thus requiring control of protein arrangement in nanometer scale. Furthermore, processing methods must not be deleterious to the native protein structure; ideally, the nanostructured material will provide an environment that enhances the stability and activity of the protein. Finally, practical applications require that the cost of patterning the material be commensurate with the value of the eventual application.

Two broad approaches, a top-down and bottom-up, are typically employed in order to prepare materials that meet as many of the above mentioned engineering criteria as possible. In the top-down approach, a surface is lithographically patterned and proteins are directed to selective regions of a surface. A variety of conventional and unconventional lithographic techniques including photolithography,[26–30] electron beam lithography,[31–34] dip-pen nanolithography,[35,36] nanografting,[37–39] and nanocontact printing[40–42] are used for protein nanopatterning, but with different resolution, speed and cost. Selective adsorption or reaction of proteins is primarily achieved by physical adsorption, covalent conjugation, or bioaffinity interactions.[43,44] In the bottom-up approach, templates may be constructed into which protein is inserted or onto which protein is reacted/absorbed, where the structure of the template directs the location of the protein. The templates are typically composed of lipid or amphiphilic block copolymers. While lithographic processes can form patterns of arbitrary shape (not necessarily periodic) with resolution that often approaches a single protein molecule, patterning is limited to two dimensions and the resultant protein density per unit area is relatively low. Methods using lipids or diblock copolymers to template proteins can achieve relatively high protein density with low self-assembly cost compared to top-down approaches, but the majority of the material is typically template polymer, reducing the total functional density of protein.

Our group has recently developed a new method of nanopatterning proteins by self-assembling protein-polymer diblock copolymers into a bulk nanostructured material.[45,46] This method meets the multiple requirements for a successful catalytic device. The self-assembled materials have a very high density of proteins; typically 30-60 wt.% of total mass is made of proteins depending on the size of proteins and polymers. Despite the high density, proteins remain accessible to substrates, products, cofactors, or charges due to continuous transport pathways generated by nanostructures. Protein orientation along the domain interfaces is controlled also by nanostructure formation. The stability and longevity of proteins are improved in the materials due to the presence of the protective polymer blocks, and the cost of patterning is relatively low compared to top-down approaches.

It is very interesting that a diblock copolymer consisting of a globular protein and a synthetic polymer undergoes microphase separation to form a variety of nanostructures, resembling the microphase separation of a diblock copolymer made of two synthetic homopolymers. While a great deal of knowledge is available about the self-assembly of conventional block copolymers composed of synthetic homopolymers which is reviewed in section 1.2, it is easy to see that the self-assembly principles learned from traditional synthetic block copolymers cannot be directly applied to the self-assembly of protein-polymer bioconjugates. Introducing a protein molecule with a globular shape, anisotropic interactions, and heterogeneous composition in replacement of a polymer chain with random coil conformation is expected to affect the optimal molecular packing geometry in equilibrium. Also, due to the limited availability of thermal annealing owing to a thermally unstable protein block, understanding kinetic processing pathways is critical in obtaining a good control of nanostructures of final solid state materials. As nanostructures in the self-assembled materials are governed by complex thermodynamics and kinetics due to the nature of proteins, a thorough investigation of the self-assembly behavior is required. This thesis is motivated by the intriguing question about how the nanostructures are controlled in the protein-polymer diblock copolymer materials.

1.2 Traditional Block Copolymer Self-Assembly

Diblock copolymers composed of two synthetic homopolymers undergo microphase separation, creating domains with nanometer length scales.[47,48] The ability of block copolymers form regular nanometer scale patterns[49] make them attractive candidates for the applications such as fuel cells,[50,51] batteries,[52,53] and solar cells.[54,55] Similar to the phase separation of two immiscible liquids such as oil and water resulting from unfavorable energy of mixing, two distinct homopolymer blocks in a block copolymer undergo phase separation due to their chemical dissimilarity. However, as the blocks are covalently connected, the size of phase separation is limited by entropic penalty imposed by chain stretching; thus resulting in microphase separation with a nanoscale domain size. As the entropy gain from mixing of polymers is much smaller than that of small molecules, even a small difference between two distinct monomers is sufficient to lead to microphase separation. The segregation strength is represented by a product of Flory Huggins interaction parameter, χ, and the degree of polymerization, N. As a result of interplay between enthalpy and entropy, block copolymers form several classical phases including a lamellar phase, hexagonally packed cylindrical phase, BCC cubic phase, and double gyroid phase with $Ia\bar{3}d$ symmetry. Size and structure of nanodomains can be tuned by changing types of monomers (χ), block copolymer composition (f_A), polymer size (N), and molecular architecture.

The phase behavior of block copolymers in solution is more complex compared to the melt phase behavior due to the distribution of the second component - a solvent - throughout the domains and interfaces. When a neat block copolymer is diluted in a solvent, it forms nanostructures due to the repulsion that drives microphase separation in melt, although the repulsion is now modulated by solvent molecules. The solution eventually becomes disordered above the critical concentration of a solvent, which is often referred to as an order-disorder transition concentration (C_{ODT}). Quality of solvent for each block determines interactions between blocks, and the selectivity of a solvent affects swelling of chains which in turn affects a relative volume fraction between two blocks. For a nonselective good solvent, the dilution approximation assumes that solvent molecules are uniformly distributed throughout the block copolymer structure, and an added neutral solvent screens unfavorable interactions between different blocks effectively lowering the χ parameters between two blocks such that $\chi_{eff} = \chi\phi N$ (where ϕ represents a volume fraction of block copolymers).[56,57] The dilution approximation can successfully predict order-order transitions (OOT) and domain spacings[58–61] provided a good solvent, small size of solvent molecules, and sufficiently small selectivity.[62]

However, substantial deviation from dilution approximation has been observed for prediction of order-disorder transitions (ODT).[59–61,63] Blocks are asymmetrically swollen in a selective solvent which is a good solvent for one block but it a poor solvent for the other block. Changing block copolymer concentration in a selective solvent can be qualitatively viewed as traversing a diagonal trajectory in a melt phase diagram.[60,61] Also, segregation strength can be increased or decreased depending on the degree of selectivity such that a weakly selective solvent lowers the segregation strength while a strongly selective solvent can increases the segregation strength.[60,61] For a nonselective poor solvent, the solution undergoes macrophase separation into a water-rich region and a block-copolymer-rich region.

Thin film geometry introduces two additional energy considerations; surface energetics and spatial confinement effect govern the phase behavior in addition to the factors governing the bulk self-assembly.[49,64,65] Interactions of block copolymers with two surfaces, either symmetric or asymmetric, determine segregation of blocks on each surface so that the block with lower interfacial energy will preferentially wet the surface. As a result, parallel orientation of nanodomains to the surface is often energetically favored over perpendicular orientation, which results in highly oriented grains as opposed to randomly oriented grains in bulk materials. In order to promote perpendicular ordering of nanodomains which is motivated by applications such as ultrafiltration membrane,[66–68] substrates are modified with random copolymer brushes to create a neutral surface.[69–71] It has been also shown that fast evaporation of solvent promotes perpendicularly ordered cylinders.[72–74] Incommensurability between block copolymer domain spacings and film thickness often results in rich morphological behavior including islands and holes structures,[75,76] or perpendicular orientation of nanodomains when surfaces are not strongly preferential.[69]

1.3 Self-Assembly of Globular Protein-Polymer Bioconjugates

The main differences between proteins and synthetic homopolymers originate from the heterogeneous composition of proteins made of 20 different amino acids building blocks. The diverse amino acids in a protein with different hydrophobicity, polarity, and acidity result in secondary and tertiary structures of protein in aqueous solutions through hydrophobic, hydrogen bonding, and electrostatic interactions. As a result, most functional proteins (as opposed to structural proteins such as collagen, elastin, or keratin) assume a globular shape. The dense and rigid nature of proteins is dramatically different than polymers with random coil conformation. Proteins cannot overlap with other proteins or swell in solution as polymers which change the conformation depending on the solvent quality and highly overlap with other chains in concentrated solution or melt. Anisotropic surface patches of globular proteins that lead to crystallization are also different from isotropic interactions of random coil polymers. In the self-assembly perspective, while the Flory-Huggins interaction parameter (χ) of two distinct blocks is defined based on the dissimilarity of two monomers, the interactions between protein and polymer are much more complex.

Our group has demonstrated the self-assembly of protein-polymer diblock copolymer into nanostructured materials using a model system of a conjugate of a red fluorescent protein, mCherry, and a synthetic biocompatible polymer block, poly(*N*-isopropylacrylamide) (PNIPAM).[45] mCherry is selected for its well-established expression and purification methods, high yield, robust structure, and relatively simple activity measurement using spectroscopy. In addition, application of fluorescent proteins as a biolasing component is recently reported.[77,78] PNIPAM is a widely used biocompatible polymer with the lower critical solution temperature (LCST) behavior which enables control of water-mediated polymer-polymer interactions. It has been shown that mCherry forms a bilayer structure in a lamellar nanostructure to minimize the interfacial area at a large polymer coil fraction ($\phi_{PNIPAM} = 0.70$). A more recent study shows multiple important differences between the phase behavior of protein-diblock copolymers and that of traditional coil-coil block copolymers; a lamellar region in the phase diagram is highly stretched to large coil fractions, no spherical cubic phase is observed, no cylindrical phase made of mCherry core is formed, and a re-entrant behavior at high concentration is observed.[79] Kinetics in processing the final solid materials are found to have a large impact on the final nanostructures due to kinetic aspects of solvent annealing process.[80] Kinetic effects on the processing of bioconjugate thin films are explored in detail in Chapter 4.

Equilibrium nanostructures in concentrated solution provided further insight into the thermodynamics governing the self-assembly of the bioconjugates.[81] mCherry-*b*-PNIPAM bioconjugates are found to undergo order-disorder transitions at concentrations between 30-40 wt.% in water. Multiple lyotropic and thermotropic phase transitions are observed as a function of concentration and temperature. The order-disorder transition concentrations (C_{ODT}) are lowest for the symmetric bioconjugates with a coil fraction (ϕ_{PNIPAM}) near 0.5, which suggests that the solvent-mediated net repulsive interactions are responsible for the microphase separation of protein-polymer diblock copolymers. This study directly motivated the current thesis to explore the effect of polymer block chemistry (Chapter 3) and the effect of electrostatic interactions on the self-assembly (Chapter 5).

1.4 Thesis Overview

This thesis describes studies on understanding the governing principles of the self-assembly of protein-polymer bioconjugates in concentrated solutions (Chapter 3, 5) and in thin films

(Chapter 4). Experimental methods about how polymerizations, bioconjugate preparation, and nanostructure characterization are conducted are described in detail in Chapter 2. Chapter 3 studies the effect of polymer block chemistry as a structure-directing element on the phase behavior of bioconjugates in concentrated solution. The results show that changing protein-polymer interactions by changing polymer block chemistry affects many aspects of phase behavior in solution. Higher order-disorder transition concentrations as well as formation of double gyroid nanostructure suggest the weaker segregation strengths of mCherry-*b*-PHPA and mCherry-*b*-POEGA bioconjugates compared to the previously studied mCherry-*b*-PNIPAM conjugates. The knowledge on the solution phase behavior of mCherry-*b*-POEGA is translated to the thin film self-assembly, which is presented in Chapter 4. Due to the limited annealing conditions available for protein-polymer conjugates as well as decreased activity of protein after annealing, understanding of nanostructures of as-cast films are critical. The study presents multiple important kinetic parameters in processing bioconjugate thin films including relative humidity which impacts solvent evaporation rate and flow coating speed. High relative humidity and high flow coating speed are found to result in films with longer range order. Chapter 5 describes the effect of electrostatic interaction and reduced charge asymmetry on the self-assembly of protein-polymer bioconjugates, in the context of understanding the nature of repulsive interactions of protein-polymer bioconjugates. Bioconjugates composed of mCherry and a zwitterionic polymer block are synthesized. The bioconjugates display weaker segregation strength compared to all previously studied mCherry-polymer conjugates, demonstrated by high C_{ODT}, extremely narrow ordered region in the phase diagram, and no nematic crystalline ordering in disordered phase at high concentration. Attractive interactions of polymer blocks are found to be critical in the self-assembly, and the ability to control nanostructures in solution by modulating protein-protein interactions by adding kosmotropic salt is demonstrated.

1.5 References

(1) Heller, A. Electrical Connection of Enzyme Redox Centers to Electrodes. *J. Phys. Chem.* **1992**, *96*, 3579–3587.

(2) Yehezkeli, O.; Yan, Y.-M.; Baravik, I.; Tel-Vered, R.; Willner, I. Integrated Oligoaniline-Cross-Linked Composites of Au Nanoparticles/Glucose Oxidase Electrodes: A Generic Paradigm for Electrically Contacted Enzyme Systems. *Chem. – A Eur. J.* **2009**, *15*, 2674–2679.

(3) Drevon, G. F.; Russell, A. J. Irreversible Immobilization of Diisopropylfluorophosphatase in Polyurethane Polymers. *Biomacromolecules* **2000**, *1*, 571–576.

(4) Russell, A. J.; Berberich, J. A.; Drevon, G. F.; Koepsel, R. R. Biomaterials for Mediation of Chemical and Biological Warfare Agents. *Annu. Rev. Biomed. Eng.* **2003**, *5*, 1–27.

(5) Simonian, A. L.; Grimsley, J. K.; Flounders, A. W.; Schoeniger, J. S.; Cheng, T.-C.; DeFrank, J. J.; Wild, J. R. Enzyme-Based Biosensor for the Direct Detection of Fluorine-Containing Organophosphates. *Anal. Chim. Acta* **2001**, *442*, 15–23.

(6) Patel, R. N. Synthesis of Chiral Pharmaceutical Intermediates by Biocatalysis. *Coord. Chem. Rev.* **2008**, *252*, 659–701.

(7) Hasan, F.; Shah, A. A.; Hameed, A. Industrial Applications of Microbial Lipases. *Enzyme Microb. Technol.* **2006**, *39*, 235–251.

(8) Schmid, A.; Dordick, J. S.; Hauer, B.; Kiener, A.; Wubbolts, M.; Witholt, B. Industrial Biocatalysis Today and Tomorrow. *Nature* **2001**, *409*, 258–268.

(9) Schoemaker, H. E.; Mink, D.; Wubbolts, M. G. Dispelling the Myths--Biocatalysis in Industrial Synthesis. *Science (80-.).* **2003**, *299*, 1694–1697.

(10) Straathof, A. J. J.; Panke, S.; Schmid, A. The Production of Fine Chemicals by Biotransformations. *Curr. Opin. Biotechnol.* **2002**, *13*, 548–556.

(11) Kirk, O.; Borchert, T. V.; Fuglsang, C. C. Industrial Enzyme Applications. *Curr. Opin. Biotechnol.* **2002**, *13*, 345–351.

(12) Favre, N.; Christ, M. L.; Pierre, A. C. Biocatalytic Capture of CO2 with Carbonic Anhydrase and Its Transformation to Solid Carbonate. *J. Mol. Catal. B Enzym.* **2009**, *60*, 163–170.

(13) Reda, T.; Plugge, C. M.; Abram, N. J.; Hirst, J. Reversible Interconversion of Carbon Dioxide and Formate by an Electroactive Enzyme. *Proc. Natl. Acad. Sci. U. S. A.* **2008**, *105*, 10654–10658.

(14) Parkinson, B. A.; Weaver, P. F. Photoelectrochemical Pumping of Enzymatic Co2 Reduction. *Nature* **1984**, *309*, 148–149.

(15) Kuwabata, S.; Tsuda, R.; Yoneyama, H. Electrochemical Conversion of Carbon Dioxide to Methanol with the Assistance of Formate Dehydrogenase and Methanol Dehydrogenase as Biocatalysts. *J. Am. Chem. Soc.* **1994**, *116*, 5437–5443.

(16) Karyakin, A. A.; Morozov, S. V; Karyakina, E. E.; Varfolomeyev, S. D.; Zorin, N. A.; Cosnier, S. Hydrogen Fuel Electrode Based on Bioelectrocatalysis by the Enzyme Hydrogenase. *Electrochem. commun.* **2002**, *4*, 417–420.

(17) Hambourger, M.; Gervaldo, M.; Svedruzic, D.; King, P. W.; Gust, D.; Ghirardi, M.; Moore, A. L.; Moore, T. A. [FeFe]-Hydrogenase-Catalyzed H2 Production in a Photoelectrochemical Biofuel Cell. *J. Am. Chem. Soc.* **2008**, *130*, 2015–2022.

(18) Krassen, H.; Schwarze, A.; Friedrich, B.; Ataka, K.; Lenz, O.; Heberle, J. Photosynthetic Hydrogen Production by a Hybrid Complex of Photosystem I and [NiFe]-Hydrogenase. *ACS Nano* **2009**, *3*, 4055–4061.

(19) Minteer, S. D.; Liaw, B. Y.; Cooney, M. J. Enzyme-Based Biofuel Cells. *Curr. Opin. Biotechnol.* **2007**, *18*, 228–234.

(20) Leech, D.; Kavanagh, P.; Schuhmann, W. Enzymatic Fuel Cells: Recent Progress. *Electrochim. Acta* **2012**, *84*, 223–234.

(21) Cogdell, R. J.; Gall, A.; Kohler, J. The Architecture and Function of the Light-Harvesting Apparatus of Purple Bacteria: From Single Molecules to in Vivo Membranes. *Q. Rev. Biophys.* **2006**, *39*, 227–324.

(22) Das, R.; Kiley, P. J.; Segal, M.; Norville, J.; Yu, A. A.; Wang, L.; Trammell, S. A.; Reddick, L. E.; Kumar, R.; Stellacci, F.; *et al.* Integration of Photosynthetic Protein Molecular Complexes in Solid-State Electronic Devices. *Nano Lett.* **2004**, *4*, 1079–1083.

(23) Choi, J.-W. W.; Fujihira, M. Molecular-Scale Biophotodiode Consisting of a Green Fluorescent Protein/cytochrome c Self-Assembled Heterolayer. *Appl. Phys. Lett.* **2004**, *84*, 2187–2189.

(24) Falconnet, D.; Csucs, G.; Michelle Grandin, H.; Textor, M. Surface Engineering Approaches to Micropattern Surfaces for Cell-Based Assays. *Biomaterials* **2006**, *27*, 3044–3063.

(25) Vörös, J.; Blättler, T.; Textor, M. Bioactive Patterns at the 100-Nm Scale Produced Using Multifunctional Physisorbed Monolayers. *Mrs Bull.* **2005**, *30*, 202–206.

(26) Mooney, J. F.; Hunt, A. J.; McIntosh, J. R.; Liberko, C. A.; Walba, D. M.; Rogers, C. T. Patterning of Functional Antibodies and Other Proteins by Photolithography of Silane Monolayers. *Proc. Natl. Acad. Sci.* **1996**, *93*, 12287–12291.

(27) Flounders, A. W.; Brandon, D. L.; Bates, A. H. Patterning of Immobilized Antibody Layers via Photolithography and Oxygen Plasma Exposure. *Biosens. Bioelectron.* **1997**, *12*, 447–456.

(28) Sorribas, H.; Padeste, C.; Tiefenauer, L. Photolithographic Generation of Protein Micropatterns for Neuron Culture Applications. *Biomaterials* **2002**, *23*, 893–900.

(29) Shin, D.-S.; Lee, K.-N.; Jang, K.-H.; Kim, J.-K.; Chung, W.-J.; Kim, Y.-K.; Lee, Y.-S. Protein Patterning by Maskless Photolithography on Hydrophilic Polymer-Grafted Surface. *Biosens. Bioelectron.* **2003**, *19*, 485–494.

(30) Petrou, P. S.; Chatzichristidi, M.; Douvas, A. M.; Argitis, P.; Misiakos, K.; Kakabakos, S. E. A Biomolecule Friendly Photolithographic Process for Fabrication of Protein Microarrays on Polymeric Films Coated on Silicon Chips. *Biosens. Bioelectron.* **2007**, *22*, 1994–2002.

(31) Harnett, C. K.; Satyalakshmi, K. M.; Craighead, H. G. Bioactive Templates Fabricated by Low-Energy Electron Beam Lithography of Self-Assembled Monolayers. *Langmuir* **2000**, *17*, 178–182.

(32) Lussi, J. W.; Tang, C.; Kuenzi, P. A.; Staufer, U.; Csucs, G.; Voros, J.; Danuser, G.; Hubbell, J. A.; Textor, M. Selective Molecular Assembly Patterning at the Nanoscale: A Novel Platform for Producing Protein Patterns by Electron-Beam Lithography on SiO2/indium Tin Oxide-Coated Glass Substrates. *Nanotechnology* **2005**, *16*, 1781–1786.

(33) Pallandre, A.; De Meersman, B.; Blondeau, F.; Nysten, B.; Jonas, A. M. Tuning the Orientation of an Antigen by Adsorption onto Nanostriped Templates. *J. Am. Chem. Soc.* **2005**, *127*, 4320–4325.

(34) Kolodziej, C. M.; Maynard, H. D. Electron-Beam Lithography for Patterning Biomolecules at the Micron and Nanometer Scale. *Chem. Mater.* **2012**, *24*, 774–780.

(35) Lee, K. B.; Park, S. J.; Mirkin, C. A.; Smith, J. C.; Mrksich, M. Protein Nanoarrays Generated by Dip-Pen Nanolithography. *Science (80-.).* **2002**, *295*, 1702–1705.

(36) Ginger, D. S.; Zhang, H.; Mirkin, C. A. The Evolution of Dip-Pen Nanolithography. *Angew. Chemie-International Ed.* **2004**, *43*, 30–45.

(37) Case, M. A.; McLendon, G. L.; Hu, Y.; Vanderlick, T. K.; Scoles, G. Using Nanografting to Achieve Directed Assembly of de Novo Designed Metalloproteins on Gold. *Nano Lett.* **2002**, *3*, 425–429.

(38) Hu, Y.; Das, A.; Hecht, M. H.; Scoles, G. Nanografting de Novo Proteins onto Gold Surfaces. *Langmuir* **2005**, *21*, 9103–9109.

(39) Bano, F.; Fruk, L.; Sanavio, B.; Glettenberg, M.; Casalis, L.; Niemeyer, C. M.; Scoles, G. Toward Multiprotein Nanoarrays Using Nanografting and DNA Directed Immobilization of Proteins. *Nano Lett.* **2009**, *9*, 2614–2618.

(40) Csucs, G.; Künzler, T.; Feldman, K.; Robin, F.; Spencer, N. D. Microcontact Printing of Macromolecules with Submicrometer Resolution by Means of Polyolefin Stamps. *Langmuir* **2003**, *19*, 6104–6109.

(41) Li, H. W.; Muir, B. V. O.; Fichet, G.; Huck, W. T. S. Nanocontact Printing: A Route to Sub-50-Nm-Scale Chemical and Biological Patterning. *Langmuir* **2003**, *19*, 1963–1965.

(42) Ruiz, S. A.; Chen, C. S. Microcontact Printing: A Tool to Pattern. *Soft Matter* **2007**, *3*, 168–177.

(43) Rusmini, F.; Zhong, Z. Y.; Feijen, J. Protein Immobilization Strategies for Protein Biochips. *Biomacromolecules* **2007**, *8*, 1775–1789.

(44) Sassolas, A.; Blum, L. J.; Leca-Bouvier, B. D. Immobilization Strategies to Develop Enzymatic Biosensors. *Biotechnol. Adv.* **2012**, *30*, 489–511.

(45) Thomas, C. S.; Glassman, M. J.; Olsen, B. D. Solid-State Nanostructured Materials from Self-Assembly of a Globular Protein-Polymer Diblock Copolymer. In *ACS Nano*; American Chemical Society, 2011; Vol. 5, pp. 5697–5707.

(46) Olsen, B. D. Self-Assembly of Globular-Protein-Containing Block Copolymers. *Macromol. Chem. Phys.* **2013**, *214*, 1659–1668.

(47) Bates, F. S. Polymer-Polymer Phase Behavior. *Science* **1991**, *251*, 898–905.

(48) Bates, F. S.; Fredrickson, G. H. Block Copolymers—Designer Soft Materials. *Phys. Today* **1999**, *52*, 32–38.

(49) Segalman, R. A. Patterning with Block Copolymer Thin Films. *Mater. Sci. Eng. R-Reports* **2005**, *48*, 191–226.

(50) Meier-Haack, J.; Taeger, A.; Vogel, C.; Schlenstedt, K.; Lenk, W.; Lehmann, D. Membranes from Sulfonated Block Copolymers for Use in Fuel Cells. *Sep. Purif. Technol.* **2005**, *41*, 207–220.

(51) Elabd, Y. A.; Hickner, M. A. Block Copolymers for Fuel Cells. *Macromolecules* **2011**, *44*, 1–11.
(52) Young, W. S.; Kuan, W. F.; Epps, T. H. Block Copolymer Electrolytes for Rechargeable Lithium Batteries. *J. Polym. Sci. Part B Polym. Phys.* **2014**, *52*, 1–16.
(53) Orilall, M. C.; Wiesner, U. Block Copolymer Based Composition and Morphology Control in Nanostructured Hybrid Materials for Energy Conversion and Storage: Solar Cells, Batteries, and Fuel Cells. *Chem. Soc. Rev.* **2011**, *40*, 520–535.
(54) Sun, S.-S. Design of a Block Copolymer Solar Cell. *Sol. Energy Mater. Sol. Cells* **2003**, *79*, 257–264.
(55) Crossland, E. J. W.; Nedelcu, M.; Ducati, C.; Ludwigs, S.; Hillmyer, M. A.; Steiner, U.; Snaith, H. J. Block Copolymer Morphologies in Dye-Sensitized Solar Cells: Probing the Photovoltaic Structure-Function Relation. *Nano Lett.* **2009**, *9*, 2813–2819.
(56) Helfand, E.; Tagami, Y. Theory of the Interface between Immiscible Polymers. II. *J. Chem. Phys.* **1972**, *56*, 3592–3601.
(57) Whitmore, M. D.; Noolandi, J. Self-Consistent Theory of Block Copolymer Blends: Neutral Solvent. *J. Chem. Phys.* **1990**, *93*, 2946.
(58) Hashimoto, T.; Shibayama, M.; Hiromichi, K.; Kawai, H. Ordered Structure in Block Polymer Solutions. 4. Scaling Rules on Size of Fluctuations with Block Molecular Weight, Concentration, and Temperature in Segregation and Homogeneous Regimes. *Macromolecules* **1983**, *16*, 1093–1101.
(59) Sakurai, S.; Hashimoto, T.; Fetters, L. J. Thermoreversible Cylinder-Sphere Transition of Polystyrene-Block-Polyisoprene Diblock Copolymers in Dioctyl Phthalate Solutions. *Macromolecules* **1996**, *29*, 740–747.
(60) Hanley, K. J.; Lodge, T. P. Effect of Dilution on a Block Copolymer in the Complex Phase Window. *J. Polym. Sci. Part B Polym. Phys.* **1998**, *36*, 3101–3113.
(61) Hanley, K. J.; Lodge, T. P.; Huang, C. I. Phase Behavior of a Block Copolymer in Solvents of Varying Selectivity. *Macromolecules* **2000**, *33*, 5918–5931.
(62) Naughton, J. R.; Matsen, M. W. Limitations of the Dilution Approximation for Concentrated Block Copolymer/solvent Mixtures. *Macromolecules* **2002**, *35*, 5688–5696.
(63) Lodge, T. P.; Pan, C.; Jin, X.; Liu, Z.; Zhao, J.; Maurer, W. W.; Bates, F. S. Failure of the Dilution Approximation in Block Copolymer Solutions. *J. Polym. Sci. Part B Polym. Phys.* **1995**, *33*, 2289–2293.
(64) Fasolka, M. J.; Mayes, A. M. Block Copolymer Thin Films: Physics and Applications. *Annu. Rev. Mater. Res.* **2001**, *31*, 323–355.
(65) Albert, J. N. L.; Epps, T. H. Self-Assembly of Block Copolymer Thin Films. *Mater. Today* **2010**, *13*, 24–33.
(66) Phillip, W. A.; Rzayev, J.; Hillmyer, M. A.; Cussler, E. L. Gas and Water Liquid Transport through Nanoporous Block Copolymer Membranes. *J. Memb. Sci.* **2006**, *286*, 144–152.
(67) Phillip, W. A.; O'Neill, B.; Rodwogin, M.; Hillmyer, M. A.; Cussler, E. L. Self-Assembled Block Copolymer Thin Films as Water Filtration Membranes. *ACS Appl. Mater. Interfaces* **2010**, *2*, 847–853.
(68) Jackson, E. A.; Hillmyer, M. A. Nanoporous Membranes Derived from Block Copolymers: From Drug Delivery to Water Filtration. *ACS Nano* **2010**, *4*, 3548–3553.

(69) Kellogg, G.; Walton, D.; Mayes, A.; Lambooy, P.; Russell, T.; Gallagher, P.; Satija, S. Observed Surface Energy Effects in Confined Diblock Copolymers. *Phys. Rev. Lett.* **1996**, *76*, 2503–2506.

(70) Huang, E.; Rockford, L.; Russell, T. P.; Hawker, C. J. Nanodomain Control in Copolymer Thin Films. *Nature* **1998**, *395*, 757–758.

(71) Huang, E.; Russell, T. P.; Harrison, C.; Chaikin, P. M.; Register, R. A.; Hawker, C. J.; Mays, J. Using Surface Active Random Copolymers To Control the Domain Orientation in Diblock Copolymer Thin Films. *Macromolecules* **1998**, *31*, 7641–7650.

(72) Turturro, A.; Gattiglia, E.; Vacca, P.; Viola, G. T. Free Surface Morphology of Block Copolymers: 1. Styrene-Butadiene Diblock Copolymers. *Polymer (Guildf).* **1995**, *36*, 3987–3996.

(73) Kim, G.; Libera, M. Morphological Development in Solvent-Cast Polystyrene - Polybutadiene - Polystyrene (SBS) Triblock Copolymer Thin Films. *Macromolecules* **1998**, *31*, 2569–2577.

(74) Phillip, W. A.; Hillmyer, M. A.; Cussler, E. L. Cylinder Orientation Mechanism in Block Copolymer Thin Films upon Solvent Evaporation. *Macromolecules* **2010**, *43*, 7763–7770.

(75) Coulon, G.; Collin, B.; Ausserre, D.; Chatenay, D.; Russell, T. P. Islands and Holes on the Free Surface of Thin Diblock Copolymer Films. I. Characteristics of Formation and Growth. *J. Phys.* **1990**, *51*, 2801–2811.

(76) Smith, A. P.; Douglas, J. F.; Meredith, J. C.; Amis, E. J.; Karim, A. Combinatorial Study of Surface Pattern Formation in Thin Block Copolymer Films. *Phys. Rev. Lett.* **2001**, *87*, 015503.

(77) Jonas, A.; Kiraz, A. In Vitro and in Vivo Biolasing of Fluorescent Proteins Suspended in Liquid Microdroplet Cavities. *Lab Chip* **2014**, 3093–3100.

(78) Gather, M. C.; Yun, S. H. Bio-Optimized Energy Transfer in Densely Packed Fluorescent Protein Enables near-Maximal Luminescence and Solid-State Lasers. *Nat. Commun.* **2014**, *5*, 5722.

(79) Thomas, C. S.; Olsen, B. D. Coil Fraction-Dependent Phase Behaviour of a Model Globular Protein–polymer Diblock Copolymer. *Soft Matter* **2014**, *10*, 3093–3102.

(80) Thomas, C. S.; Xu, L.; Olsen, B. D. Kinetically Controlled Nanostructure Formation in Self-Assembled Globular Protein–Polymer Diblock Copolymers. *Biomacromolecules* **2012**, *13*, 2781–2792.

(81) Lam, C. N.; Olsen, B. D. Phase Transitions in Concentrated Solution Self-Assembly of Globular Protein–polymer Block Copolymers. *Soft Matter* **2013**, *9*, 2393.

Chapter 2. Experimental Methods

2.1 Polymer Synthesis

Materials.

All solvents and chemicals used in this thesis are listed in Table 2-1 and 2-2, respectively.

Table 2-1. Grade, purity, and source of solvents used in this thesis.

Solvent	CAS Number	Grade and Purity	Supplier
Acetone	67-64-1	ACS grade (≥ 99.5%)	Macron Fine Chemicals™
Diethyl ether	60-29-7	ACS grade (≥ 99.0%)	J.T.Baker
Dichloromethane	75-09-2	ACS grade (≥ 99.5%)	Macron Fine Chemicals™
Hexane	110-54-3	ACS grade (≥ 98.5%)	Macron Fine Chemicals™
Ethyl acetate	141-78-6	ACS grade (≥ 99.5%)	Macron Fine Chemicals™
Dioxane	123-91-1	ACS grade (≥ 99.0%)	Sigma-Aldrich
Trifluoroethanol	75-89-8	*ReagentPlus*® (≥ 99%)	Sigma-Aldrich
Chloroform	67-66-3	ACS grade (≥ 99.8%)	Macron Fine Chemicals™
Chloroform-d	865-49-6	D, 99.8%	Cambridge Isotope Laboratories Inc.
Deuterium oxide	7789-20-0	D, 99.8%, sterility tested	Cambridge Isotope Laboratories Inc.

Table 2-2. Purity and source of chemicals used in this thesis.

Chemical	CAS Number	Purity	Supplier
Ethanethiol	75-08-1	97%	Aldrich
Aliquat® 336	63393-96-4	N/A	Aldrich
Carbon disulfide (CS_2)	75-15-0	≥ 99.9%	Sigma-Aldrich
4-dimethylaminopyridine (DMAP)	1122-58-3	99%	Aldrich
4-cyano-4-(phenylcarbonothioylthio)pentanoic acid (CPP)	201611-92-9	≥ 97%	Strem Chemicals

exo-3a,4,7,7a-tetrahydro-2-(3-hydroxypropyl)-4,7-epoxy-14-isoindole-1,3(2*H*)-dione	6118-51-0	N/A	Aldrich
N,*N*'-dicyclohexylcarbodiimide (DCC)	538-75-0	99%	Aldrich
2-hydroxypropyl acrylate (mixture of isomers)	25584-83-2	95% 200 ppm hydroquinone monomethyl ether as inhibitor	Sigma-Aldrich
Aluminum oxide (activated, basic, Brockmann I)	1344-28-1	N/A (Pore size 58Å, pH 9.5 ± 0.5 in H_2O)	Sigma-Aldrich
Azobisisobutyronitrile (AIBN)	78-67-1	98%	Aldrich
Trimethylamine	121-44-8	$\geq$ 99%	Sigma-Aldrich
2-(2-methoxyethoxy)ethanol	111-77-3	ReagentPlus®, $\geq$99.0%	Sigma-Aldrich
Acryloyl chloride	814-68-6	$\geq$ 97% (~400 ppm phenothiazine as stabilizer)	Sigma-Aldrich
Anhydrous Na_2SO_4	7757-82-6	ACS grade	Macron Fine Chemicals™
2-methoxyethyl acrylate	3121-61-7	98% (50-100 ppm MEHQ as inhibitor)	Aldrich
2,2'-Azobis[2-(2-imidazolin-2-yl)propane]dihydrochloride (VA-044)	27776-21-2	N/A	Wako chemicals
3-[*N*-(2-methacroyloyethyl)-*N*,*N*-dimethylammonio]propane sulfonate (DMAPS)	3637-26-1	97%	Aldrich
Hydroquinone (HQ)	123-31-9	99%	Alfa Aesar
Butylated hydroxytoluene (BHT)	128-37-0	$\geq$ 99.0%	Aldrich

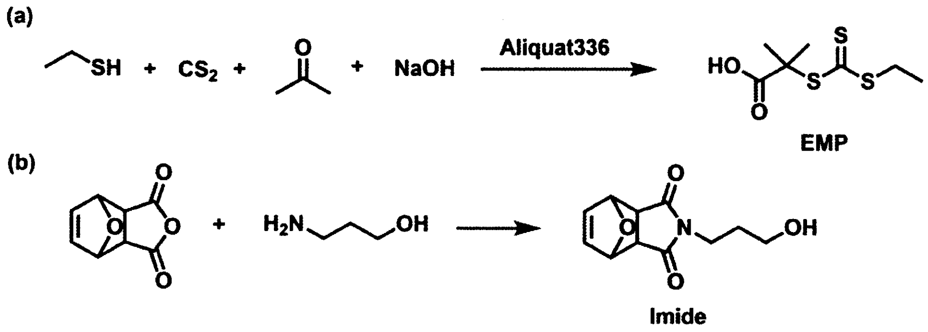

Scheme 2-1. Synthesis of precursors of chain transfer agents. (a) EMP synthesis and (b) Imide synthesis.

Synthesis of 2-ethylsulfanylthiocarbonyl sulfanyl-2-methylpropionic acid (EMP). Synthesis of EMP was conducted according to a previous work (Scheme 2-1a)[1] which was adapted from a 2-dodecylsulfanylthiocarbonylsulfanyl-2-methyl propionic acid (DMP) synthesis, a similar compound with a longer alkyl chain.[2] Typically, 7.21 mL (6.21 g) ethanethiol, 73.3 mL acetone, 1.13 mL Aliquat® 336 were combined and cooled in ice bath and under nitrogen stream. 9 mL of 50% NaOH aqueous solution was added to the reaction mixture over 10 minutes. 6.03 mL CS_2 and 12.64 mL acetone were combined in a dropping funnel and added to the reaction mixture over 30 minutes. 80 mL of the 50% NaOH solution was added over 20 minutes and the reaction mixture was stirred overnight. Next day, 200 mL of distilled water and 80 mL of concentrated HCl were added to the solution. Crude product was extracted three times in 100 mL of diethyl ether and solvent was removed by rotary evaporation. The crude product was purified over silica gel column (typically 400 mL of silica was used). First yellow fraction was washed using 1 L hexane which was discarded afterwards. As much as the second streaky fraction with orange/brown color was collected using a 1:1 mixture of hexane and diethyl ether as a mobile phase. The third fraction was discarded. Solvent was removed by rotary evaporation and the product was purified further by distillation. Impurity was collected as the first fraction up to 135 °C 190 mTorr with bright yellow color. The pure EMP was collected as the second fraction up to 157 °C 120 mTorr. The final orange-colored product was analyzed using thin-layer chromatography (TLC) and ^{1}H-NMR (Figure 2-1).

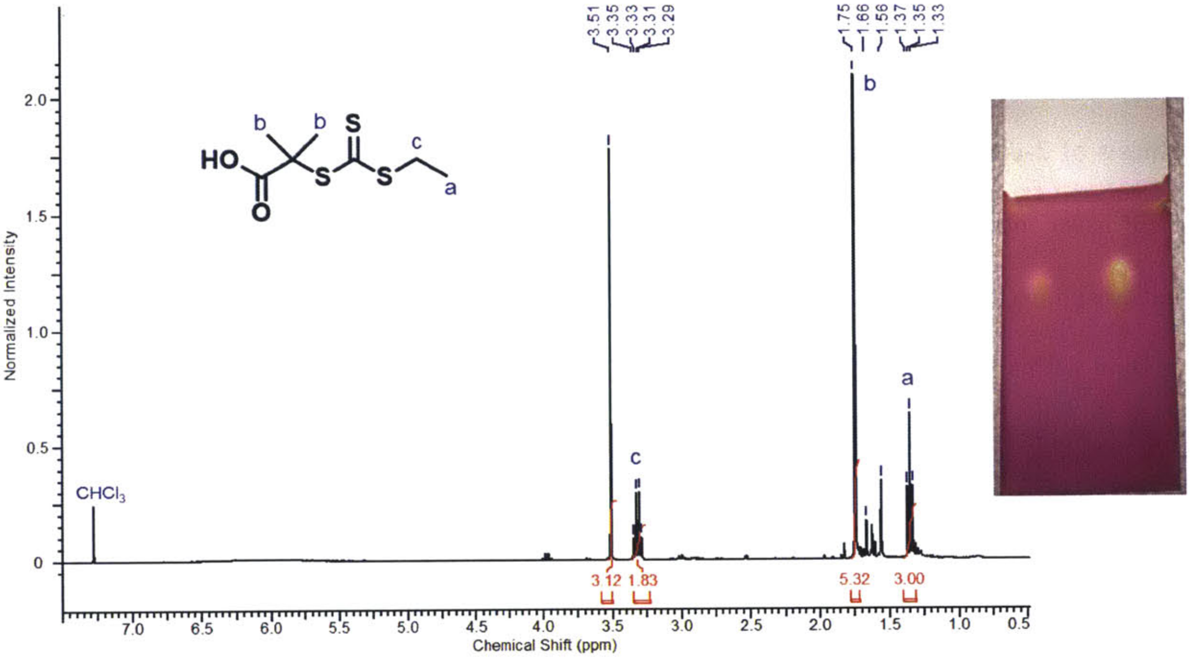

Figure 2-1. ^{1}H-NMR spectrum of EMP in deuterated chloroform ($CDCl_3$), and TLC result of purified EMP showing purity after distillation. The TLC was run in a 1:1 mixture of hexane and diethyl ether. The second lane of the TLC plate represents the same sample as the first lane but twice more concentrated.

Synthesis of exo-3a,4,7,7a-tetrahydro-2-(3-hydroxypropyl)-4,7-epoxy-14-isoindole-1,3(2*H*)-dione (Imide). Synthesis of Imide was performed following a previously published method[1] (Scheme 2-1b) which was adapted from a literature.[3] 500 mL methanol was added to a 1 L round-bottom flask containing 9 g of exo-3,6-epoxy-1,2,3,6-tetrahydrophthalic anhydride. 4.08 g of 3-amino-1-propanol was added dropwise to the solution while stirring over approximately 30 minutes, after which the solution became clear. The reaction mixture was submerged in an oil bath heated at 56°C and stirred for 3-4 days. The flask was removed from the oil bath, and the solvent was removed by rotary evaporation to obtain clear yellow oil. 200 mL of dichloromethane was added to the oil, and washed three times with 200 mL saturated sodium chloride solution. The collected organic layer was dried over anhydrous sodium sulfate which was removed by filtration. Dichloromethane was removed by rotary evaporation, resulting in a white solid (yield 20%).

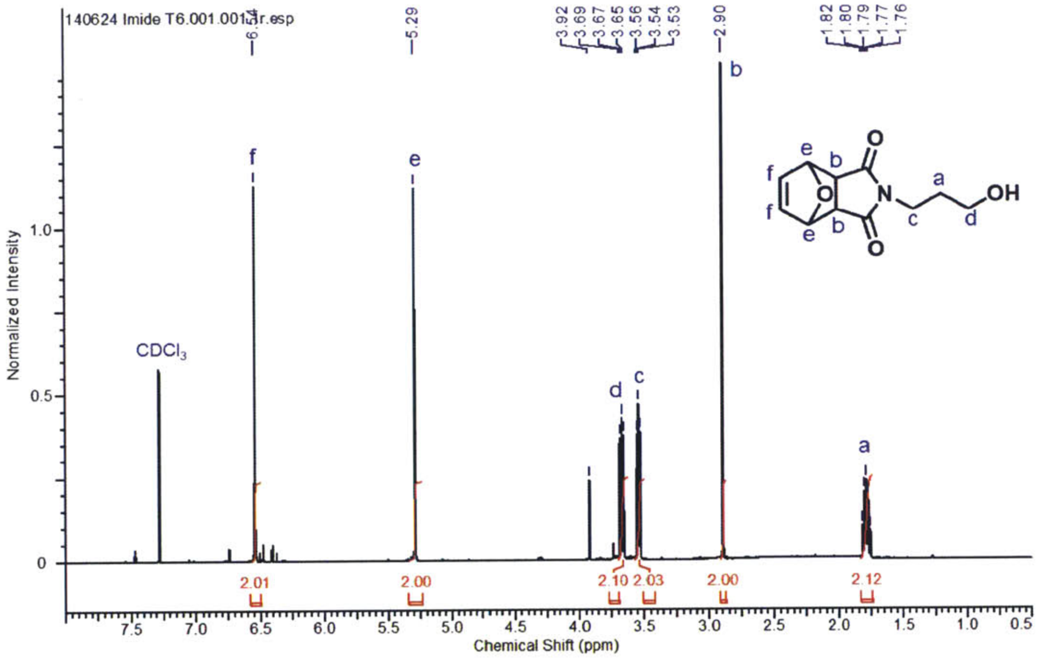

Figure 2-2. ^{1}H-NMR spectrum of exo-3a,4,7,7a-tetrahydro-2-(3-hydroxypropyl)-4,7-epoxy-14-isoindole-1,3(2*H*)-dione (Imide) in CDCl$_3$.

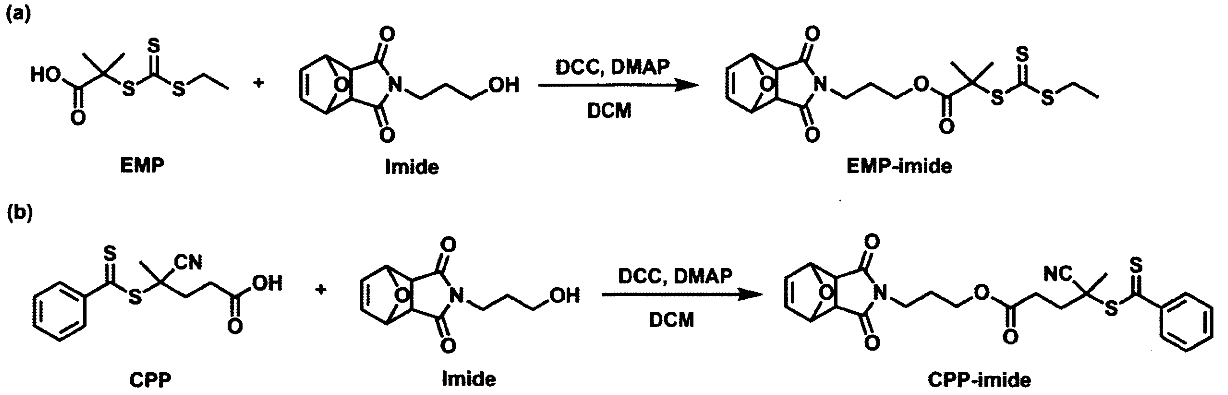

Scheme 2-2. Synthesis of two chain transfer agents used for reversible addition-fragmentation chain-transfer (RAFT) polymerization in this thesis. (a) EMP-imide synthesis from EMP and Imide, and (b) CPP-imide RAFT agent from CPP and Imide, both through a DCC coupling reaction.

Synthesis of EMP-imide. Synthesis of EMP-imide shown in Scheme 2-2a was conducted following the previously published protocol.[1] 2.10 g of EMP (9.35 mmol, 1 equiv.) and 2.28 g of Imide (10.21 mmol, 1.1 equiv.) were dissolved in 85 mL of dichloromethane. 113 mg of DMAP (1.01 mmol, 0.1 equilv.) was added to the reaction mixture, and 2.30 g of DCC (11.15 mmol, 1.2 equiv.) was added. The mixture was stirred overnight at room temperature. The solution was filtered to remove urea, and the solvent was removed by rotary evaporation. The crude mixture was purified using silica gel column chromatography using a 1:1 mixture of hexane and ethyl acetate as the mobile phase. Fractions containing the product with $R_f \sim 0.4$ were collected based on TLC analysis (Figure 2-3). A majority of the solvent was removed by rotary evaporation, and the solid was further dried in a vacuum oven at room temperature overnight. Purity of product was analyzed using ^{1}H-NMR (Figure 2-4). 2.55 g of yellow solid was obtained after drying (yield: 64 %) and stored at -20 °C in the dark until it was used.

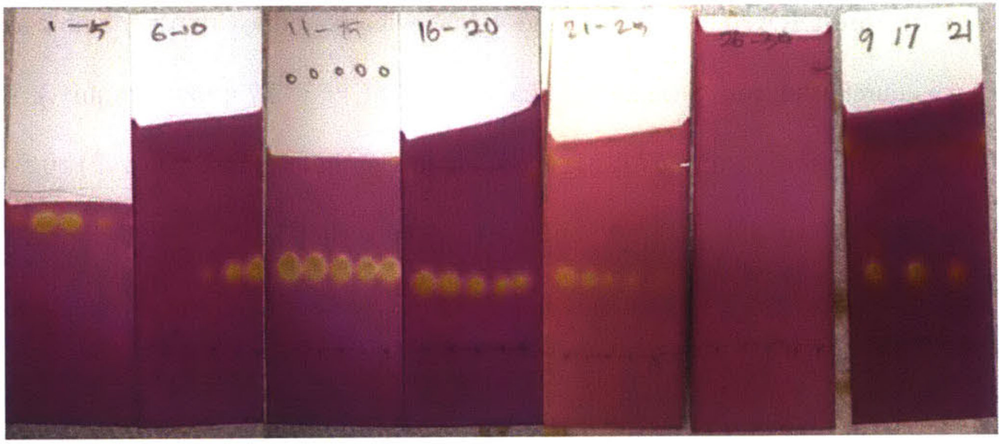

Figure 2-3. TLC analysis of fractions collected during column chromatography for EMP-imide purification. The mobile phase used for TLC was a 1:1 mixture of hexane and ethyl acetate. The number of fractions are indicated on the top of each TLC plate. From this particular purification, fractions from 9 to 25 were collected.

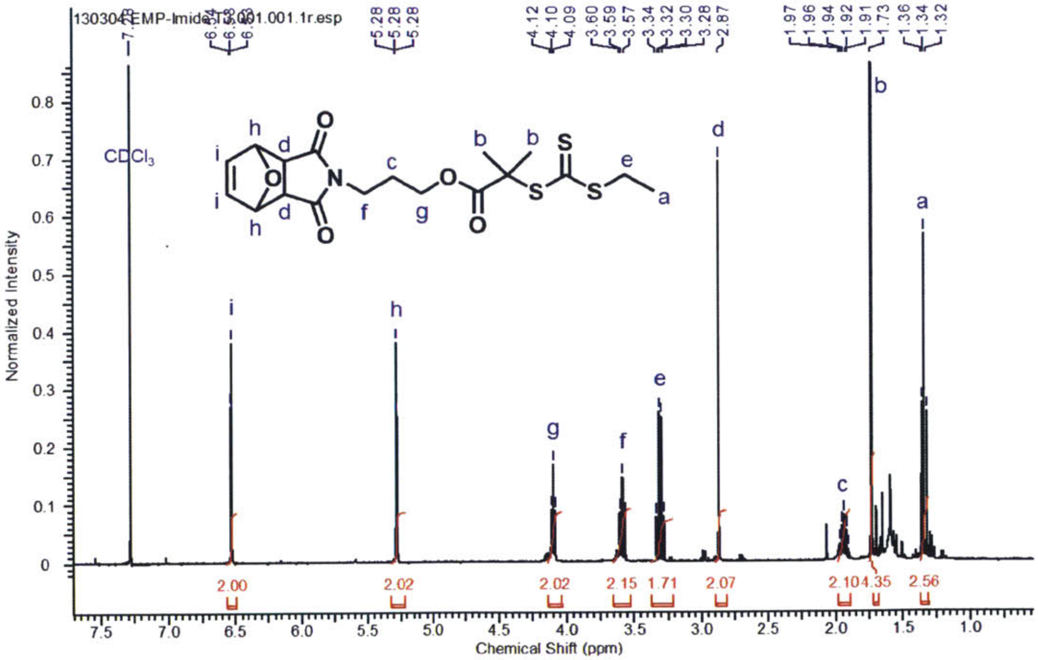

Figure 2-4. ^{1}H-NMR spectrum of EMP-imide in $CDCl_3$.

Synthesis of CPP-imide RAFT agent. 4-cyano-4-(phenylcarbonothioylthio)pentanoic acid (min. 97%) (CPP) was purchased from Strem Chemicals. 1.5 g of CPP (5.37 mmol, 1 equiv.), 1.36 g of Imide (5.91 mmol, 1.1 equiv.) and 67.4 mg of 4-dimethylaminopyridine (DMAP) (0.54 mmol, 0.1 equiv.) were dissolved in 50 mL of dichloromethane. 1.37 g of *N,N'*-dicyclohexylcarbodiimide (DCC) (6.44 mmol, 1.2 equiv.) was added to the mixture and stirred under nitrogen overnight. The reaction mixture was washed using house distilled water three times and dried under anhydrous sodium sulfate. The solvent was removed by rotary evaporation. The crude product was further purified using a flash chromatography in an Isolera One Biotage system. A KP-Sil 50 g cartridge was used with hexane and ethyl acetate as eluents. After a quick wash step at 30% ethyl acetate for 1 column volume (CV), percent ethyl acetate was linearly increased to 80% over 15 CV, followed by a final wash step at 100% for 4 CV as shown in Figure 2-7a. The fractions containing the correct molar mass compound analyzed by liquid chromatography–mass spectrometry (LC-MS) were collected. LC-MS was performed using a poroshell 120 EC-C18; 3.0 x 50 mm; 2.7 micron column. Water with 0.1% formic acid was used for solvent A and acetonitrile with 0.1% formic acid for solvent B. A default linear gradient program applied to analyze CPP-imide samples is shown in the table below.

Time (min)	**A (%)**	**B (%)**	**Flow (mL/min)**
0.00	95.0	5.0	0.550
5.20	5.0	95.0	
6.00	5.0	95.0	
6.40	95.0	5.0	
8.00	95.0	5.0	

Solvent was removed by rotary evaporation, and the red oil was further dried in a vacuum oven at room temperature overnight. Due to the high viscosity of the product, drying process of this compound was carefully monitored and vacuum level was adjusted as necessary to prevent excessive bubbling. Purity of product was analyzed using ^{1}H-NMR (Figure 2-5) and LC-MS (Figure 2-6). 1.9 g of red oil was obtained after drying (yield: 73 %) and stored at -20 °C in the dark until it was used.

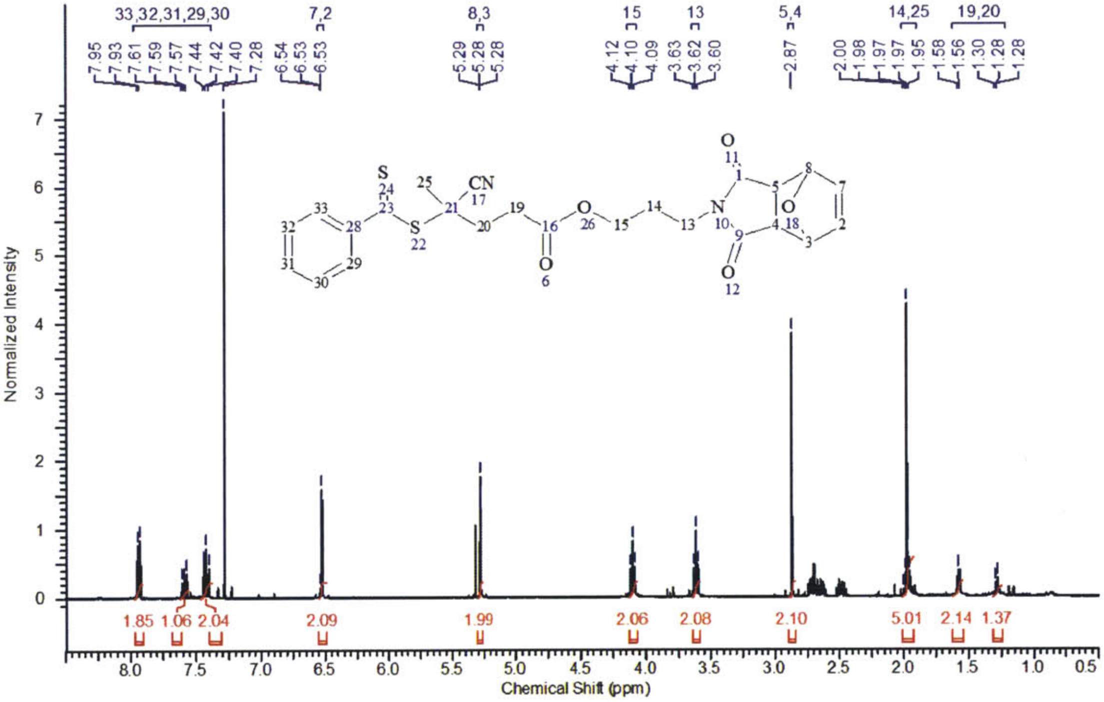

Figure 2-5. ^{1}H-NMR spectrum of CPP-imide in $CDCl_3$.

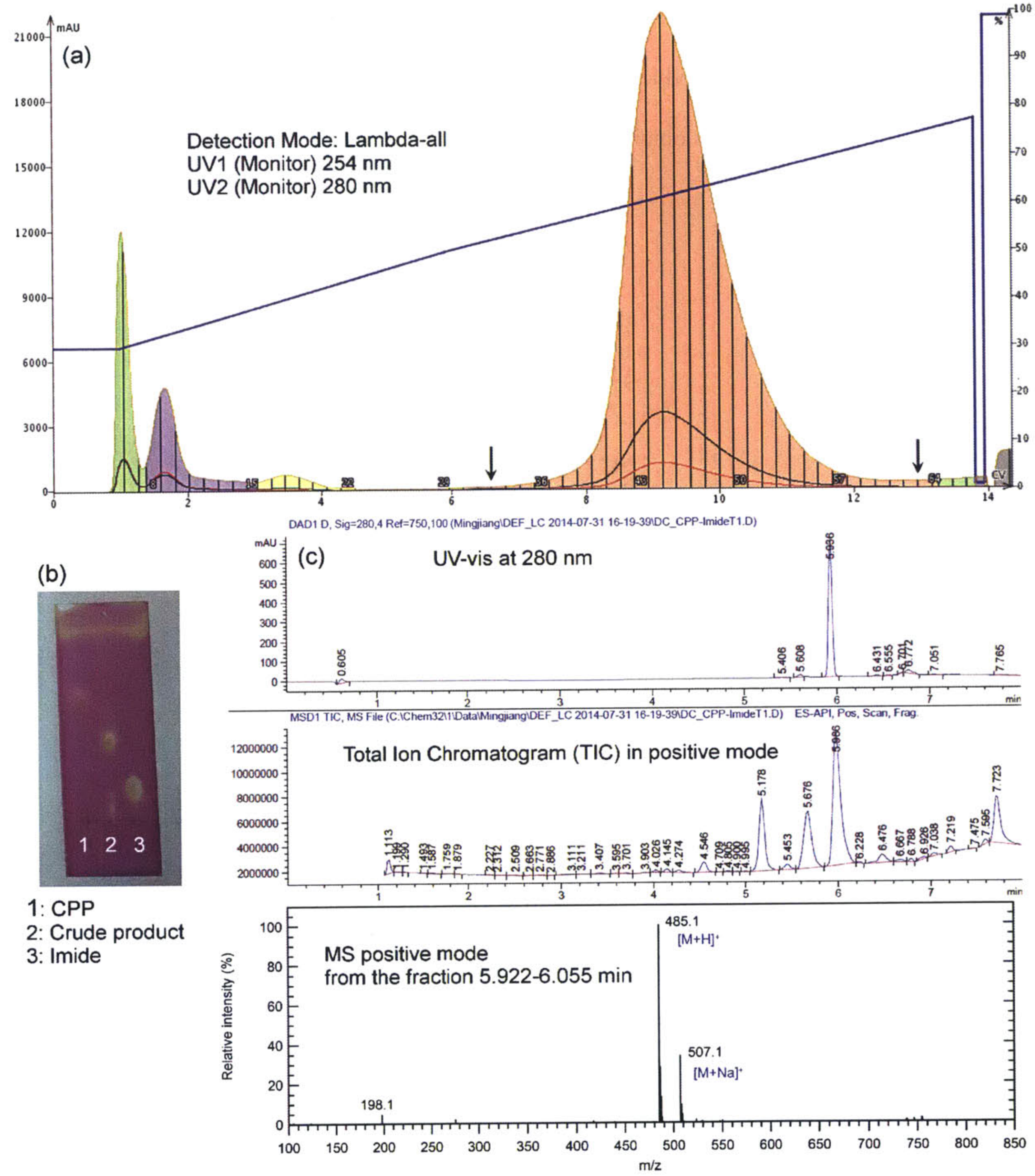

Figure 2-6. CPP-imide purification. (a) UV-vis spectra collected during chromatography in Biotage. Fractions from 33 to 63 were collected from this particular purification as marked by black arrows. (b) TLC results using 4:6 mixture of hexane and ethyl acetate as the mobile phase

showing CPP, crude product before chromatography, and Imide. (c) LC-MS result of the purified CPP-imide confirming the molar mass.

Poly(hydroxypropyl acrylate) (PHPA) Polymerization. Hydroxypropyl acrylate (95%, mixture of isomers, 2-hydroxy-1-propyl acrylate and 1-hydroxy-2-propyl acrylate) was purchased from Sigma-Aldrich. Inhibitors were removed by passing the liquid monomers through a basic alumina column. Typically, a glass column with 2 inch diameter was filled with approximately 300 mL of basic alumina. 20 mL of anhydrous sodium sulfate was poured on top of alumina layer to remove residual water from monomer. Approximately 350 mL of monomer was poured into the column and flowthrough was collected. Purified monomer was stored at -20 °C until needed. Azobisisobutyronitrile (AIBN) was recrystallized from methanol prior to use. Typically, 5 g of AIBN was dissolved in 50 mL of methanol and the solution was heated to boil. After 3-5 minutes, the solution was vacuum filtered to remove impurities. The filtrate was collected and cooled down to room temperature, and stored at 4 °C overnight for recrystallization. Crystals were collected by filtration, washed with cold methanol, and dried in vacuum oven overnight at room temperature shielded from light. Recrystallized AIBN was stored at -20 °C. RAFT polymerization of PHPA was carried out in acetonitrile at a 750: 1: 0.5 molar ratio of monomer/chain transfer agent (CTA)/AIBN for PHPA with M_n of 17.7 and 27.2 kg/mol, and at a ratio of 1600: 1: 1.45 for M_n of 57.0 kg/mol. All reactions were started with 40 g monomer at 2 M monomer concentration. Reaction mixtures were degassed by three freeze-pump-thaw cycles and initiated by plunging the flask into a pre-heated bath at 55 °C. The reaction was stopped by exposing the solution to the air and moving the flask to a cold water bath while stirring the solution for a few minutes to allow it to contact with the air. PHPA was precipitated three times after polymerization in a 1:1 mixture of hexane and ethyl acetate and thoroughly dried under vacuum at room temperature before deprotection. The polymerization time was optimized to limit the conversion to approximately 25-35% to minimize incorporation of the protected maleimide endgroup into the growing polymer chains. The conversion was checked by measuring the average molar mass of the polymer using gel permeation chromatography (GPC) after precipitation.

Synthesis of 2-(2-methoxyethoxy)ethyl acrylate (MEEA). MEEA monomer was synthesized following a protocol reported in literature (Scheme 2-3).[4] 36 g of 2-(2-methoxyethoxy)ethanol (300 mmol) and 37.9 g of triethylamine (375 mmol) were added to 200 mL of dry dichloromethane in an ice bath. 32.5 g of acryloyl chloride (360 mmol) mixed with 60 mL of dry dichloromethane was added to the reaction mixture dropwise while stirring to give an opaque yellow mixture. The reaction proceeded overnight at room temperature. The dark yellow solution was filtered to remove Et_3NCl salt and washed twice each with 0.1M HCl (aq) to remove base catalyst Et_3N, saturated $NaHCO_3$ (aq) to remove acrylic acid, and 0.5M NaCl (aq). The solution was dried over anhydrous Na_2SO_4 and the solvent was dried by rotary evaporation to obtain orange brown liquid. The flask was not submerged in a heated water bath so it remained cold as dichloromethane evaporated to minimize monomer evaporation and/or polymerization. Byproduct was further removed by flash chromatography in silica gel using a 1:1 mixture of hexane and ethyl acetate as eluent (Figure 2-7). All crude product that moved with the eluent was all collected with R_f approximately 0.7 in a 1:1 mixture of hexane and ethyl acetate. The collected solution was dried by rotary evaporation leaving a clear orange liquid. A small amount (typically 5 wt%) of hydroquinone was added to the crude product as an inhibitor, and the mixture was vacuum distilled at 300 mTorr at 60 °C or 150 mTorr at 90 °C. Everything evaporated was collected. Typically 40 g of clear liquid was collected leaving a small amount of byproduct in the original flask as a yellow solid. The product was diluted in 100 mL dichloromethane and washed four times with 50 mL of 0.1M KOH (aq) and with water as necessary to remove residual hydroquinone that evaporated during the distillation process. This extensive purification process was found to be necessary to produce a product that could yield low dispersity polymer products. A clear liquid was obtained after rotary evaporation (37.8g, 72%). ^{1}H NMR ($CDCl_3$, δ, ppm): 3.34 (3H, -OCH_3), 3.52 (2H, -$OCH_2C\mathit{H}_2OCH_3$), 3.61 (2H, -$OC\mathit{H}_2CH_2OCH_3$), 3.72 (2H, -$COOCH_2C\mathit{H}_2O$-), 4.27 (2H, -$COOC\mathit{H}_2CH_2O$-), 5.80 (1H, HHC=CH-), 6.12 (1H, HHC=CH-), 6.41 (1H, $H_2C=C\mathit{H}$-).

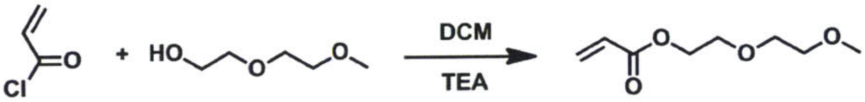

Scheme 2-3. Synthesis of MEEA monomer from acryloyl chloride and 2-(2-methoxyethoxy)ethanol.

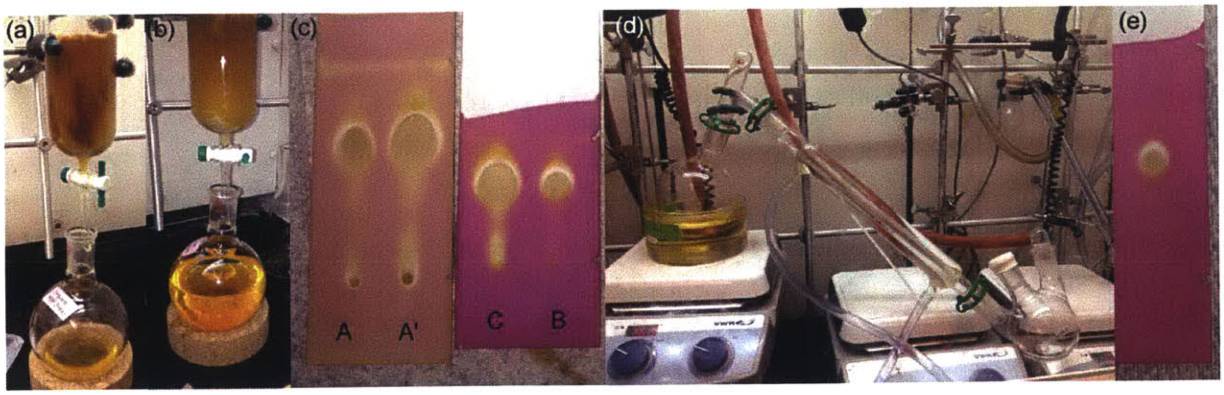

Figure 2-7. (a) MEEA monomer purification during flash chromatography and (b) after all flowthrough is collected. (c) TLC results showing the crude mixture before flash chromatography (A and A' with A' is twice concentrated), early flowthrough (B) and later

flowthrough (C) which are both collected for distillation. (d) A typical large scale distillation set-up. (e) TLC result of collected product after distillation. Mobile phase used for all TLC is a 1:1 mixture of hexane and ethyl acetate. Indentations in the TLC plates indicate the beginning and the end of chromatography.

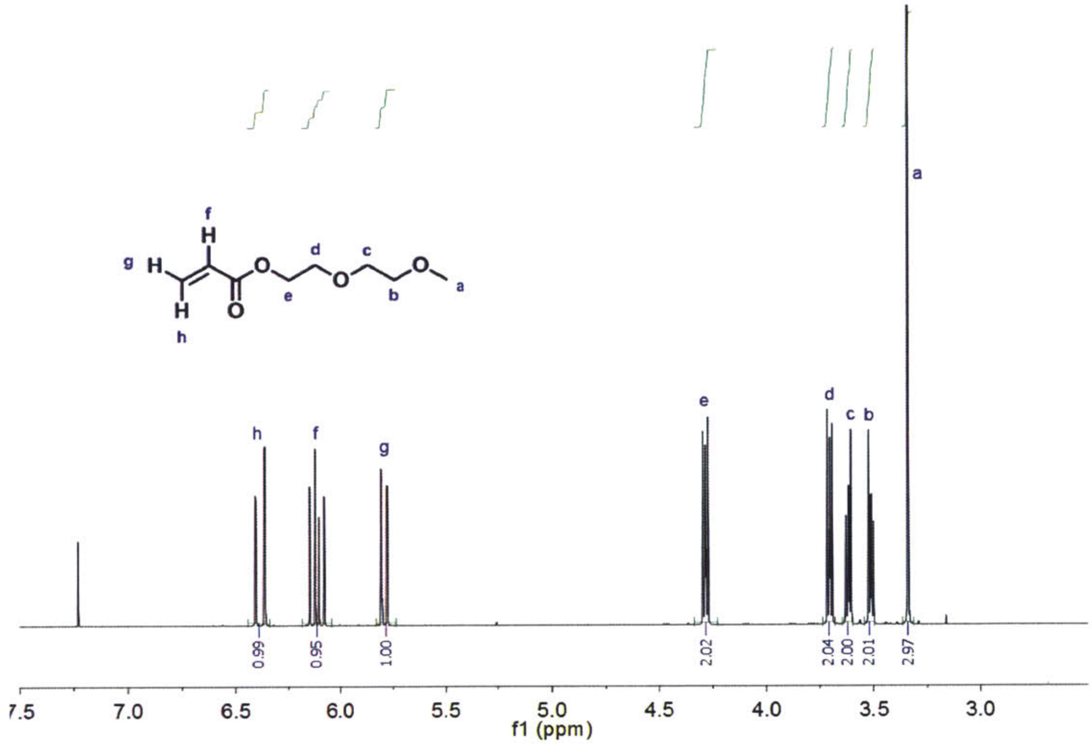

Figure 2-8. ^{1}H-NMR spectrum of MEEA monomer in $CDCl_3$ solution.

Poly(oligoethylene glycol acrylate) (POEGA) Polymerization. 2-methoxyethyl acrylate (98%) (MEA) was purchased from Sigma-Aldrich. Inhibitors were removed by passing the liquid monomers through a basic alumina column. The same chain transfer agent, EMP-imide, as the PHPA polymerization was used for POEGA polymerization. Azobisisobutyronitrile (AIBN) was recrystallized from methanol prior to use. RAFT polymerization of POEGA was carried out in dioxane at 55 °C with feed ratios of MEA/MEEA/CTA/initiator 270: 270: 1: 0.5 for M_n of 18.4

and 26.1 kg/mol, and 627: 660: 1: 0.5 for M_n of 57.6 kg/mol. POEGA was precipitated three times in hexane and thoroughly dried under vacuum at room temperature before deprotection.

Deprotection of PHPA and POEGA. The maleimide-protecting group was removed by a retro Diels-Alder reaction by heating the polymers to 120 °C for 2 hours under vacuum. To eliminate all detectable coupling between maleimide groups during deprotection, approximately 10 wt.% of butylated hydroxytoluene and hydroquinone were each added to the polymers prior to deprotection. Incomplete removal of inhibitors may affect downstream processes including protein activity after bioconjugation and polymer macrophase separation behavior; therefore, butylated hydroxytoluene was removed by precipitating PHPA and POEGA in 1:1 mixture of hexane/ethyl acetate and hexane, respectively, three times. Polymers were dissolved in plentiful water at 4°C and thermally precipitated three times to remove hydroquinone. The molar masses and dispersities (Đ) before and after deprotection show very minimal changes (Figure 2-9).

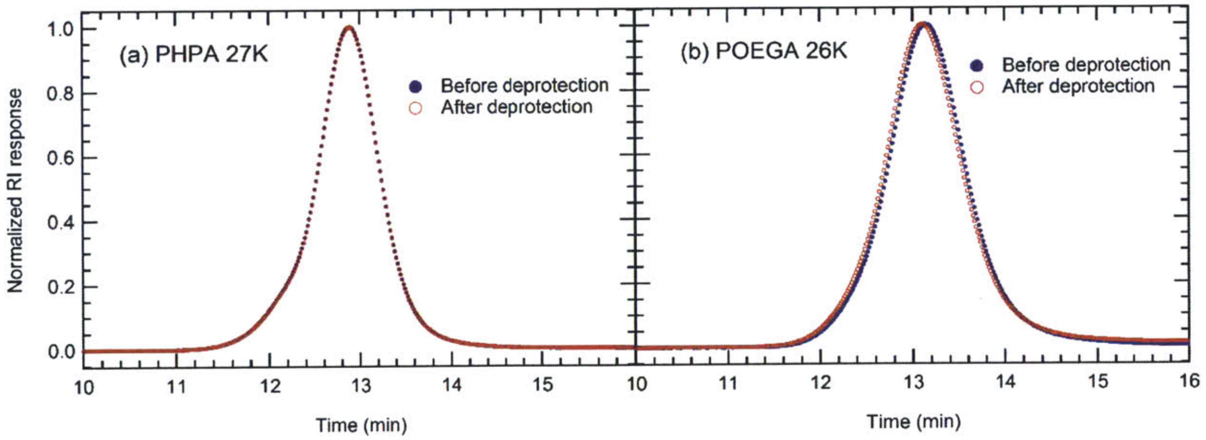

Figure 2-9. GPC traces of (a) PHPA 27K and (b) POEGA 26K homopolymers, before deprotection (blue closed circles) and after deprotection (red open circles), showing minimal changes.

PDMAPS Polymerization and Deprotection. 3-[*N*-(2-methacroyloyethyl)-*N*,*N*-dimethylammonio]propane sulfonate (DMAPS) monomer and an initiator 2,2'-azobis[2-(2-imidazolin-2-yl)propane]dihydrochloride (VA-044) were purchased from Sigma-Aldrich and Wako chemicals, respectively and used without further purification. RAFT polymerization of PDMAPS was carried out in trifluoroethanol. Typically 12 g of monomer was dissolved in the solvent at 0.5 M monomer concentration. DMAPS monomer, a chain transfer agent (CPP-imide), and initiator VA-044 were dissolved in trifluoroethanol at a ratio of 67: 1: 0.2 for a polymer with M_n of 33.9 kg/mol. After three freeze-pump-thaw cycles, the flask was filled with nitrogen and heated to 37°C to initiate polymerization. Polymerization was conducted overnight and terminated by opening the flask to the air. The mixture was precipitated first in acetone, and twice in methanol to obtain pink solid. The polymer was thoroughly dried in vacuum and deprotected at 150°C under vacuum overnight. The molar mass and dispersity (Đ) before and after deprotection show minimal changes (Figure 2-10). The higher temperature and longer reaction time were chosen based on a deprotection efficiency study conducted by monitoring peaks from maleimide and deprotection group in NMR spectra (Figure 2-11).

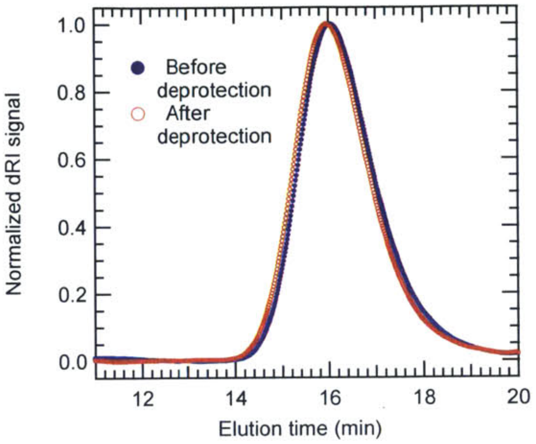

Figure 2-10. GPC traces of PDMAPS 29K homopolymer before deprotection (blue closed circles) and after deprotection (red open circles) showing minimal changes.

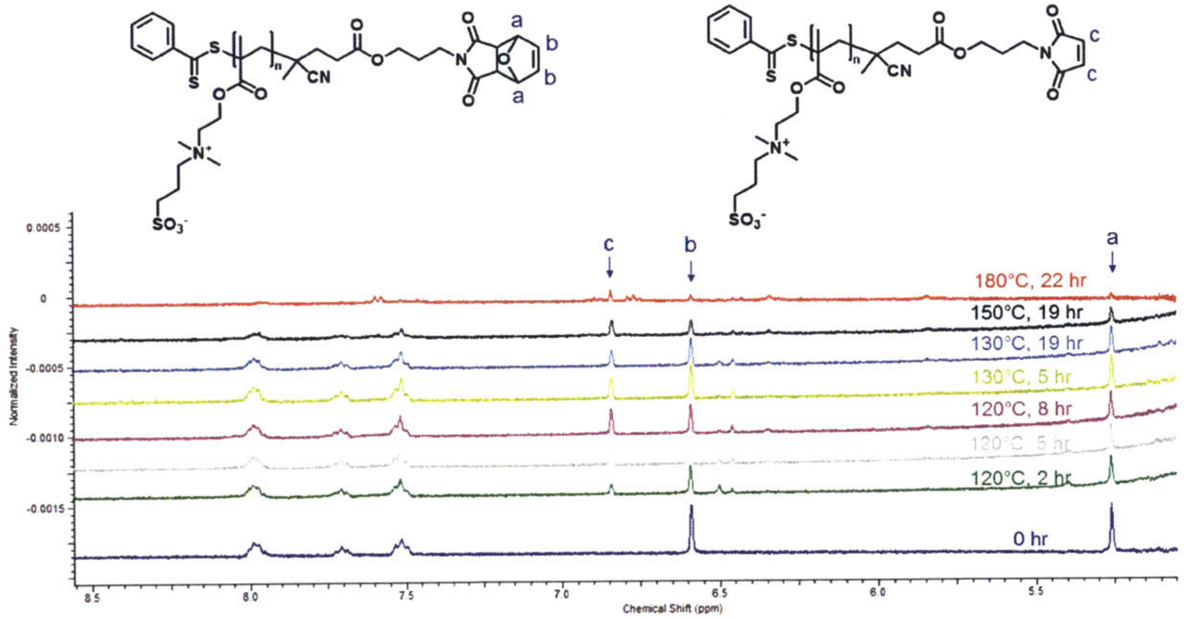

Figure 2-11. ^{1}H-NMR spectra showing efficiency of deprotection reactions of PDMAPS. PDMAPS with molar mass 8 kg/mol was used for the study, and D_2O was used for an NMR

solvent. Peaks indicated as a, b are from the deprotection group, and the peak indicated as c is from the maleimide end group.

2.2 Characterization of Synthetic Homopolymers

Gel Permeation Chromatography (GPC). The molar masses and dispersity (Đ) of the synthesized polymers were analyzed by gel permeation chromatography. An Agilent Technologies 1260 Infinity system using two ResiPore, 7.5 x 300 mm (Agilent Technologies) columns in *N,N*-dimethylformamide (DMF) with 0.02 M lithium bromide (LiBr) as the mobile phase was used for chromatography, and signals were collected from a Wyatt DAWN HELEOS II multi-angle light scattering detector and a Wyatt Optilab T-rEX refractometer. dn/dc values of PHPA and POEGA were measured using a built-in method (Polymers used for dn/dc measurement are expected to be thoroughly purified and dried to minimize error. Solutions are individually prepared at 3-5 mL scale instead of serial dilution.); experimentally determined values of 0.053 and 0.042 mL/g (Figure 2-12a) were used to obtain absolute molar masses. The molar mass and dispersity (Đ) of PDMAPS were analyzed using the same LC and detector systems with two PL Aquagel-OH MIXED-M 8 μm columns (Agilent Technologies) in 0.5 M NaCl (aq) with 0.02% sodium azide as the mobile phase. dn/dc value of PDMAPS was measured to be 0.1423 ± 0.0024 mL/g (Figure 2-12b).

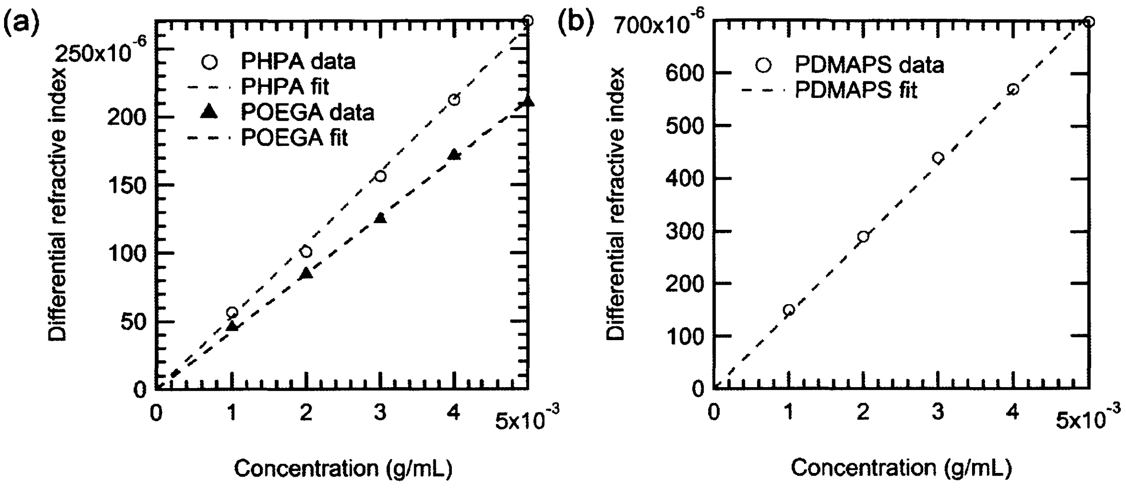

Figure 2-12. Plot of differential refractive index of (a) PHPA and POEGA, and (b) PDMAPS. dn/dc values are measured using a built-in batch mode software provided by Wyatt Technology. 1, 2, 3, 4, and 5 mg/mL of polymer solutions were prepared in *N,N*-dimethyl formamide containing 0.02 M LiBr (a), or in 0.5 M NaCl solution (b). The fitted lines are forced to intercept the origin. The dn/dc of PHPA was measured to be 0.0533 ± 0.0014 mL/g (R^2=0.9977) and that of POEGA was 0.0424 ± 0.0007 mL/g (R^2=0.9989). The dn/dc of PDMAPS was measured to be 0.1423 ±0.0024 mL/g (R^2=0.9979)

Nuclear Magnetic Resonance (NMR). ^{1}H-NMR was recorded on Bruker 400 MHz spectrometers at the MIT Department of Chemistry Instrumentation Facility (DCIF). Spectra were analyzed using Bruker TopSpin software at the facility, MNova Lite, or ACD/NMR Processor depending on the availability. PHPA and POEGA were dissolved in $CDCl_3$ and PDMAPS was dissolved in D_2O for analysis. Typically 128 scans were obtained for polymers and 32 scans for small molecules.

Cloud Point Measurements. The cloud points of the polymers were determined by measuring the transmittance of 1 wt.% polymer solutions (10 mg/mL) in water using UV-vis spectrometry. The temperature at which a 50% drop in the initial transmittance was observed was recorded as the cloud point according to reported methods in the literature.[5] Transmission at 500 nm was recorded with a temperature ramp from 5°C to 20°C and from 10°C to 30°C for PHPA and POEGA, respectively, at 0.2°C per minute. Temperature was controlled by T-app software and the temperature profile was recorded separately. The solution was heated first and cooled down. % Transmittance was obtained from $\%T = 100\,(10^{-A})$ (A: absorbance). The cloud point of PHPA measured is lower than reported values (Table 2-3), which can be attributed to the presence of the hydrophobic maleimide end group. An example transmittance recorded as a function of temperature ramp is shown in Figure 2-13.

Table 2-3. Comparison of cloud point values measured (first row) and reported in literature (second and third rows) for PHPA.

M_n (g/mol)	Dispersity	Concentration	Cloud Point (°C)	Method	Rate (°C/min)	Reference
27,220	1.22	1.0 wt%	11.4	50% of initial transmittance in first heating curve	0.2	Measured
11,100	1.21	1.0 wt%	21.4	50% transmittance point in first heating curve	1	5
N/A	N/A	10 %	16	N/A	N/A	6

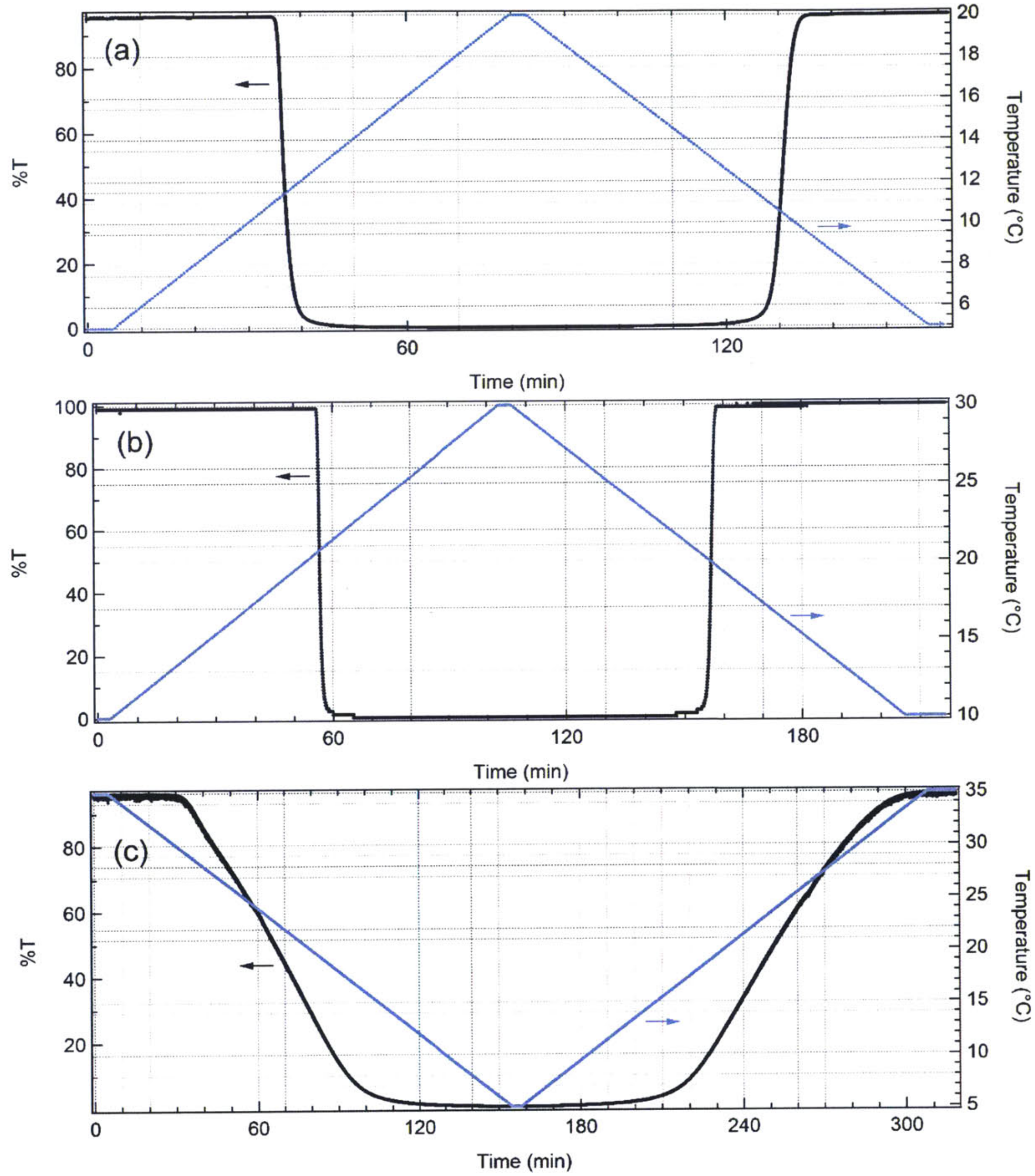

Figure 2-13. A transmittance (%T) measured with heating and cooling for (a) PHPA with M_n = 27,220 g/mol, (b) POEGA with M_n = 26,080 g/mol and (c) PDMAPS with M_n = 32,880 g/mol.

Due to the absorption of PDMAPS up to 600 nm (Figure 2-14a), the wavelength of 700 nm was used for determination of cloud points. 1 wt% PDMAPS solution in MilliQ water (10 mg/mL) was cooled from 35 °C to 5 °C and heated back to 35 °C at 0.2 °C per minute. The solution was stirred during measurement to prevent precipitation.

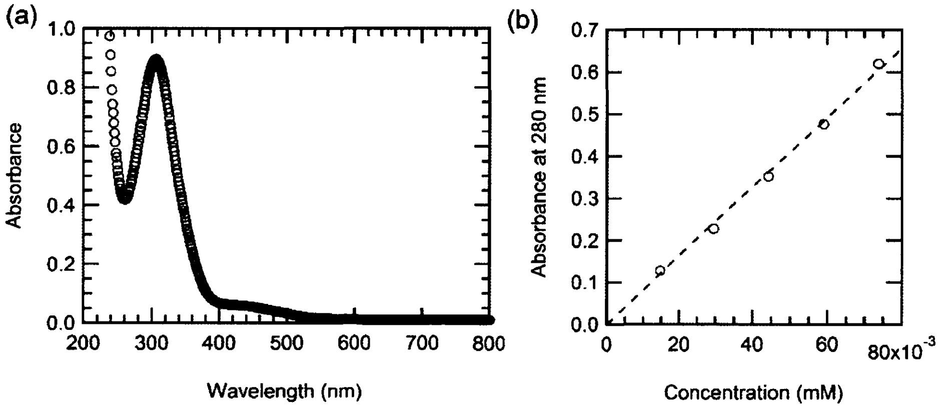

Figure 2-14. UV-vis absorption spectrum of PDMAPS and the determination of molar attenuation coefficient (ε). Solution of deprotected PDMAPS with M_n 32,800 and PDI 1.097 in MilliQ water was used for UV-vis measurements conducted at 35°C. (a) UV-vis absorption spectrum of 2.5 mg/mL of the polymer solution. (b) Absorbance at 280 nm as a function of polymer solution concentration 0.5, 1, 1.5, 2, and 2.5 mg/mL. Molar attenuation coefficient was determined to be 8,190 M^{-1} cm^{-1} based on the slope with the intercept forced to be zero.

PDMAPS Density Measurement. Density of PDMAPS was measured using two nonsolvents with known densities, dichloromethane with 1.326 and chloroform with 1.4788. The two solvents were mixed based on volumes and the final volume was measured using a graduated cylinder. The final density of mixture was estimated using the measured final volume and known densities of solvents. PDMAPS solid was finely ground using a mortar and pestle to minimize pores trapped in the solid that may result in underestimation of the density. PDMAPS powder was mixed with solvent mixtures and left undisturbed for a few hours (Figure 2-15). Density of PDMAPS was estimated to be 1.37 based on the result that the PDMAPS solid settled in the solvent mixture with density 1.363 while floated in the mixture with density 1.378.

Figure 2-15. PDMAPS (M_n 67,360, PDI 1.051) powder in various mixtures of organic solvents. From left to right, hexane (0.659), dichloromethane (1.326), 4:1 volume mixture of dichloromethane and chloroform (1.363), 3:1 volume mixture (1.378), 1:1 volume mixture (1.41), and chloroform (1.4788). Densities are indicated in parentheses.

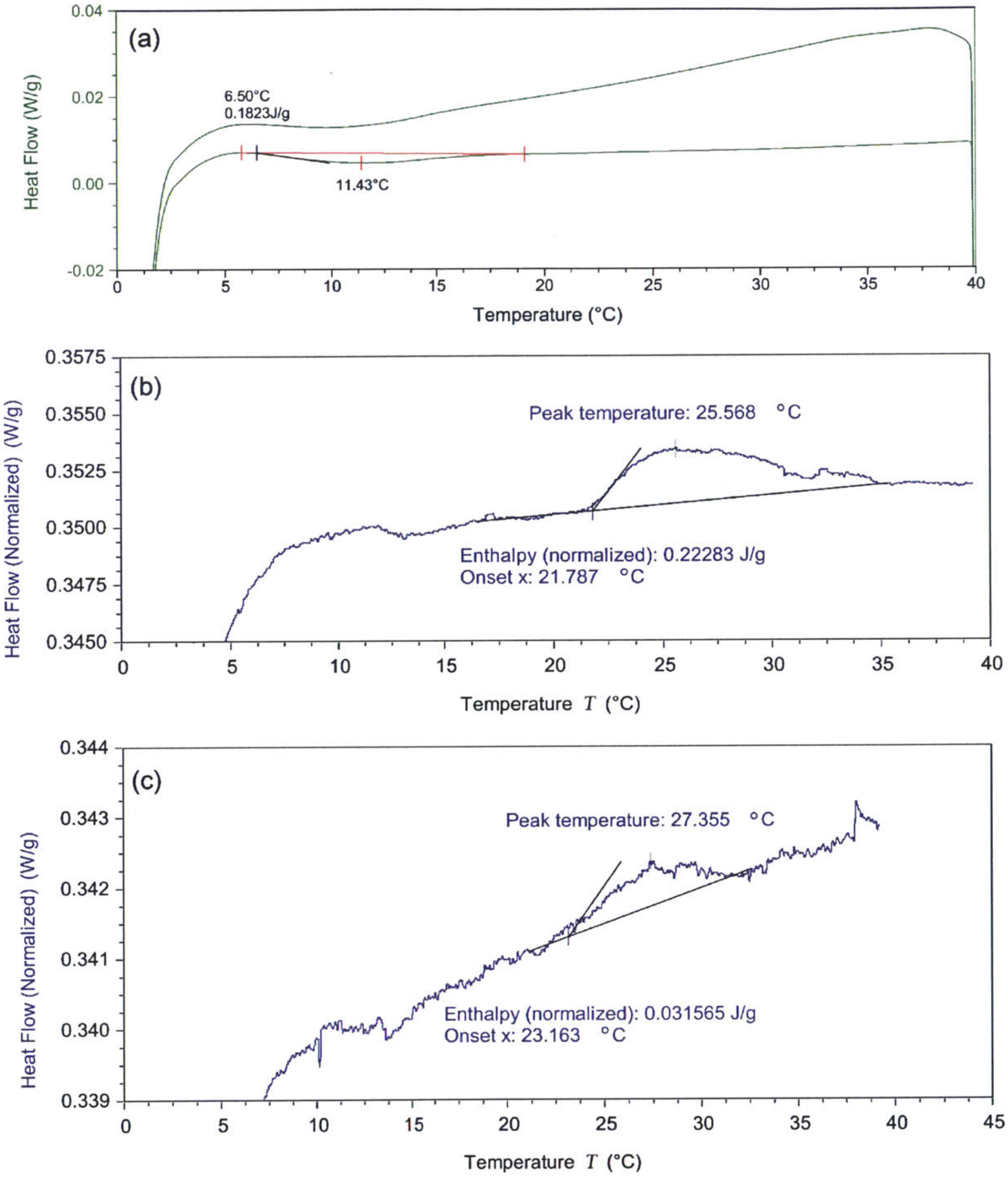

Figure 2-16. Differential scanning calorimetry (DSC) curves of (a) PHPA with M_n = 27,220 g/mol, (b) POEGA with M_n = 26,080 g/mol and (c) PDMAPS with M_n = 32,880 g/mol. Analysis is shown on the first heating curve of each polymer.

2.3 Bioconjugate Synthesis and Purification

Bioconjugation and purification of mCherry-PHPA and mCherry-POEGA. mCherryS131C protein expression and purification were conducted following the previously published protocol.[7] mCherryS131C containing N-terminal His-tag was expressed in the *E. coli* strain SG13009 containing the pREP4 repressor plasmid, grown in 2XYT media for 6 hours after induction using IPTG and harvested. The cells were resuspended in 100 mL of lysis buffer per L culture. 100 mg lysozyme per L culture was added to the solution and incubated on ice for 30 minutes. The solution was further sonicated on 50% duty cycle (output power 5) on ice for 15 minute. The lysate was clarified by centrifugation at 6,000 rpm (6,340 xg) for 10 minutes at 4°C using a F10S-6X500Y rotor. The recovered mCherryS131C solution in lysis buffer was bound to 10 g nickel resin per 100 mg protein for approximately 2 hours at 4°C on a rocker. Nickel affinity chromatography was performed at room temperature. Pure protein was collected by performing after removing flowthrough, washing the resin four times with 10 CV of wash buffer, eluting mCherryS131C four times with 1 CV of elution buffer (components of the buffers are listed in Appendix B). A denaturing SDS-PAGE gel showing a typical purification process is shown in Figure 2-17. Eluent was dialyzed into 20 mM Tris-Cl pH 8.0 buffer by changing buffer seven times, with an interval of at least three hours between changes, over 1-2 days. Protein concentration and activity were analyzed based on the ratio of absorbance at 586 nm and absorbance at 280 nm (A586/A280) using UV-vis spectroscopy (Figure 2-18). A586/A280 ratio is typically between 1.45 and 1.6, and typically 70-120 mg mCherryS131C is obtained per L culture. Protein concentration was calculated from absorbance based on the molar extinction coefficients (ε) of mCherryS131C which are 72,000 M^{-1} cm^{-1} at 586 nm and 32,550 M^{-1} cm^{-1} at 280 nm.

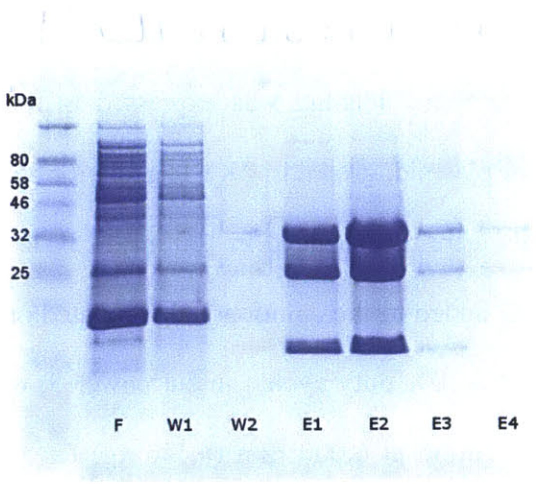

Figure 2-17. An SDS-PAGE gel showing fractions collected from mCherryS131C nickel affinity chromatography. mCherryS131C has a molar mass 28,134 Da, and two fragments with molar masses 19 kDa and 9 kDa are generated as a result of partial hydrolysis of chromophore acylimine bond.[8] F: flowthrough, W1: first washed fraction, W2: second washed fraction, E1-E4: eluted fractions. (The gel image is cropped to omit redundant lanes)

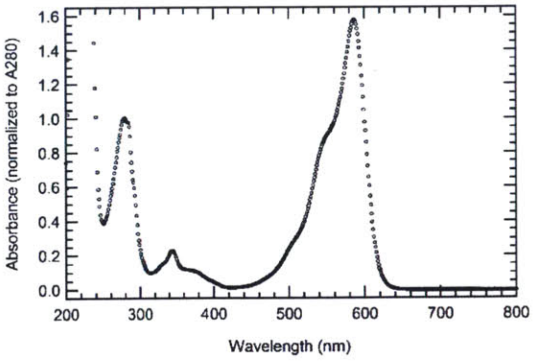

Figure 2-18. UV-vis spectrum of purified mCherryS131C in 20 mM Tris-Cl pH 8.0 buffer.

Prior to bioconjugation, the protein solution in 20 mM Tris-Cl pH 8.0 buffer is pre-incubated with 10-fold molar excess of 3,3′,3″-phosphanetriyltripropanoic acid hydrochloride (TCEP·HCl), based on concentration measured from A280, for 1 hour to reduce disulfide bonds. A 6-fold molar excess of solid deprotected PHPA or POEGA was added to the solution and the reactions were carried out for 2 days at 4 °C. The reaction mixture containing bioconjugate, unreacted proteins, and polymers, was diluted using 20 mM Tris-Cl pH 8.0 buffer to an mCherry concentration of 1 mg/mL. Bioconjugate and unreacted polymers were precipitated in 1 M ammonium sulfate by adding 3 M ammonium sulfate pH 8.0 buffer. The solution was centrifuged at 10,000 rpm (17,600 xg) for 30 minutes at room temperature, and the supernatant containing unreacted proteins was discarded. Typically the color of the first supernatant is dark pink indicating significant amount of unreacted mCherryS131C. For large scale bioconjugation reactions involving similar or greater than 100 mg of protein, precipitation process was repeated three times total. The color of supernatant becomes clearer as the precipitation process is repeated. After centrifugation, the recovered solid was resuspended in 20 mM Tris-Cl pH 8.0 buffer (at 1 mg/mL of protein concentration) at 4°C on a rocker, which typically takes 4-8 hours depending on the reaction scale (PHPA conjugate takes longer to dissolve). Ammonium sulfate precipitation process was repeated total three times to remove as much of unreacted proteins, and the third supernatant is typically very clear which suggests most of unreacted mCherryS131C is removed from the reaction mixture.

The resuspended mixture in 20 mM Tris-Cl pH 8.0 buffer was bound to 10 g of nickel resin per 100 mg protein at 4 °C on a rocker for 4 hours or overnight at maximum. Larger bioconjugates require longer binding time due to the steric hindrance of large polymer chains. Nickel affinity chromatography was performed similarly to the previous protein purification except that it was performed at 4°C and the buffers did not contain BME. Unreacted polymers were removed by washing the resin four times with 10 CV cold deionized (Milli-Q) water. The conjugate was eluted using 1 CV elution buffer (without BME) four times, and the solution was dialyzed into deionized (Milli-Q) water similarly as before 4 °C to remove excess imidazole. Typical SDS-PAGE gels showing the result of ammonium sulfate precipitations and affinity chromatography are shown in Figure 2-19 and Figure 2-20 for mCherry-PHPA 27K and mCherry-POEGA 26K conjugates, respectively. Purity of final bioconjugates was analyzed using SDS-PAGE and native PAGE gels (Figure 3-4). Function of the protein within the bioconjugates was spectroscopically analyzed based on the A586/A280 ratio (Figure 3-5c).

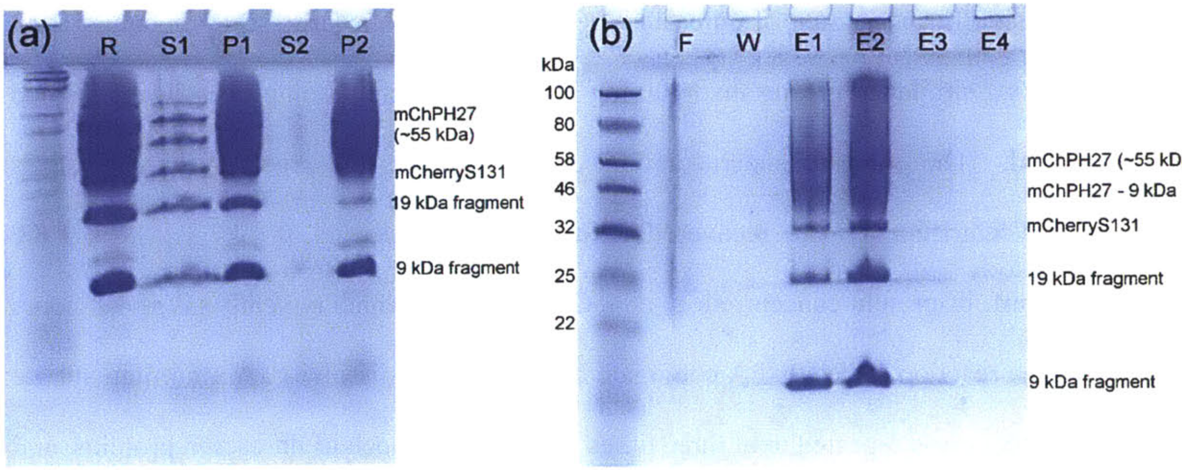

Figure 2-19. SDS-PAGE gels analyzed for mCherry-PHPA 27K bioconjugate purification. (a) SDS-PAGE gel from ammonium sulfate precipitation of mCherry-PHPA 27K conjugate from a large scale bioconjugation reaction (150 mg mCherryS131C was used for the reaction). From left to right, ladder, R: whole reaction mixture, S1: first supernatant, P1: first precipitate, S2: second supernatant, and P2: second precipitate are shown. (b) A representative SDS-PAGE gel

from Ni-NTA purification of mCherry-PHPA 27K bioconjugate. From left to right, ladder, F: flowthrough, W: wash, and E1-E4: elution 1-4 are shown.

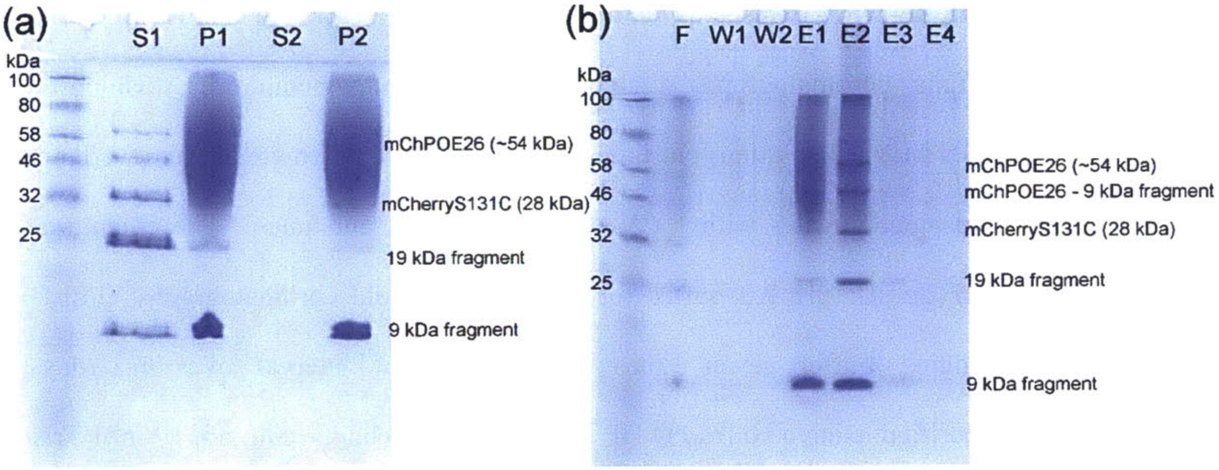

Figure 2-20. SDS-PAGE gels analyzed for mCherry-POEGA 26K bioconjugate purification. (a) SDS-PAGE gel from ammonium sulfate precipitation of mCherry-POEGA 26K conjugate from a test bioconjugation reaction (0.5 mg mCherryS131C was used for the reaction). From left to right, ladder, S1: first supernatant, P1: first precipitate, S2: second supernatant, and P2: second precipitate are shown. (b) SDS-PAGE gel from Ni-NTA chromatography of mCherry-POEGA 26K conjugate from a large scale bioconjugation reaction (mCherryS131C 230 mg was used for the reaction). From left to right, ladder, F: flowthrough, W1: wash 1, W2: wash 2, and E1-E4: elution 1-4 are shown.

Bioconjugation and purification of mCherry-PDMAPS. Prior to bioconjugation, mCherryS131C solution in 20 mM Tris-Cl pH 8.0 buffer is pre-incubated with 10-fold molar excess of TCEP·HCl, based on concentration measured from A280, for 1 hour to reduce disulfide bonds. A 7-fold molar excess of solid deprotected PDMAPS was added to the solution.

In order to increase polymer solubility, saturated sodium chloride solution was added to the reaction mixture to the final concentration 0.5 M NaCl. Reactions were carried out overnight at room temperature, and nickel resin was directly added to the reaction mixture at a ratio of 10 g of Ni resin per 100 mg mCherryS131C used. The mixture was put on a rocker at room temperature overnight. Nickel affinity chromatography was conducted at room temperature by washing the resin with 10 CV of 0.5 M NaCl solution four times to ensure all free polymers are removed, and elute free protein and bioconjugates with 1 CV of elution buffer four times. The eluent was dialyzed into 10 mM Tris-Cl pH 7.0 buffer for fast protein liquid chromatography (FPLC) purification by changing buffer seven times with three hour interval over 1-2 days. Bioconjugates were purified using a HiTrap Q HP 5 mL anionic exchange column, 10 mM Tris-Cl pH 7.0 as buffer A and 10 mM Tris-Cl 0.5 M NaCl pH 7.0 as buffer B in an AKTA pure FPLC system. Bioconjugate solutions were centrifuged at 10,000 rpm (corresponding to 11,617 xg in F15-8X50cy rotor) for 1 hour prior to loading to remove any precipitates. Depending on the volume of samples, either 10 mL injection loop or superloop was used. Injection volume was adjusted so that the amount of injected protein (including free protein and proteins in bioconjugates) did not exceed 120 mg per run. Smaller amount of loading usually resulted in purer conjugates due to better separation between free protein and bioconjugates. A slow gradient from 0 to 20% buffer B for 12 CV was applied to elute proteins, followed by a wash step for 10 CV at 20% buffer B. Free mCherryS131C moves much faster than bioconjugates at 20% buffer B which often corresponds to 10.86 mS/cm in conductivity, and a washing step longer than 10 CV is often beneficial. After ensuring as much of free mCherry was removed as possible, bioconjugate was eluted by fast gradient from 20 to 100% buffer B for 5 CV followed by 100% buffer B for 5 CV. A typical spectrum during the gradient program is shown in Figure

2-21 for mCherry-PDMAPS 33 kg/mol conjugate. While mCherry-PDMAPS 77K conjugate was purified similarly, separation between free mCherry and bioconjugate was much better due to the increased interaction of bioconjugate with the resin. Purity of fractions was analyzed using a denaturing protein gel (Figure 2-22) and the appropriate fractions were collected and dialyzed into deionized water.

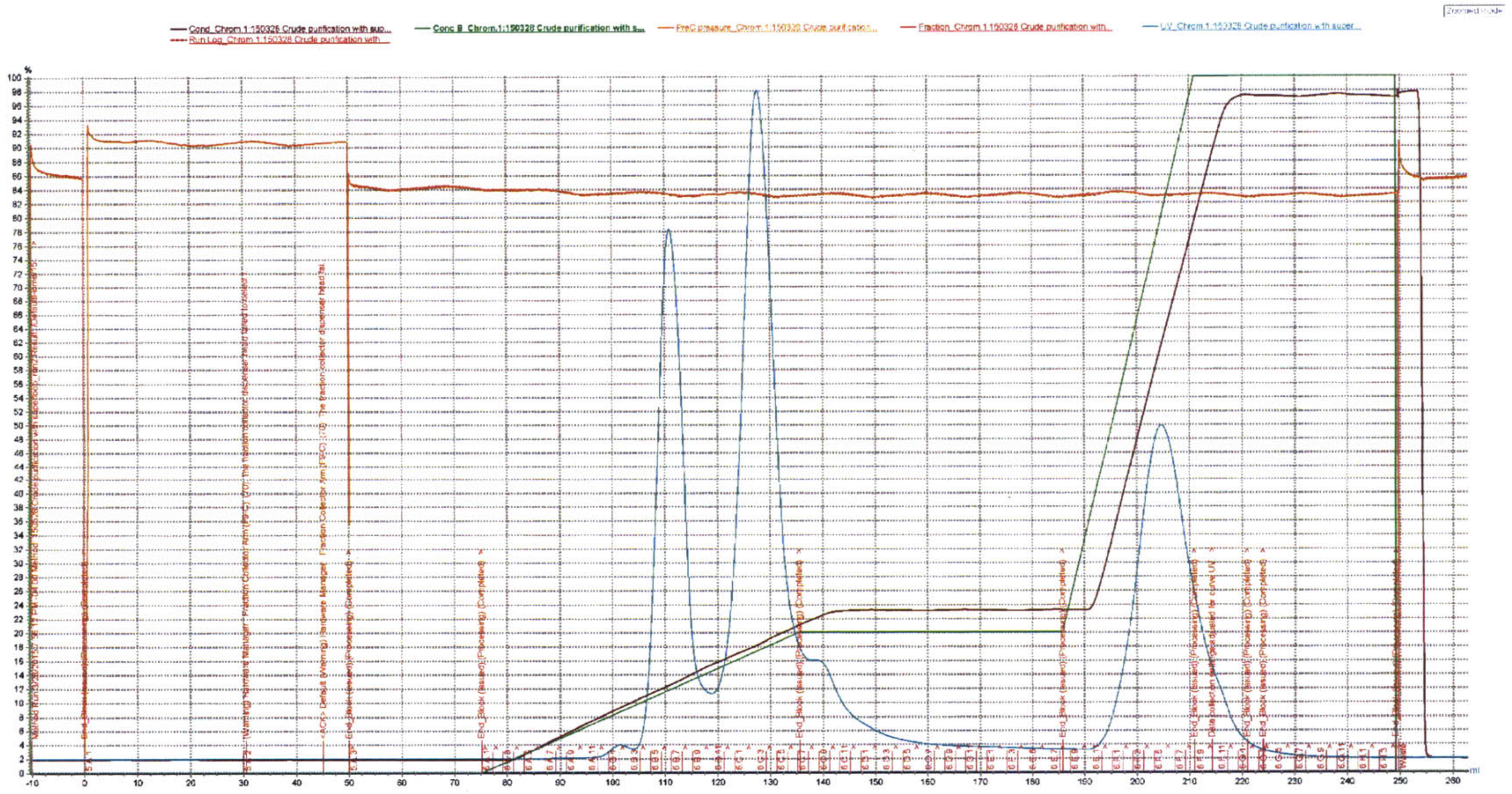

Figure 2-21. A color-coded representative FPLC spectrum for a purification of mCherry-PDMAPS bioconjugate. Brown solid line: conductivity, green solid line: concentration of buffer B (10 mM Tris-Cl 0.5 M NaCl pH 7.0), orange solid line: system pressure, cyan solid line: UV absorption, and red texts: run log and collected fractions. Fractions from E12 to G2 were collected from this run.

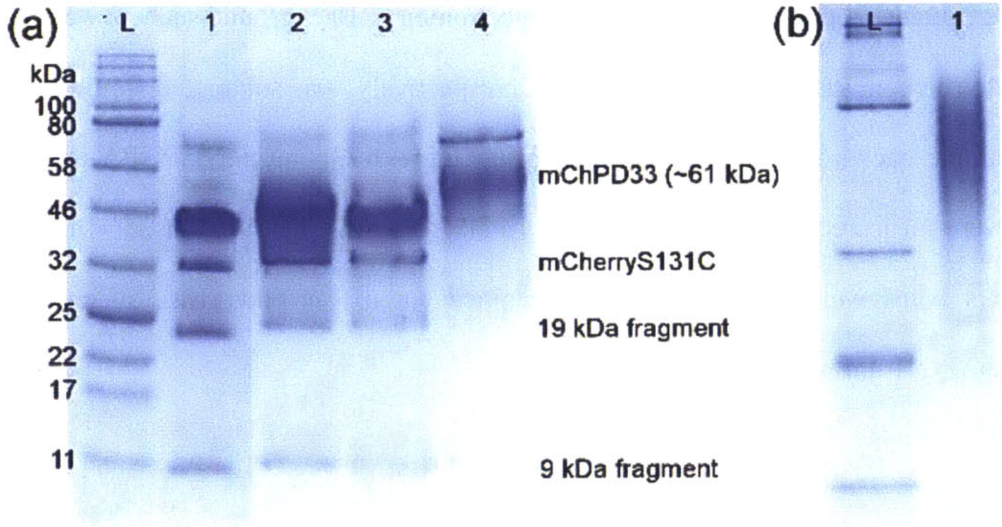

Figure 2-22. mCherry-PDMAPS 33K bioconjugate purification protein gels. (a) SDS-PAGE gel (+BME, no boil) of samples from the FPLC purification. L: ladder, 1: mCherryS131C, 2: flowthrough, 3: fraction D2, and 4: fraction D9. (b) Native protein gel showing L: ladder, and 1: the collected product from fractions E12-G2.

Circular Dichroism (CD). The secondary structure of free mCherryS131C and mCherry in bioconjugates was analyzed using an Aviv model 202 circular dichroism spectrometer at MIT Keating lab (for mCherry-PHPA and mCherry-POEGA) or MIT Biophysical Instrumentation facility (BIF) (for mCherry-PDMAPS). The CD spectrum of mCherry was measured in 20 mM Tris-Cl buffer (pH=8.0) while those of the bioconjugates were measured in water. Typically mCherry or bioconjugate solutions were diluted to have 0.5 mg/mL of protein concentration based on the UV-vis absorbance at 280 nm using 20 mM Tris-Cl buffer (pH=8.0) or MilliQ water, respectively, filtered using a 0.1 μm alumina-based Anopore membrane filter, measured using a quartz cuvette with 1 mm path length, and the actual protein concentration was measured afterwards for correction. Typically the concentration after filtration was measured to be 75%-95% of the initial concentration using UV-vis spectrometry. Background such as water and Tris-Cl buffer for bioconjugates and mCherryS131C, respectively, was subtracted from the measured data. Example background spectra are shown in Figure 2-23. mCherry-PHPA and mCherry-POEGA were measured at 5°C while mCherry-PDMAPS was measured at 35°C to ensure the both blocks were well-solvated. Signal obtained for 10 seconds was averaged at each wavelength with 1 nm wavelength step.

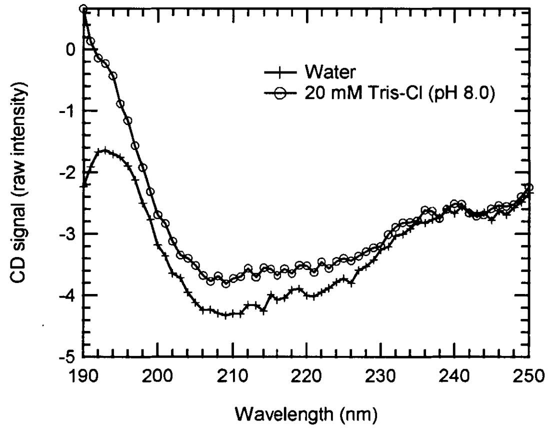

Figure 2-23. Example circular dichroism (CD) background spectra obtained at MIT Keating lab.

2.4 Nanostructure Characterization in Bulk

Purified bioconjugate solutions were concentrated to approximately 200 mg/mL using centrifugal filters with a molecular weight cut-off of 10 kDa. The solutions were cast in 20 μL aliquots on Teflon sheets and dried under dynamic vacuum at room temperature with a ramp rate of 50 Torr per hour until a final pressure of 10 Torr, followed by holding at this pressure overnight. The collected pellets were stored in a sealed tube shielded from light at 4°C until they were used. Pellets were dissolved in water or appropriate salt solution to prepare the desired concentrations of bioconjugate solutions for characterization. Hydration typically took 5-15 hours depending on the type of the polymer block and the bioconjugate concentration.

Small-angle X-ray scattering (SAXS) were carried out following the standard operating procedures at each beamline. SAXS measurements of mCherry-PHPA and mCherry-POEGA were performed at NSLS beamline X27C at Brookhaven National Laboratory (decay mode, X-ray wavelength 0.1371 nm, sample to detector distance 1750-1910 mm, and typical exposure time per scan 30 s). 2-D scattering patterns were radially averaged to obtain 1-D scattering curve, and converted to q space by using calibration parameters obtained using an silver behenate (AgBe) standard provided at the beamline. Background was subtracted from sample using the equation

$$I_{corrected} = \frac{1}{T_{sample} \cdot BC_{sample}} \left[\left(\frac{I_{sample} - I_{background}}{t_{sample}} \right) - \left(\frac{I_{dark} - I_{background}}{t_{dark}} \right) \right] - \frac{1}{T_{empty} \cdot BC_{empty}} \left[\left(\frac{I_{empty} - I_{background}}{t_{empty}} \right) - \left(\frac{I_{dark} - I_{background}}{t_{dark}} \right) \right]$$

where I is intensity, T is transmittance, BC is beam current, and t is time. Transmittance was calculated using $\mathrm{T}_{sample} = \frac{I_{t,sample}}{I_{i,sample}} \cdot \frac{I_{i,open}}{I_{t,open}}$ where I_t is the transmitted beam intensity and I_i is the incident beam intensity. A background scattering pattern was measured for a very short time such as 1 s, a dark scattering pattern was collected for the same amount of time as the sample exposure time with shutter closed, and an empty scattering pattern was collected from an empty washer backed with Kapton tapes on both sides for the same amount of time as sample exposure with shutter open. Incident and transmitted beam intensity were monitored from upstream and downstream detectors at the beamline, and the beam current was recorded from the facility provided monitor at the moment of measurement. Nanostructure of mCherry-PDMAPS were measured at Stanford Synchrotron Radiation Lightsource (SSRL) beamline 1-5 (top-off mode, X-ray energy 8 keV, sample to detector distance 2,970.04 mm, and typical exposure time per scan 180-210 s) and Advanced Photon Source (APS) beamline 12-ID-C,D at Argonne National Laboratory (top-off mode, X-ray energy 12 keV, sample to detector distance 2,259 mm, and typical exposure time per scan 0.5 s). Due to a problem with the transmitted beam intensity monitor, scattering patterns collected at SSRL were analyzed without correction for sample transmittance using an Igor package NIKA. Data collected at APS at beamline 12-ID-C,D were analyzed using a software provided at the beamline.

Equilibrium nanostructures measured by SAXS were typically studied with concentration variation between 30 and 70 wt.% with 10 wt.% increments, with selected additional measurements for more precise determination of order-disorder transition concentrations. The samples were studied at temperatures from 5 °C to 35 °C in 5 °C increments (or from 35 °C to 5 °C with 5 °C intervals in the case of mCherry-PDMAPS) and were equilibrated for 10 to 20 minutes after reaching a desired temperature depending on the heat transfer efficiency of a temperature controlling element at each beamline. Beam damage and phase equilibrium were checked by going back to a previous temperature and measuring the structure.

Depolarized light scattering (DPLS) and turbidimetry were conducted as previously described[7] and following the Olsen lab standard operating procedure on Birefringence. A Coherent OBIS LX660 laser with wavelength 662 nm and continuous wave output power of 20 mW was used. Hydrated samples (18-20 μL in total volume) were loaded into a 1 mm-thick Teflon mold which were then sandwiched between two quartz disks. For low viscosity samples, vacuum grease was applied between the mold and quartz disks to prevent a sample loss due to a leak. A LabVIEW program was used to record the detector signal and control the temperature of the connected chiller. A typical temperature program was the following: samples were equilibrated at the initial temperature for 10 minutes, ramped up or down to the final temperature at a rate 0.1°C/minute, held at the final temperature for 10-15 minutes, and ramped back to the original temperature at the same rate to check reversibility. The neutral density (ND) filter setting 2 was used for birefringence measurement and ND3 was used for turbidimetry to keep the detector signal in the order of 1. Measured birefringence signal was normalized to the power fraction (I_{PF}) following the equation shown below, where variables are defined as following; T_S is sample transmission calculated from the intensity measured by turbidimetry divided by I_{open}, I_B is sample birefringence signal, I_{dark} is the background "leak" detector signal, I_{cross} is the detector signal when the rear polarizer is set to be perpendicular to the laser polarization, and I_{open} is the laser intensity reading on the detector.

$$\mathrm{I} = \frac{1}{T_S}(I_B - I_{dark}) - (I_{cross} - I_{dark})$$

$$I_{PF} = \frac{I}{I_{open}}$$

2.5 Bioconjugate Thin Film Preparation and Characterization

Materials. Silicon wafers were purchased from Wafer World (P-type Silicon with boron as dopant, orientation: (100), single-side polished, test grade). A wafer was cut into halves, rinsed in acetone and treated with oxygen plasma at MIT Center for Material Science and Engineering (CMSE) for 5 minutes immediately before use. Poly(ethylene glycol) methyl ether (PEG) (M_n=750 g/mol) was purchased from Sigma-Aldrich. A cleaned wafer was submerged in PEG melt and heated at 150°C for 24 hours under vacuum to induce the thermal dehydration coupling reaction. Wafers were rinsed in acetone afterwards, briefly dried using house air, and stored in a sealed dish and used within a few days.

Thin Film Preparation and annealing. A flow coater was built following plans from a previously reported design.[9] A humidity chamber was custom-built around the flow coater (Figure 2-24b). Design of the chamber is shown in Figure 2-25.

Table 2-4. Parts list for flow coater. Alphabet symbols given in the last column are indicated in Figure 2-24 either in yellow or red.

Company	Item	Part Number	Purpose
Newport Corp	Angle Bracket (qty. 2)	360-90	Used for knife mount (A)
Newport Corp	Tilt and Roration Platform, 2 axis ± 4° tilt, ± 4° rotation	37	Knife-blade mount for blade angle to substrate surface (B)
Newport Corp	Quick-Mount linear stage, 12.7 mm x-axis travel	460A-X	Aluminum stage, ball bearing movement for knife-blade vertical height adjustment (C)
Newport Corp	High Precision small knob Adjustment Screw, 12.7 mm Travel, 100 TPI, Side lock	AJS100-0.5	High sensitivity of micrometers to stage adjustment (D)
axisNE	Screw driven automation table-404XR Series Precision Linear Positioners	404XR100-5718	Motorized stage (E)
axisNE	Copley Controls Stepnet stepper amplifier/controller	STP-075-07-BNC	Controller for communication between the motorized stage and computer software (F)
axisNE	24V Output Power Supply	S8VS18024	Power supply (G)
Machined	Aluminum plate for blade mount	-	For blade mount (H)
Machined	Aluminum platform	-	To match the height of the stage to the blade parts. Need to be very flat (I)

A 1-inch wide glass slide was cut into half using a general glass cutter along its long axis to generate 0.5-inch wide glass slide, which was used as a blade. The angle of the blade was fixed at 5° throughout experiments. After blade touches the substrate by visual inspection, the 100 TPI fine adjustment screw (254 μm per revolution) that controls the z-position of the blade was turned 180° clockwise to lift the blade by 127 μm. 4 μL of bioconjugate solution of concentration from 15 wt.% to 30 wt.% was injected between the blade and the substrate using a fine tip gel loading pipet. Wet films were prepared by moving the stage at a constant speed using CME2 software provided by Copley Controls. Films were allowed to dry in the humidity chamber which was almost instantaneous for relative humidity 10% and took seconds for 80%. Films were taken out to ambient air afterwards. Flow coating was conducted at room temperature. Relative humidity was measured using a VWR digital hygrometer (part number 35519-046, temperature range 0 to 50°C, humidity range 25 to 95% RH, 0.1°C and 1% RH resolution).

Figure 2-24. A photo of flow coater (a) with parts symbols in Table 2-4 indicated, and humidity chamber (b) used for control of humidity during thin film preparation.

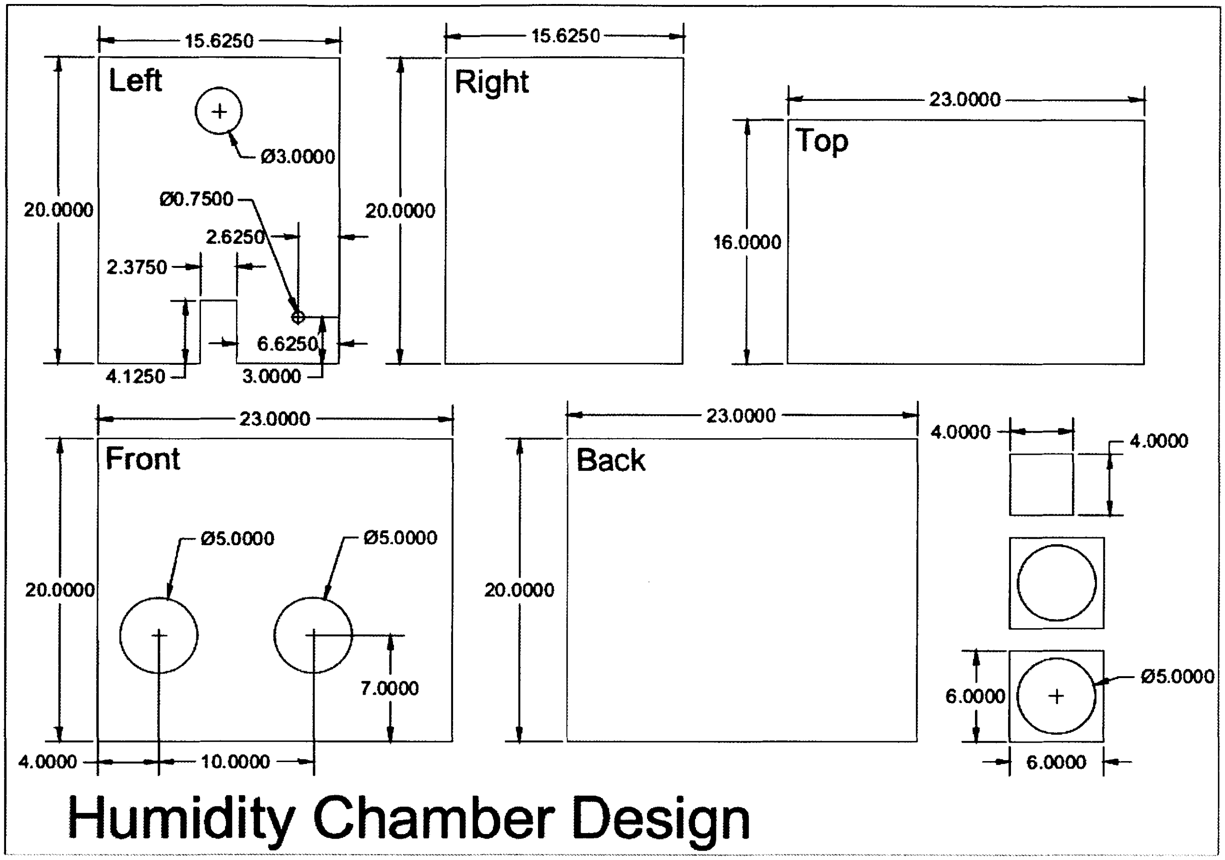

Figure 2-25. Design of humidity chamber. Units are shown in inches. Polyethylene terephthalate glycol-modified (PETG) sheets are cut along the blue lines using a waterjet.

For annealing, films were immediately cut into small pieces with an approximate dimension 1 cm by 1 cm, and annealed on a 50 mL beaker put upside down in a 180 mL glass jar filled with 5 mL of 0.5 M NaCl solution (Figure 2-26). The lid for the glass jar was opened to terminate annealing process and the films were stored at ambient condition for a few hours to dry. Films were stored in a sealed 6-well plate afterwards, where the structure as measured by GISAXS was stable for at least 5 months as shown in Figure 2-27.

Figure 2-26. A typical annealing chamber set up. Left: side view, right: top view.

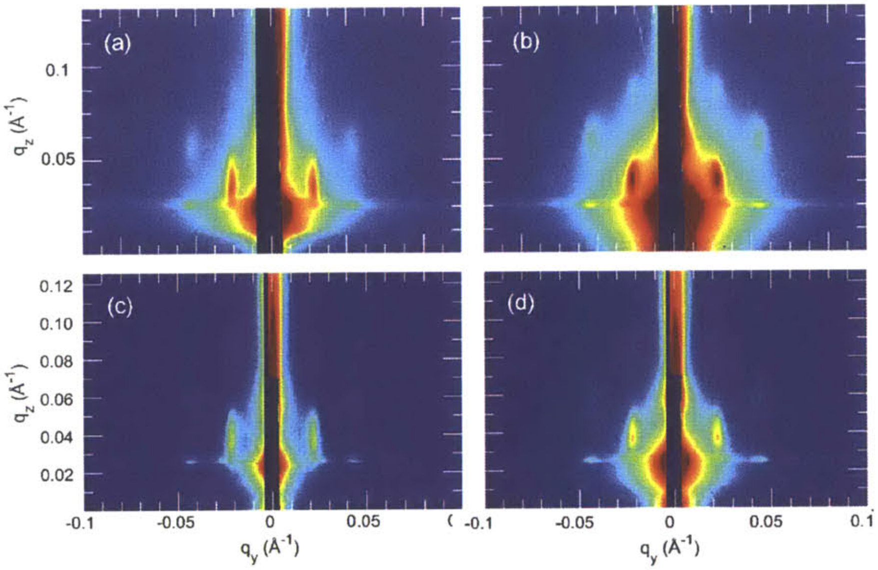

Figure 2-27. GISAXS images of 55 nm thick film prepared at 80% humidity with 15 mm/min coating speed measured initially within a week after film preparation (a) and measured after 5 months of storage in a sealed container (c). 104 nm thick film prepared at 80% humidity with 50 mm/min speed measured initially (b) and after 5 months (d).

Thin Film Characterization. X-ray photoelectron spectroscopy was conducted using PHI Versaprobe II XPS with a monochromated Al source (50W) with a spot size 200 μm. Chemical composition was analyzed from data measured at three different positions in a film to account for statistical variation across the film surface. Data were corrected using manufacturer-supplied relative sensitivity factors, smoothed using the SG7 mechanism, and background subtracted to integrate for quantification. Data were calibrated based on binding energy of aliphatic carbon 285.0 eV unless noted otherwise. Depth profiling experiments were conducted using a C60 cluster-ion gun operated at 10 kV and 10 nA with a raster scan size 4 by 4 mm and sputtering time with 1 minute interval.

The surface morphologies were studied using a NT-MDT Ntegra Prima scanning force microscope (SFM) in intermittent contact mode. NCHR Pointprobe® probes from NanoWorld (average resonance frequency 320 kHz, force constant 42 N/m), HQ:NSC15/Al BS probes from μmasch (average resonance frequency 325 kHz, force constant 40 N/m), and HQ:NSC16/Al BS probes also from μmasch (average resonance frequency 190 kHz, force constant 45 N/m) were mainly used for imaging depending on the success of imaging. The resonance frequency of an atomic force microscopy (AFM) tip was tuned at magnitude 10 or 20, and the tip was engaged to the surface by soft approach function in the software with 5% MagErr and 2.0 gain. When soft approach failed, the tip was manually landed at a setpoint that was 70-80% of the free amplitude. Typically 2 by 2 μm images with 256 points were obtained using gain 0.5 and scan rate 1.0 Hz. Imaging conditions including setpoint, gain, scan rate, and scan direction as well as scanning location were varied according to the image quality. Possibly due to the interactions between the tip and bioconjugate film surfaces, engaging the tip was difficult and phase imaging was often unsuccessful. The phase images were post-processed using first order corrections and the height image was processed using fifth order corrections.

Film thicknesses were measured using a spectroscopic ellipsometer (J.A. Woollam Co., INC XLS-100) at MIT Institute for Soldier Nanotechnologies (ISN). Data were collected at all wavelengths with 100 rev/meas, but data from wavelengths between 800 nm and 1,000 nm were used when analyzing bioconjugate films to avoid the mCherry absorption/emission range. In the WVASE32® software, a bioconjugate film layer was added as a Cauchy layer on top of a Silicon layer with 1 mm thickness (thickness of Si is not important) and an SiO_2 layer of which thickness was determined from a bare silicon substrate (typically 2-3 nm). The index of refraction (n) of mCherry-POEGA bioconjugate films was first determined from a film with a known thickness (36.6 nm, from AFM measurement). n was parameterized as a slowly decaying function of wavelength such that $n(\lambda) = A + \frac{B}{\lambda^2} + \frac{C}{\lambda^4}$ (λ in μm). The parameters A, B, and C determined from the film were 1.605 ± 0.168, 0.1747 ± 0.256, and -0.086051 ± 0.0969, respectively. Then thickness was fit using the fixed A, B, and C values. Thicknesses measured from three different spots within a film were averaged to account for spatial variation.

Grazing incidence small angle X-ray scattering (GISAXS) experiments were conducted at beamline 8-ID-E at Argonne National Laboratory using X-rays with energy 7.35 keV. Samples were measured under ambient conditions at two incident angles (α_i) 0.20 and 0.22° between the critical angle of silicon, 0.24°, and the critical angle of bioconjugate film, 0.18°, and the reported images are from an incident angle 0.20°. Samples were exposed for 20 seconds in each acquisition, and two images obtained at two different detector positions were combined to fill the gaps in the detector. Sample to detector distances (SDD) were 1,474 mm for most of data collected in November 2014 and 2,154 mm for annealed films collected in April 2015. Data were analyzed using GIXSGUI software package written by one of the beamline scientists, Zhang Jiang. Data were converted to q space by applying correction parameters (stored as .MAT file format) provided by the beamline scientists.

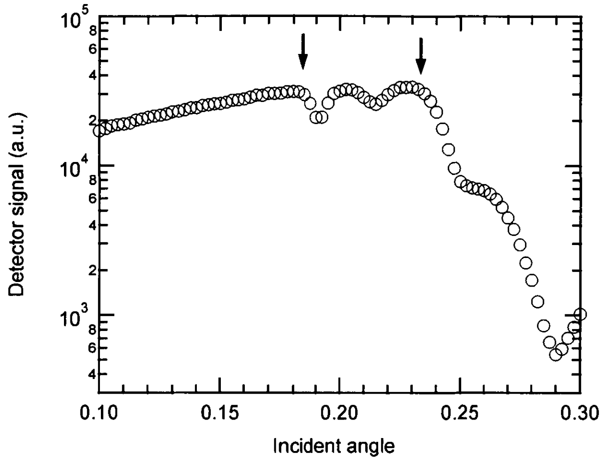

Figure 2-28. A representative X-ray reflectivity scan obtained from a film coated from a 20 wt.% mChPOE26 bioconjugate solution at 10% relative humidity with thickness 71.5 nm. The black arrow indicates the critical angle of Si substrate (~0.24°) and the blue arrow indicates the critical angle of the bioconjugate film (~0.18°).

2.6. References

(1) Thomas, C. S.; Glassman, M. J.; Olsen, B. D. Solid-State Nanostructured Materials from Self-Assembly of a Globular Protein-Polymer Diblock Copolymer. In *ACS Nano*; American Chemical Society, 2011; Vol. 5, pp. 5697–5707.

(2) You, Y.-Z.; Oupicky, D. Synthesis of Temperature-Responsive Heterobifunctional Block Copolymers of Poly(ethylene Glycol) and poly(N-Isopropylacrylamide). *Biomacromolecules* **2007**, *8*, 98–105.

(3) Neubert, B. J.; Snider, B. B. Synthesis of (±)-Phloeodictine A1. *Org. Lett.* **2003**, *5*, 765–768.

(4) Hua, F.; Jiang, X.; Li, D.; Zhao, B. Well-Defined Thermosensitive, Water-Soluble Polyacrylates and Polystyrenics with Short Pendant Oligo(ethylene Glycol) Groups Synthesized by Nitroxide-Mediated Radical Polymerization. *J. Polym. Sci. Part A Polym. Chem.* **2006**, *44*, 2454–2467.

(5) Eggenhuisen, T. M.; Becer, C. R.; Fijten, M. W. M.; Eckardt, R.; Hoogenboom, R.; Schubert, U. S. Libraries of Statistical Hydroxypropyl Acrylate Containing Copolymers with LCST Properties Prepared by NMP. *Macromolecules* **2008**, *41*, 5132–5140.

(6) Taylor, L. D.; Cerankowski, L. D. Preparation of Films Exhibiting a Balanced Solutions-A Study of Lower Consolute Behavior. *J. Polym. Sci.* **1975**, *13*, 2551–2570.

(7) Lam, C. N.; Olsen, B. D. Phase Transitions in Concentrated Solution Self-Assembly of Globular Protein–polymer Block Copolymers. *Soft Matter* **2013**, *9*, 2393.

(8) Pakhomov, A. A.; Pletneva, N. V; Balashova, T. A.; Martynov, V. I. Structure and Reactivity of the Chromophore of a GFP-like Chromoprotein from Condylactis Gigantea. *Biochemistry* **2006**, *45*, 7256–7264.

(9) Stafford, C. M.; Roskov, K. E.; Epps, T. H.; Fasolka, M. J. Generating Thickness Gradients of Thin Polymer Films via Flow Coating. *Rev. Sci. Instrum.* **2006**, *77*, 1–7.

Chapter 3. Effect of Polymer Chemistry on Globular Protein-Polymer Block Copolymer Self-Assembly

Polymer Chemistry 2014,5, 4884-4895, DOI: 10.1039/C4PY00448E - Reproduced by permission of The Royal Society of Chemistry

3.1 Abstract

Bioconjugates of the model red fluorescent protein mCherry and synthetic polymer blocks with different hydrogen bonding functionalities show that the chemistry of the polymer block has a large effect on both ordering transitions and the type of nanostructures formed during bioconjugate self-assembly. The phase behavior of mCherry-*b*-poly(hydroxypropyl acrylate) (PHPA) and mCherry-*b*-poly(oligoethylene glycol acrylate) (POEGA) in concentrated aqueous solution shows that changes in polymer chemistry result in increase in the order-disorder transition concentrations (C_{ODT}s) approximately 10-15 wt.% compared to a previously studied globular protein-polymer block copolymer, mCherry-*b*-poly(*N*-isopropylacrylamide) (PNIPAM). The C_{ODT}s are always minimized for symmetric bioconjugates, consistent with the importance of protein-polymer interactions in self-assembly. Both mCherry-*b*-PHPA and mCherry-*b*-POEGA also form phases that have not previously been observed in other globular protein-polymer conjugates: mCherry-*b*-PHPA forms a cubic phase that can be indexed to $Ia\bar{3}d$ and mCherry-*b*-POEGA displays coexistence of lamellae and a cubic $Ia\bar{3}d$ structure over a narrow range of concentration and temperature. Several common behaviors are also revealed by comparison of different polymer blocks. With increasing concentration and temperature, ordered phases always

appear in the order lamellar, cubic/PL, and hexagonal, although not all phases are observed in all materials. High concentration solutions (near 80 wt.%) also undergo a re-entrant order-disorder transition to form nematic liquid crystalline phases, regardless of the polymer block chemistry.

3.2 Introduction

There is great interest in incorporating a variety of proteins into bio-based materials to capture their high catalytic activity or specific molecular recognition ability. Potential applications include biocatalysts,[1,2] biosensors,[3–5] and bioelectronic devices using electrocatalytic or photoelectric materials.[6,7] These protein-based biomaterials can benefit from control over the nanoscale arrangement of the proteins because it promotes proper orientation of proteins, facile transport of materials (substrates, products, or charges), and improved stability and longevity of folded protein structures.[8,9] Both top-down approaches that combine lithographic techniques with protein immobilization chemistry and bottom-up approaches including block copolymer templating methods[10–14] have been demonstrated to pattern proteins on the nanometer length scale in 2-D and 3-D. While lithographic techniques are capable of achieving very precise spatial control, patterning is limited to two dimensions, and the resultant protein density per unit area is relatively low. Methods using diblock copolymers or lipids to template proteins can achieve relatively high protein density, but the majority of the material is typically template polymer, reducing the total functional density of protein.

The direct self-assembly of bioconjugates where a protein and a water-soluble polymer block are conjugated to form a block copolymer is a promising method that can potentially meet the design criteria for materials incorporating globular proteins and enzymes.[15–17] It can achieve high three-dimensional density, connectivity of domains, and control over nanoscale morphology and protein orientation.[15] In addition, the need for the use of harsh organic solvents is eliminated. Despite many advances in protein-polymer bioconjugate chemistry,[18–20] the majority of studies of globular protein-polymer conjugates have focused on dilute solution self-assembly behavior. Proteins conjugated to thermoresponsive polymers form spherical aggregates[21–23] including micelles and vesicles for applications in drug delivery. More complex architectures including toroids and figure eight structures have been reported from triblock conjugates composed of a globular protein and a diblock copolymer.[24]

Introduction of a globular protein as one block in a diblock copolymer results in significant changes in the phase behavior of the materials due to the effects of the globular protein shape and surface interactions (hydrophobic, ionic, and hydrogen bonding interactions).[25] Using a model protein-polymer conjugate block copolymer, mCherry-*b*-poly(*N*-isopropylacrylamide) (PNIPAM), it was observed that lamellar phases are favoured for coil fractions greater than 0.5 while hexagonal phases are favoured at lower coil fractions. A small region of hexagonally perforated lamellae was also observed near a coil fraction of 0.5. The order-disorder transition concentration (C_{ODT}) for mCherry-*b*-PNIPAM reaches a minimum for near-symmetric polymer volume fractions, suggesting that repulsive protein-polymer interactions contribute to the self-assembly of globular protein-polymers. Unexpectedly, re-entrant order-disorder transition (ODT) behavior is observed such that the bioconjugate becomes disordered at very high solution concentrations. This phase behavior is significantly different than traditional coil-coil block copolymers.[26–28]

Herein, the role of polymer chemistry and protein-polymer interactions on the self-assembly of mCherry-polymer bioconjugates is explored. Because hydrogen bonding is one of the key interactions between proteins and polymers, it is hypothesized that changing hydrogen bonding may enable differences in self-assembly to be observed due to changes in protein-polymer interactions. Therefore, conjugate block copolymers are prepared from poly(hydroxypropyl acrylate) (PHPA) and poly(oligoethylene glycol acrylate) (POEGA), polymers specifically chosen to have lower critical solution temperature (LCST) behavior similar to PNIPAM but different hydrogen bonding patterns. PHPA is a hydrogen bond donor and acceptor based on hydroxyl and ester groups instead of amide groups, and POEGA is a hydrogen bond acceptor only. PHPA and POEGA have lower critical solution temperatures (LCSTs) which enable control of solvent-mediated polymer interactions using temperature. It is shown that these changes in polymer chemistry have a large effect on the protein-polymer conjugate phase behavior, yielding an important path for structure control in bioconjugate materials and insights into the fundamental physics governing their self-assembly.

3.3 Experimental Methods

Materials and **Synthesis of MEEA** are described in detail in Chapter 2.

RAFT polymerization of PHPA and POEGA. The chemical structures of polymers used in this study and their polymerization reactions are illustrated in Scheme 3-1. Synthesis of the chain

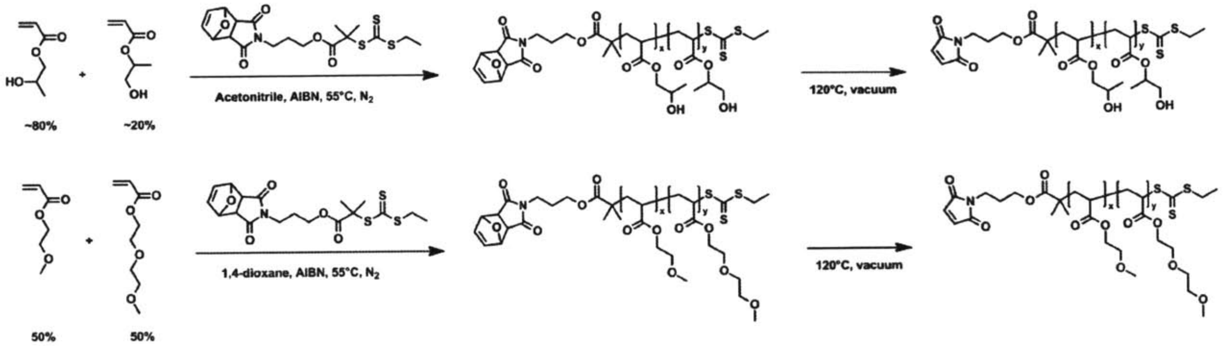

Scheme 3-1. Synthesis of poly(hydroxypropyl acrylate) (PHPA; top) and poly(oligoethyleneglycol acrylate) (POEGA; bottom) by RAFT polymerization.

transfer agent (CTA) with a protected maleimide group and reversible addition-fragmentation chain transfer polymerization were conducted similarly to previous work.[29] Reversible addition-fragmentation chain-transfer (RAFT) polymerization of PHPA was carried out in acetonitrile at a 750: 1: 0.5 molar ratio of monomer/CTA/AIBN for polymers with M_n of 17.7 and 27.2 kg/mol, and at a ratio of 1600: 1: 1.45 for M_n of 57.0 kg/mol. All reactions were started with 40 g monomer at 2 M monomer concentration. Reaction mixtures were degassed by three freeze-pump-thaw cycles, initiated by heating to 55°C, and stopped before reaching a conversion of 30% to minimize incorporation of the protected maleimide endgroup into the growing polymer chains. RAFT polymerization of POEGA was carried out in dioxane with all other conditions the same as PHPA polymerization. Feed ratios of MEA/MEEA/CTA/initiator were 270: 270: 1: 0.5 for polymers with M_n of 18.4 and 26.1 kg/mol and 627: 660: 1: 0.5 for M_n of 57.6 kg/mol. PHPA and POEGA were each precipitated three times after polymerization, in a 1:1 mixture of hexanes/ethyl acetate and pure hexanes, respectively. The maleimide-protecting group was removed by a retro Diels-Alder reaction by heating the polymers to 120 °C for 2 hours under vacuum. To eliminate all detectable coupling between maleimide groups during deprotection, approximately 10 wt.% of butylated hydroxytoluene and hydroquinone were each added to the polymers prior to deprotection. Added inhibitors were removed by repeating the same precipitation steps three times followed by a thermal precipitation in water.

GPC characterization, ^{1}H-NMR analysis, and cloud point measurements of PHPA and POEGA are described in detail in Section 2.2. GPC traces of the polymers used in this study are shown in Figure 3-1, and their molar masses and dispersities (Đ) are listed in Table 3-1. Representative ^{1}H-NMR spectra of homopolymers are shown in Figure 3-2 and Figure 3-3 for PHPA 27K and POEGA 26K, respectively.

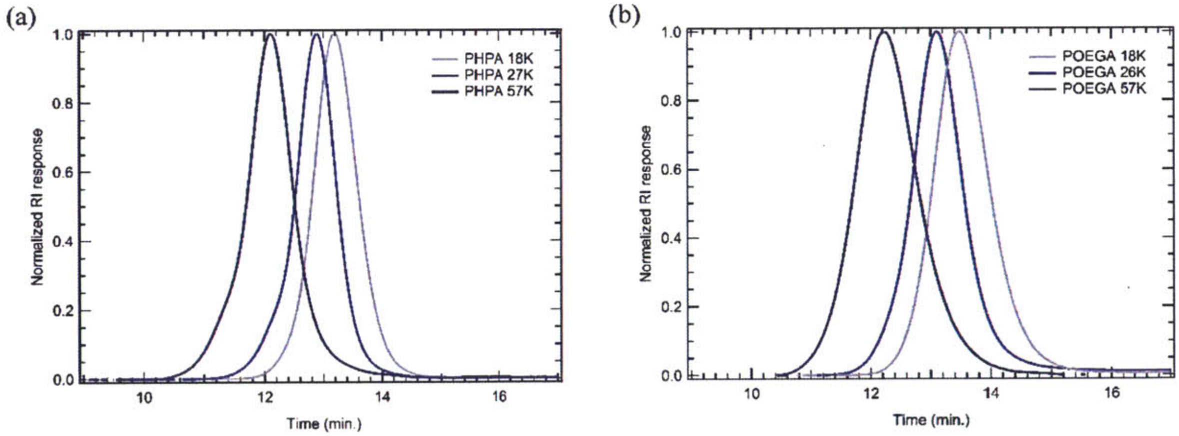

Figure 3-1. GPC traces of (a) PHPA and (b) POEGA homopolymers with three different molar masses used in this study.

Table 3-1. Molecular Properties of Protein-Polymer Conjugates.

Abbreviation	Copolymer	Polymer M_n (kg/mol)	Dispersity (Đ)	Bioconjugate M_n (kg/mol)	$\phi_{polymer}$ [a]	Composition [b]	Cloud point (°C) [c]
mChPH18	mCherry-PHPA 18K	17.7	1.20	45.8	0.42	-	11.6
mChPH27	mCherry-PHPA 27K	27.2	1.22	55.4	0.53	-	11.4
mChPH57	mCherry-PHPA 57K	57.0	1.23	85.1	0.70	-	11.4
mChPOE18	mCherry-POEGA 18K	18.4	1.18	46.5	0.46	54/46	18.7
mChPOE26	mCherry-POEGA 26K	26.1	1.19	54.2	0.54	53/47	21.7
mChPOE57	mCherry-POEGA 57K	57.6	1.25	85.7	0.72	49/51	23.0

[a] Density of PHPA 1.16,[30] POEGA 1.05,[31] and mCherryS131C 1.35g/cm[3,32] were used to calculate volume fraction of polymers in bioconjugates.

[b] The composition shown is the molar ratio of MEA to MEEA monomer in POEGA.

[c] The cloud point was measured for homopolymers in water.

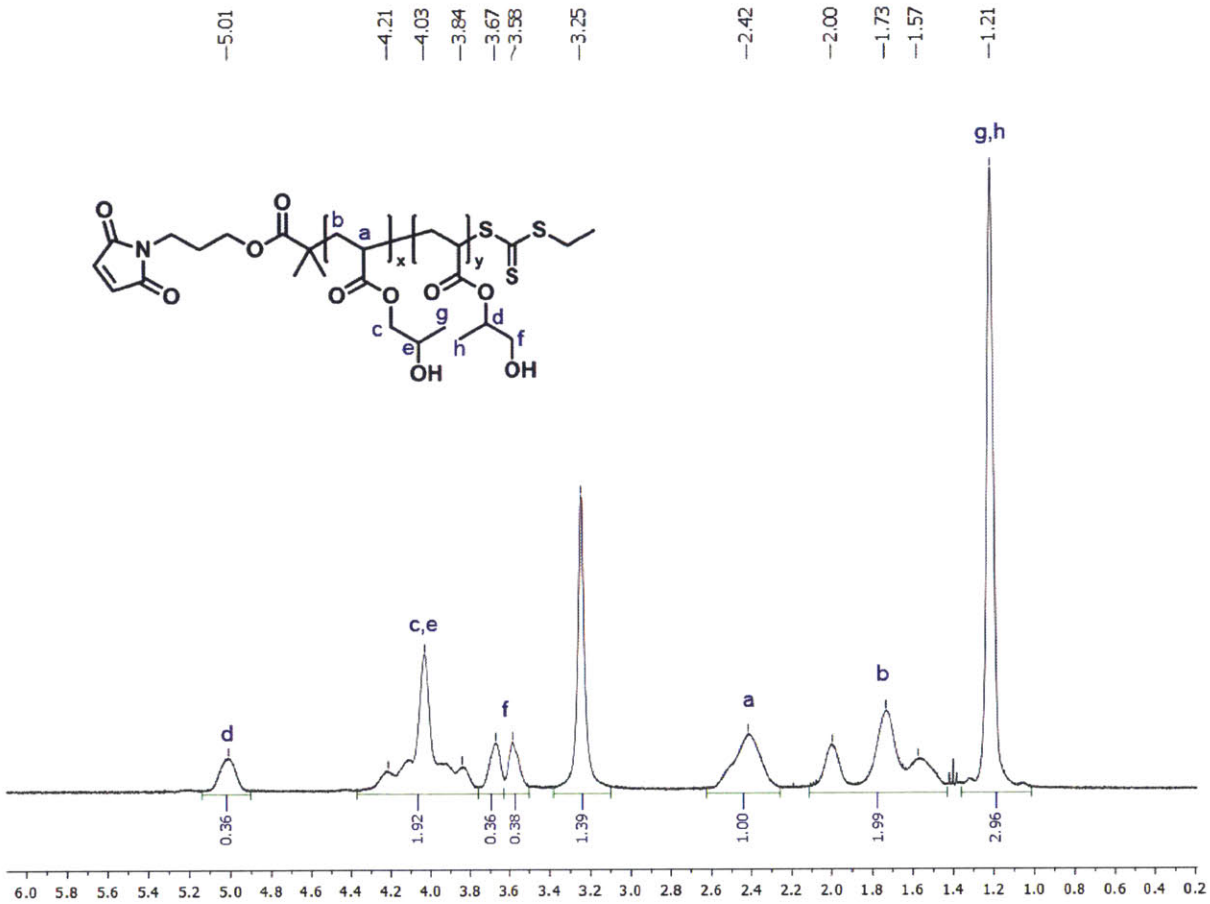

Figure 3-2. ^{1}H-NMR spectrum of deprotected PHPA with M_n 27,220 g/mol in $CDCl_3$ solution. The NMR spectrum shows that the polymer consists of 64% of the major isomer (x) and 36% of the minor isomer (y). The fraction of the minor isomer was determined from the equation $\frac{y}{x+y} = \frac{H_d}{H_a} = \frac{0.36}{1}$ where H_d/H_a is the ratio between the number of d-type protons and the number of a-type protons.

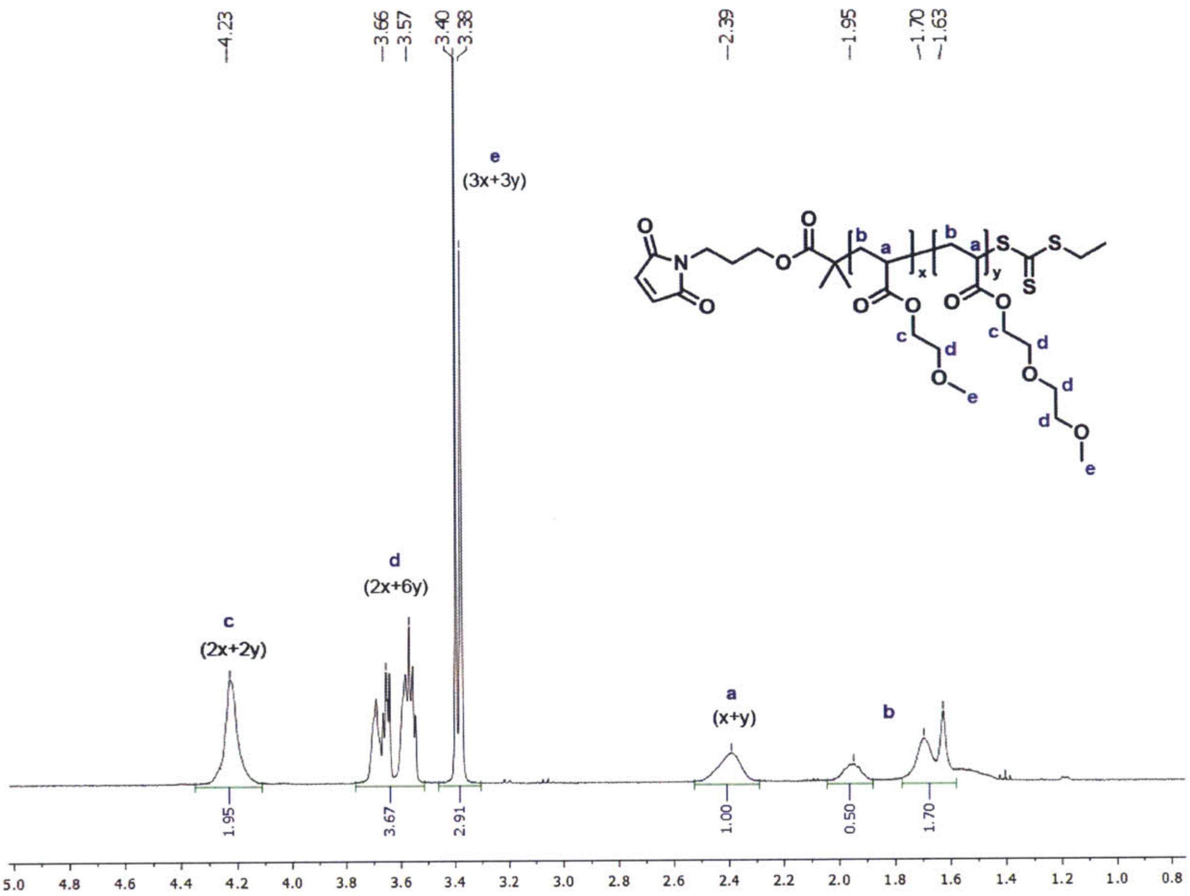

Figure 3-3. ^{1}H-NMR spectrum of deprotected POEGA with M_n 26,080 g/mol in $CDCl_3$ solution. The molar monomer ratio of MEA and MEEA (x:y) incorporated into the polymer is determined to be 53/47 based on the ratio of d-type protons and e-type protons shown in the spectrum.

Protein expression and bioconjugation. mCherryS131C protein expression, purification, and thiol-maleimide coupling reactions were carried as previously described.[17] Briefly, a 6-fold molar excess of either polymer was mixed with mCherryS131C in 20 mM Tris buffer at pH 8.0 after pre-incubation of the protein with 10-fold molar excess of 3,3′,3′′-phosphanetriyltripropanoic acid hydrochloride (TCEP·HCl) for 1 hour to reduce disulfide bonds. Reactions were carried out for 2 days at 4 °C, followed by precipitation in 1M ammonium sulphate at pH 8.0 three times to remove unreacted protein. The resuspended mixture was purified by nickel affinity chromatography to remove unreacted polymers and dialyzed into MilliQ water. Native gels showed the purity of final products was greater than 98 mol% (Figure 3-4). Circular dichroism (CD) analysis and UV-vis spectroscopy demonstrate that the secondary structure and activity of the protein are preserved after bioconjugation (Figure 3-5 a-d). The molar masses of the bioconjugates and polymer volume fractions are listed in Table 3-1 for all six conjugate materials.

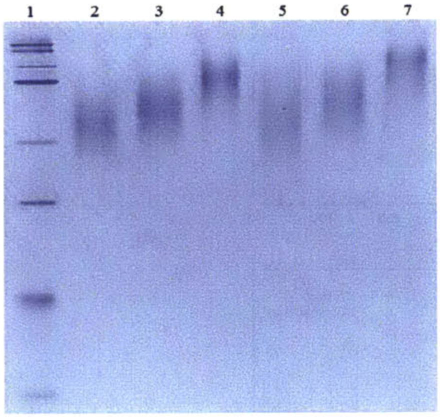

Figure 3-4. Native protein gel of mCherry-*b*-PHPA and mCherry-*b*-POEGA bioconjugates. Lanes 1-7 represent ladder, mCherry-PHPA 18K, mCherry-PHPA 27K, mCherry-PHPA 57K, mCherry-POEGA 18K, mCherry-POEGA 26K, and mCherry-POEGA 57K, respectively. The molar purities determined by lane and bands analysis tool in Image Lab software were greater than 98%.

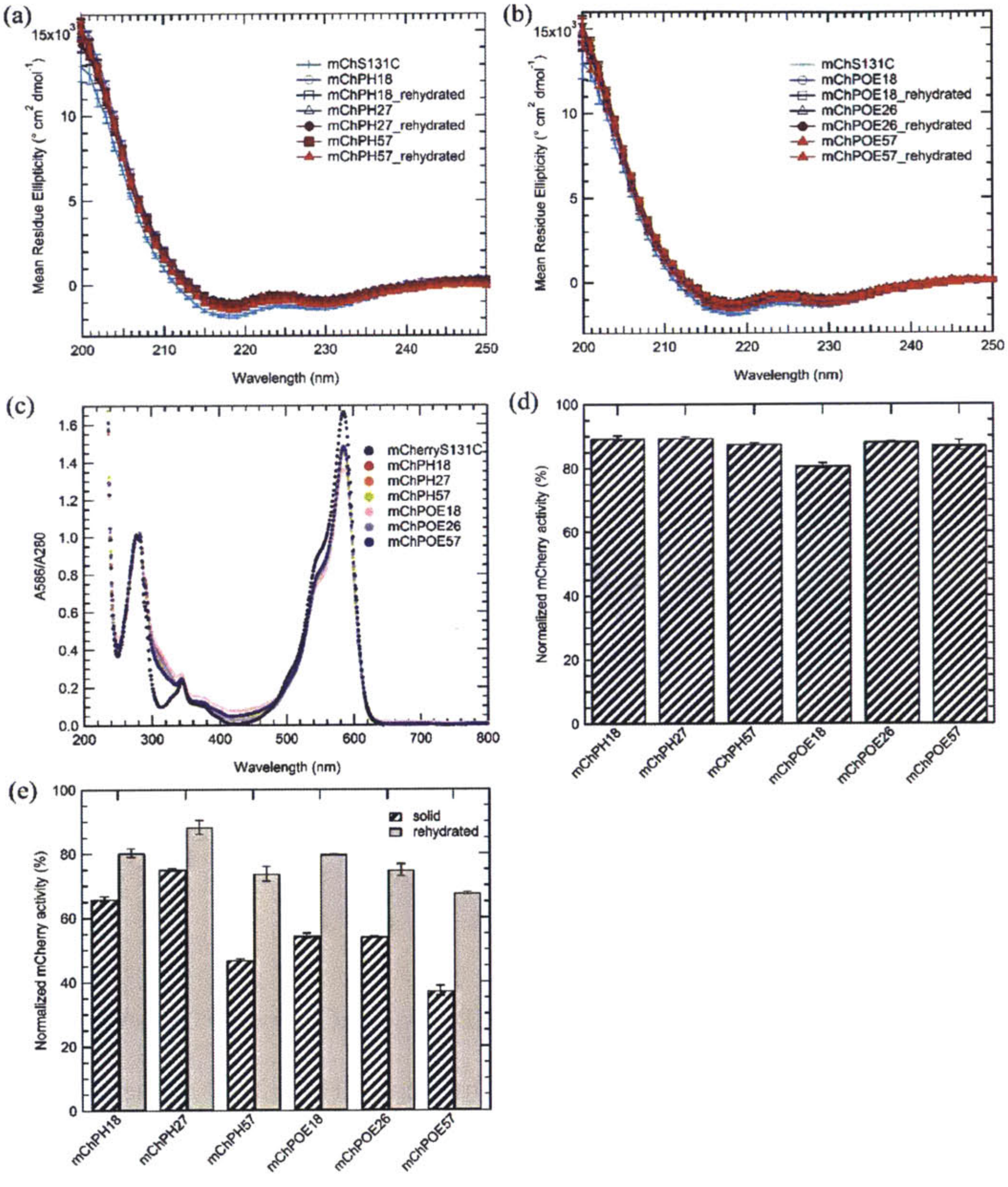

Figure 3-5. Circular dichroism (CD) spectrum of mCherry and of (a) mCherry-*b*-PHPA and (b) mCherry-*b*-POEGA, after conjugation and after rehydration of solid-state materials. CD spectrum of mCherry was measured in 20 mM Tris-Cl buffer (pH=8.0) while those of the bioconjugates were measured in water. No significant change in secondary structure is observed after conjugation and self-assembly. (c) UV-Vis spectra of mCherry and of mCherry-*b*-PHPA and mCherry-*b*-POEGA normalized to the absorbance at 280 nm. Retention of activity upon

conjugation was calculated by comparing the ratio of the chromophore absorption peak of mCherry at 586 nm to the absorption peak at 280 nm (A586/A280) to the A586/A280 ratio of fresh mCherry. (d) Results show that mCherry-*b*-PHPA retains approximately 90% of the initial protein activity after bioconjugation and purification for all polymer coil fractions studied, while mCherry-*b*-POEGA retains approximately 80-90%. (e) After solid-state casting and self-assembly and rehydration, the bioconjugates maintain approximately 70-90% of the activity of the bioconjugates after purification.

Sample processing Purified bioconjugate solutions were concentrated to approximately 100 mg/mL using centrifugal filters with a molecular weight cut-off of 10 kDa. The solutions were cast in 20 μL aliquots on Teflon sheets and dried under dynamic vacuum with a ramp rate of 50 Torr per hour until a final pressure of 10 Torr, followed by holding at this pressure overnight. The collected pellets were re-dissolved in water to prepare the desired concentrations of bioconjugate solutions. CD analysis and UV-vis measurements demonstrate that the protein secondary structure and greater than 70-90% of the activity are preserved after drying to induce self-assembly and subsequent rehydration (Figure 3-5 a,c, and e).

Characterization Small-angle X-ray scattering (SAXS), depolarized light scattering (DPLS), and turbidimetry were carried out as previously described.[17] SAXS measurements were performed at NSLS beamline X27C at Brookhaven National Laboratory. The samples were studied at temperatures from 5°C to 35°C in 5°C increments with a 10 minute equilibration time at each temperature. Concentration was varied between 20 and 80 wt.% in 10 wt.% increments, with selected additional measurements for more precise determination of order-disorder transition concentrations. Small-angle neutron scattering (SANS) of mChPH27 and mChPOE26 at 30 wt.% concentration was used to analyse the hydration levels of the mCherry and polymer domains at 10 °C using contrast variation as reported previously for mCherry-*b*-PNIPAM.[17] Contrast variation of mChPH27 was performed in D_2O%/H_2O% solvent compositions of 10/90, 20/80, 30/70, 50/50, and 70/30, and for mChPOE26, the same solvent compositions were used excluding 10/90 D_2O%/H_2O%. Samples were loaded into a 1 mm thick washer and sealed between two quartz discs. Data acquisition was performed at Oak Ridge National Laboratory at the EQ-SANS Diffractometer. Samples were equilibrated at 10 °C for 20 minutes prior to data collection. SANS data were collected and corrected for empty cell and dark field scattering. Reversibility of heating and cooling curves of DPLS and turbidimetry were confirmed for every sample. Polarized optical microscopy (POM) with an Axioskop2 MAT (Zeiss) was used to image 80 wt.% samples.

3.4 Results and Discussion

In comparison to previously reported mCherry-*b*-PNIPAM bioconjugates, mCherry-*b*-PHPA and mCherry-*b*-POEGA diblock copolymers show phase transitions at significantly different concentrations and temperatures as well as the appearance of previously unobserved nanostructures. Phase diagrams are constructed for both polymers at three different polymer volume fractions (Figure 3-6) by using a complementary set of characterization techniques including SAXS (Figure 3-10 and Figure 3-11), DPLS, and turbidimetry (Table 3-2).

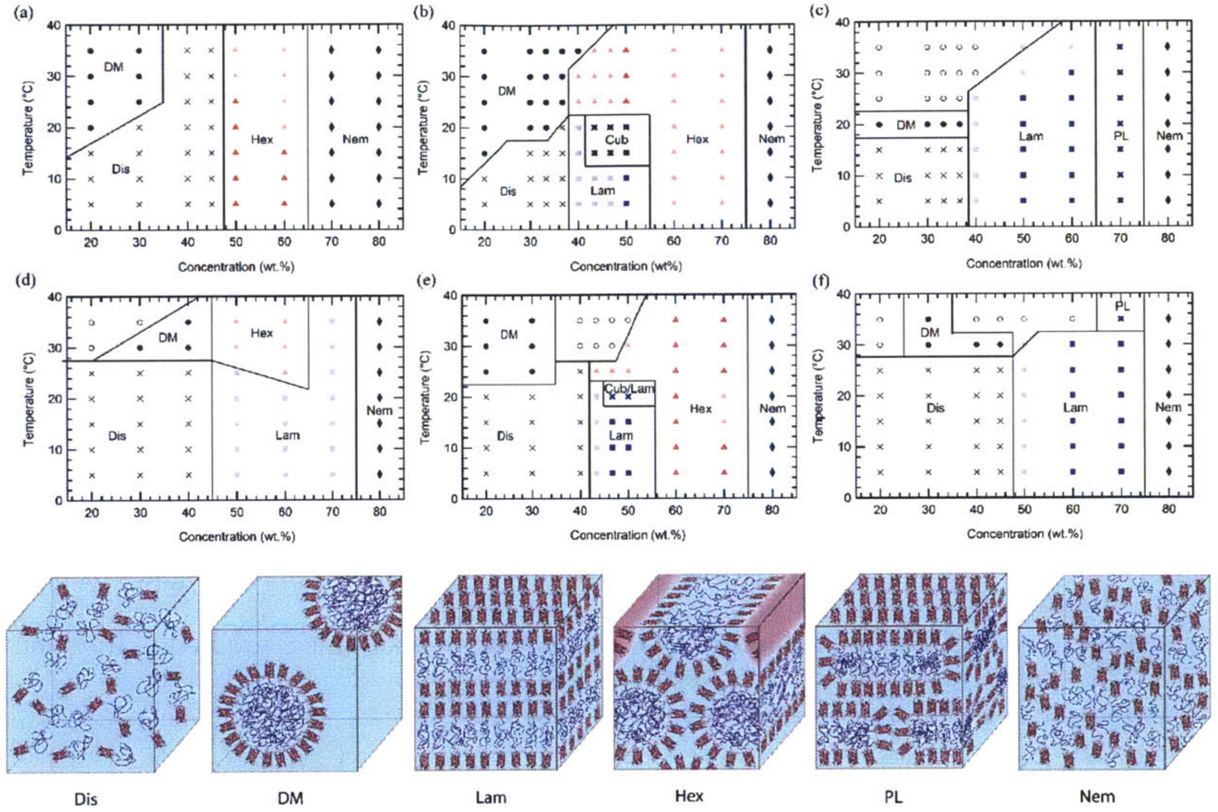

Figure 3-6. Phase diagrams of mCherry-*b*-PHPA in aqueous solution are shown at the top row at polymer fraction (a) 0.42, (b) 0.53, and (c) 0.70, and mCherry-*b*-POEGA at the bottom row at polymer fraction (d) 0.46, (e) 0.54, and (f) 0.72 as a function of concentration and temperature. Dis: disordered phase, DM: disordered micellar phase, Hex: hexagonally packed cylindrical phase, Lam: lamellar phase, Cub: bicontinuous cubic phase, PL: perforated lamellar phase, Nem: nematic phase, and Cub/Lam: cubic and lamellar phase coexistence. Light colored symbols represent non-birefringent lamellae or hexagonally packed cylinders, while dark symbols represent birefringent phases. Closed symbols denote a homogeneous phase, and open symbols denotes macrophase separated phases.

Regardless of the polymer coil fraction or polymer chemistry, phase diagrams have several common features. At low temperatures below the thermoresponsive transition temperature of the bioconjugates, water is a nonselective solvent for both the protein and polymer. In this regime, low concentration solutions of mCherry-*b*-PHPA and mCherry-*b*-POEGA form disordered phases. Both bioconjugates microphase separate with increasing concentration, exhibiting ordered regions in the general range of 40 to 70 wt.%. They form hexagonally packed cylinders or lamellae depending upon coil fraction and type of polymer, and lyotropic order-order transitions between the two phases can be observed within this concentration window. At very high concentrations, both bioconjugates display a re-entrant order-disorder transition (ODT) behavior, transitioning gradually from an ordered phase to a disordered nematic phase at 80 wt.%.

Above the thermoresponsive temperature where water is a selective solvent for mCherry, low concentration solutions form a disordered micellar phase (DM) due to the thermoresponsive behavior of the polymers. A region of macrophase separation often accompanies this thermoresponsive transition, indicating coexistence between a high conjugate concentration and low conjugate concentration phase. It is likely that the phases formed show kinetic effects on structure formation due to the high thermodynamic barrier for polymer diffusion across water-rich nanodomains above the thermoresponsive transition temperature, as previously observed.[16] At concentrations between 40 and 70 wt.%, most bioconjugates maintain their nanostructures with increasing temperature but display a decrease in degree of ordering, evidenced by broader SAXS peaks and decreased birefringence. Symmetric bioconjugates show multiple thermotropic order-order transitions within this microphase separated region and display the most complex phase behaviors. High concentration phase behavior is strongly affected by solvent selectivity towards the polymer at high temperature. Heating reduces the degree of hydration of the polymer coil, leading to an effective reduction in polymer coil fraction.

Lyotropic order-disorder transitions in a nonselective solvent

Although the overall shapes of the phase diagrams are similar for all polymers, the lyotropic order-disorder transition of the bioconjugates is strongly affected by the type of polymer and the polymer coil fraction. The C_{ODT} is defined as the lowest concentration at which ordering is observed at temperatures below the block copolymer thermoresponsive temperature, where both blocks are well hydrated. Representative SAXS curves between 30 and 60 wt.% at 5°C show lyotropic disorder to order transitions with increasing concentration (Figure 3-10). mChPH18 starts to form hexagonally packed cylinders at 50 wt.% (Figure 3-10a), while mChPH27 and mChPH57 form lamellar phases at 40 wt.% (Figure 3-10 b, c). mChPOE18 forms a poorly ordered lamellar phase at 50 wt.% (Figure 3-10d), while mChPOE26 forms a lamellar phase at 43 wt.% (Figure 3-10e, curve not shown), and mChPOE57 also forms lamellae at 50 wt.% (Figure 3-10f).

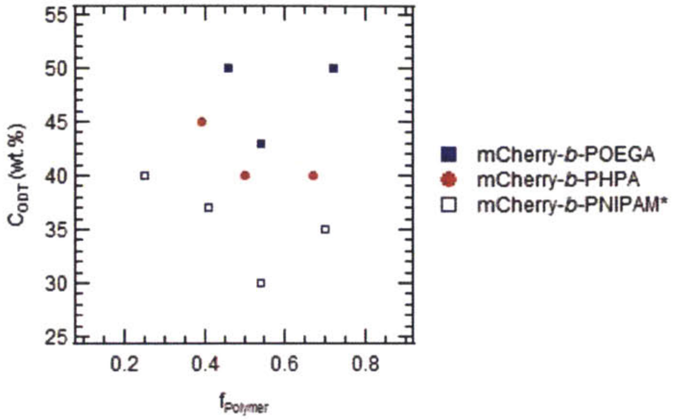

Figure 3-7. Order-disorder transition concentration (C_{ODT}) values for the three types of bioconjugates versus polymer volume fraction. *mCherry-*b*-PNIPAM data are adapted from Figure 5 of Ref 17.

A plot of C_{ODT} for the three different polymer block types (mCherry conjugated to PNIPAM, PHPA, and POEGA) (Figure 3-7) shows a trend in C_{ODT} as a function of polymer block chemistry. The C_{ODT} of mCherry-*b*-PNIPAM is 5-10 wt.% lower than that of mCherry-*b*-PHPA, and the C_{ODT} of mCherry-*b*-PHPA is 5-10 wt.% lower than that of mCherry-*b*-POEGA at all three coil fractions studied. This suggests that changing polymer block chemistry, which changes protein-polymer interactions, has a large effect on this transition. The results support the conclusion that PNIPAM is the most repulsive to the protein while POEGA is the least repulsive. The trend in C_{ODT} does not follow the trend in thermoresponsive transition temperature (T_t) for the three polymers. Despite PNIPAM having the highest T_t of the three polymers, mCherry-*b*-PNIPAM is observed to have the lowest C_{ODT}, while mCherry-*b*-POEGA, which has the intermediate T_t value, has the highest C_{ODT}. It is observed that mCherry conjugates with polymers capable of both accepting and donating hydrogen bonds, PNIPAM and PHPA, have the lowest C_{ODT}s, although a more quantitative understanding of the interactions in this system is required to draw firm conclusions regarding the origin of this effect.

The C_{ODT} is minimized at near-symmetric coil fraction for which protein-polymer interactions are maximized (Figure 3-7). While mCherry-*b*-POEGA and mCherry-*b*-PNIPAM show clear minima as a function of coil fraction, the minimum for mCherry-*b*-PHPA likely lies around 0.6, as C_{ODT} of the conjugates with coil fractions of 0.50 and 0.67 are the same to within the resolution of our measurement. In all cases, the small number of coil fractions sampled does not allow precise resolution of the coil fraction at which C_{ODT} is minimized. This non-monotonic trend in C_{ODT} with coil fraction further supports the hypothesis that solvent-mediated repulsive interactions between protein and polymer blocks are responsible for microphase separation near order-disorder transition concentrations.[17]

Re-Entrant Order-Disorder Transition

Surprisingly, both mCherry-*b*-PHPA and mCherry-*b*-POEGA become disordered upon increasing concentration for all coil fractions studied, but in all cases remain in an anisotropic phase, as evidenced by strong optical birefringence. At concentrations between 60 and 80 wt.%, the primary SAXS peaks of both mCherry-*b*-PHPA and mCherry-*b*-POEGA bioconjugates significantly broaden as concentration increases (Figure 3-6 a and d). This loss of ordering is consistent with our recent observation of re-entrant transitions in mCherry-*b*-PNIPAM.[25] However, birefringence of mCherry-*b*-PHPA and mCherry-*b*-POEGA is maintained or becomes stronger as the concentration nears 80 wt.% (Figure 3-68b, e), which, in combination with the disordered SAXS pattern, is characteristic of a nematic liquid crystalline phase. Polarized optical microscopy images shown in Figure 3-8c and 3-8f show birefringence of 80 wt.% solution samples of mChPH18 and mChPOE18. Because these materials are prepared by adding solvent to a solid-state material that is kinetically trapped in a more ordered state (Figure 3-9), the loss of microphase separation and formation of a nematic phase appears to be an equilibrium effect.

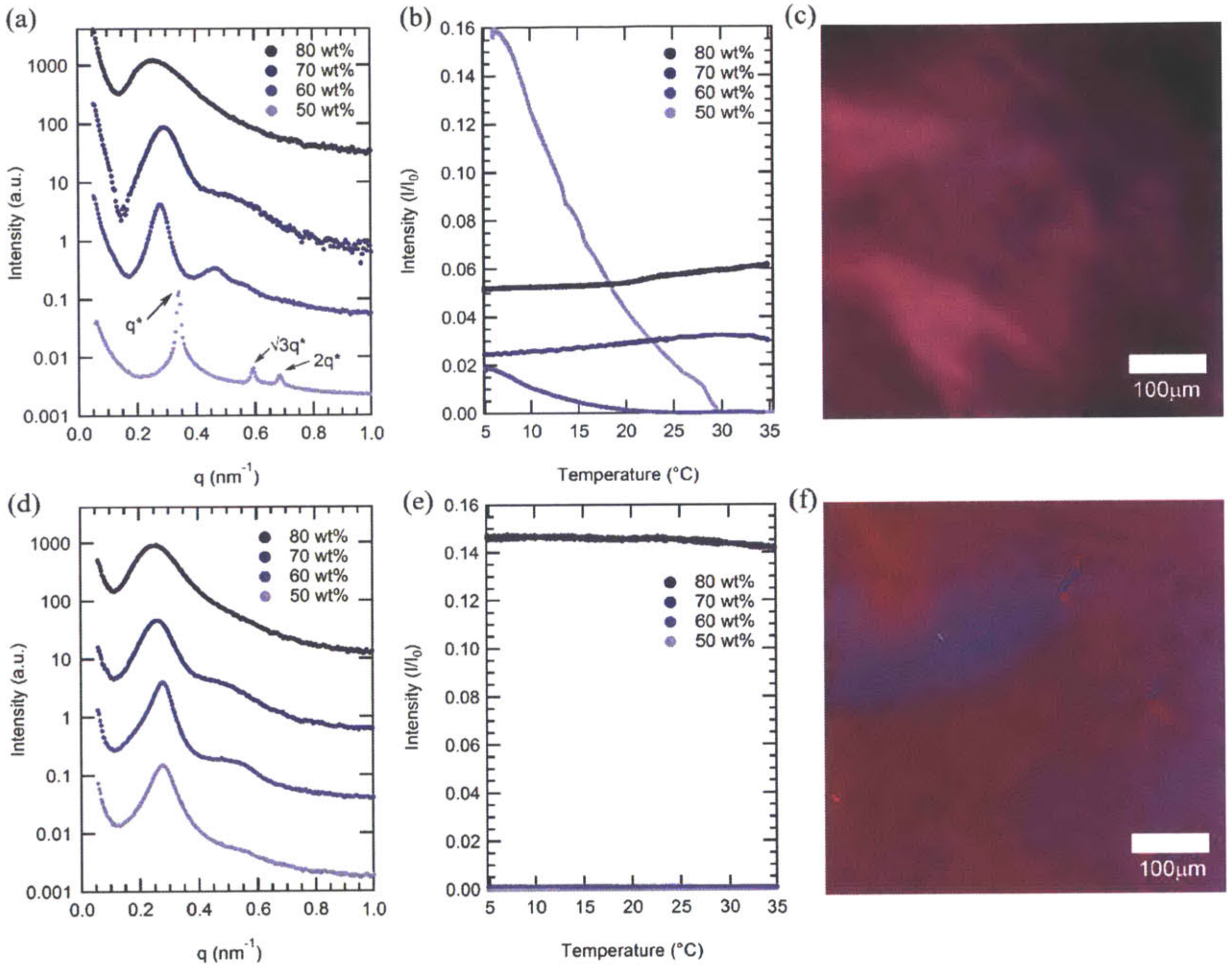

Figure 3-8. Top row: SAXS curves (a), DPLS curves (b), and a polarized optical microscopy image (c) of mChPH18 sample. Bottom row: SAXS curves (d), DPLS curves (e), and a polarized optical microscopy image (f) of mChPOE18. For mChPH18, a birefringent hexagonally packed cylindrical phase (Hex) at 50 wt% gradually loses ordering as concentration increases to 80 wt% by SAXS, while birefringence begins increasing at 70 wt%. The nonbirefringent lamellar phase of mChPOE18 between 50 and 70 wt% becomes gradually disordered as concentration increases to 80 wt% while becoming birefringent. Polarized light microscopy images are shown for 80 wt% samples.

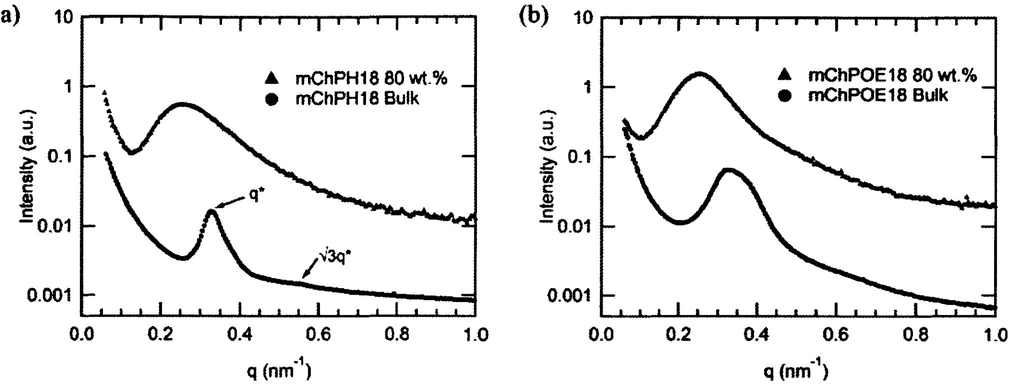

Figure 3-9. SAXS curves of solid state samples in comparison to 80 wt.% solution samples for (a) mChPH18 and (b) mChPOE18. Bulk samples were casted at 4°C and form kinetically trapped structures without annealing, while 80 wt.% bioconjugate solutions show re-entrant ODT behaviors. All samples were measured at 25°C.

The observed disordering at high concentration is unexpected in block copolymers, where the dilution approximation[33] predicts that repulsion between two blocks increases as concentration increases in a nonselective solvent. Re-entrant ODT behavior has been previously observed in polystyrene-*b*-polyisoprene (PS-PI) diblock copolymers in decane which is a selective solvent for polyisoprene.[29] A loss of micellar nanostructure and transition to a disordered phase as solutions become highly concentrated is hypothesized to result from a loss of repulsive pair interaction potential between micelles. A triblock copolymer of poly(ethylene oxide)-*b*-poly(propylene oxide)-*b*-poly(ethylene oxide) (PPO-PEO-PPO) in water, selective for PEO, does not order in bulk melt state while it microphase separates in the presence of the selective solvent.[34,35] The observation of re-entrant order-disorder transitions in mCherry-polymer system in water which is only slightly selective for polymer as shown in the later section suggests that interactions between protein and polymer become net attractive with increasing concentration. The fact that microphase separated order is lost with increasing concentration regardless of the polymer chemistry suggests that this may be a universal property of mCherry-polymer conjugate materials.

The presence of optical anisotropy in the absence of microphase separation suggests that at high concentration the mCherry-*b*-PHPA and mCherry-*b*-POEGA conjugates form nematic phases. Such phases are commonly observed in rod-coil, main-chain, and side-chain liquid crystalline block copolymers,[36] including such polymers where the liquid crystalline motif is composed of a simple polypeptide secondary structure (e.g., α-helix).[37] Formation of a nematic phase by biological molecules was recognized as early as 1936 for rod-shaped tobacco mosaic viruses.[38] Many other rod-shaped biological molecules, including Pf1 bacteriophage[39] and amyloid protein fibers,[40,41] were also shown to form nematic phases. Phase transitions to a nematic phase above a critical concentration are entropically driven due to excluded volume effects.[42] However, globular proteins themselves rarely exhibit liquid crystalline phases.[43,44] It is surprising that mCherry conjugates form liquid crystalline phases given the protein's low aspect ratio. From its crystal structure (PDB 2H5Q), mCherry has a β-barrel structure with dimensions of approximately 4.2 nm in height and 2.5 nm in diameter, giving an aspect ratio of 1.7, well below the de Gennes criteria of 4.[45] Although mCherry-polymer conjugates have previously been shown to be aspherical in dilute solution,[16] the highly overlapped nature of polymer chains in concentrated solution is known to result in significantly different chain configurations that prevent comparison between chain configurations in dilute solution and in the nematic phase. It is possible that anisotropic electrostatic interactions between proteins[46] in addition to excluded volume effects contribute to the formation of anisotropic phases. In addition, conjugation to the polymer can result in a more anisotropic macromolecular structure resembling classical small molecule mesogens such as 5CB that are capable of forming nematic phases.

Birefringence is strongest at $\phi = 0.4$ for both mCherry-*b*-PHPA and mCherry-*b*-POEGA, where the volume fraction of protein is largest. This supports the notion that formation of the nematic phase is governed by interactions between mCherry blocks. mChPOE18 has especially high birefringence compared to mChPOE26 and mChPOE57 as well as other bioconjugates. The fact that mChPOE18 has the strongest optical anisotropy correlates with its relatively small region of microphase separated structures. When protein and polymer blocks are most miscible, the mCherry liquid crystalline interactions can have the largest effect on phase behaviors.

Low concentration in selective solvents

At high temperature where water is a selective solvent for mCherry, the primary SAXS peak of low concentration solutions of all bioconjugates shifts to a lower q value compared to that at low temperature. The shifting primary peak at high temperature is correlated with the formation of larger structures, presumably micelles formed due to the thermoresponsive desolvation of the polymer blocks. The micellar transition occurs at consistently higher temperatures in mCherry-*b*-POEGA than in mCherry-*b*-PHPA, which is consistent with the observed higher cloud points of POEGA homopolymers. However, for both types of conjugate, the transition from disordered to micellar phases occurs at a significantly higher temperature than the homopolymer cloud point temperature, indicating the enhanced solubility imparted by the large protein block and the effect of increased concentration.

Table 3-2. Thermal transition temperatures (°C) observed via DPLS and turbidimetry.

	T_{DPLS}^{a} (°C)						T_t (°C)					
	mCherry-*b*-PHPA			mCherry-*b*-POEGA			mCherry-*b*-PHPA			mCherry-*b*-POEGA		
$\phi_{polymer}$	0.4	0.5	0.7	0.4	0.5	0.7	0.4	0.5	0.7	0.4	0.5	0.7
20 wt.%	○	○	○	○	○	○	-	-	20.5	28.1	-	27.0
30 wt.%	○	○	○	○	○	○	-	-	21.5	31.7	-	-
40 wt.%	○	○	○	○	○	○	-	-	25.8	-	25.2	32.0
50 wt.%	29.3	●	29.1	○	19.8	○	-	-	-	-	31.1	29.4
60 wt.%	20.1	○	34.4	○	●	31.8	-	-	-	-	-	34.8
70 wt.%	●	○	●	○	●	●	-	-	-	-	-	-
80 wt.%	●	●	●	●	●	●	-	-	-	-	-	-

○: sample displayed no birefringence
●: sample remained birefringent at all temperatures
[a]: temperature at which bioconjugates lost birefringence
-: sample did not macrophase separate

The stability of a homogeneous micellar phase leading to macrophase separation depends on the polymer block type and coil fraction (transition temperatures are listed in Table 3-2). mCherry-*b*-PHPA and mCherry-*b*-POEGA both show a narrower concentration and temperature range of macrophase separation than mCherry-*b*-PNIPAM conjugates, despite PHPA and POEGA homopolymers having lower cloud point temperatures than PNIPAM. mChPH18 and mChPH27 form macroscopically homogeneous phases throughout all concentrations and temperatures measured, and a macrophase separated region is only observed in mChPH57. While equilibrium thermodynamics suggests that the two phases should have compositions equal to those on the boundaries of the two phase region, the structure observed by SAXS does not show signs of lamellar ordering, suggesting that the material may be kinetically trapped in a disordered micellar phase as previously observed for other conjugates.[16] The mCherry-*b*-POEGA bioconjugate solutions show two types of macrophase separation behavior. At low concentration, two phases of water-rich and micelle-rich solutions are formed, as shown in mChPOE18 and mChPOE57 (Figure 3-6 d, f). At intermediate concentration, macrophase separated regions flanked by a homogeneous micellar phase in mChPOE26 or a hexagonally packed cylindrical phase in mChPOE57 suggest that a true equilibrium state is a coexistence of two phases between the neighboring homogeneous phases. mCherry-*b*-PNIPAM solutions show much larger regions of macrophase separation, which is correlated with the low stability of mCherry-*b*-PNIPAM micelles in dilute solution compared to mCherry-*b*-PHPA and mCherry-*b*-POEGA micelles.[17]

Macrophase separation temperatures (T_t) summarized in Table 3-2 are lowest in mCherry-*b*-PHPA and highest in mCherry-*b*-PNIPAM,[17] which is also consistent with the trend in cloud points of homopolymers. The macrophase separation temperature increases with increasing concentration, similar to the trend observed in mCherry-*b*-PNIPAM. However, unlike mCherry-*b*-PNIPAM, thermal transitions are undetectable by differential scanning calorimetry.

Structure of the microphase separated region

For all coil fractions, ordered phases are observed from apprximately 40 to 70 wt.%, although the type of nanostructure and quality of order are affected by coil fraction, temperature, and concentration. Representative SAXS curves at low and high temperature are shown in Figure 3-10 and Figure 3-11, respectively. Complementary DPLS results are summarized in Table 3-2.

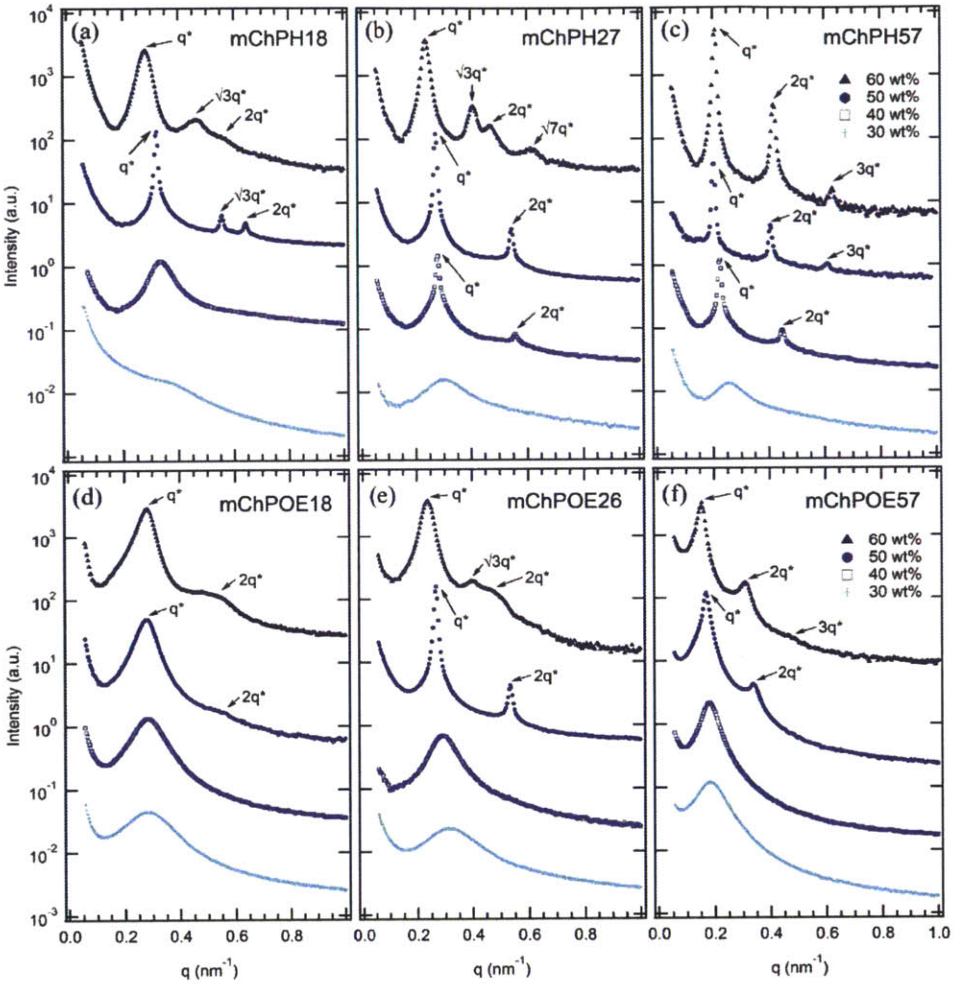

Figure 3-10. SAXS curves of mCherry-*b*-PHPA (a-c) and mCherry-*b*-POEGA (d-f) solutions from 30 to 60 wt.% for three polymer coil fractions at 5°C where both blocks are well solvated. Lyotropic disorder to order transitions occur between 30 and 50 wt.% for all bioconjugates ((a) 50 wt.% (b) 40 wt.% (c) 40 wt.% (d) 50 wt.% (e) 43 wt.% (not shown) (f) 50 wt.%). Bioconjugates with $\phi = 0.5$ (mChPH27 and mChPOE26) further undergo lyotropic order-order transition from lamellae to hexagonally packed cylinders as concentration increases from 50 to 60 wt.% (b,e). Curves are vertically offset for clarity.

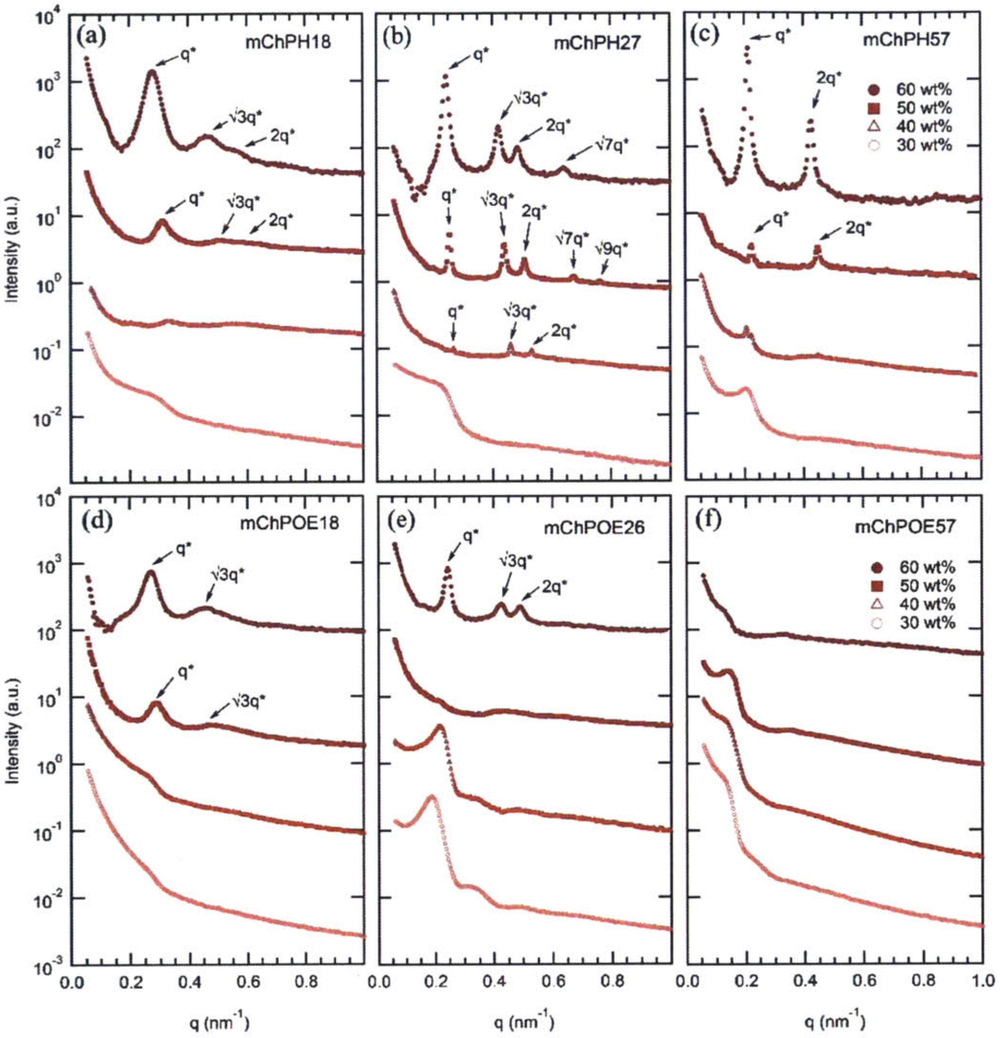

Figure 3-11. SAXS curves of mCherry-*b*-PHPA and mCherry-*b*-POEGA solutions at 30°C and 35°C, respectively. Curves are vertically offset for clarity.

At a coil fraction of 0.4, mCherry-*b*-PHPA forms well-ordered hexagonally packed cylinders, whereas mCherry-*b*-POEGA shows only weakly ordered lamellar regions (Figure 3-6 a and d). At low temperature where both blocks are well solvated, mChPH18 starts to order at 50 wt.% into a hexagonal phase, which is indicated by a sharp primary peak with clear higher order reflections at $\sqrt{3}q^*$ and $\sqrt{4}q^*$ (Figure 3-10a) and strong birefringence. At high temperature, broadening of the SAXS peaks is observed and birefringence is lost, suggesting a partial loss of order in the hexagonal phase. In contrast, mChPOE18 has very weak ordering throughout all the concentrations and temperatures explored, demonstrating only a a weak secondary reflection by SAXS at $2q^*$ that can be assigned to a lamellar phase. No birefringence is observed for mChPOE18 samples except for a nematic phase at 80 wt.%, consistent with poor ordering observed by SAXS. Above the thermoresponsive transition temperature between 20 and 25°C in the concentration range of 50-60 wt.%, mChPOE18 solutions form weakly ordered hexagonal phases at 50 and 60 wt.% (Figure 3-11d).

The solution phase behavior of bioconjugates with symmetric coil fractions shows the most complex lyotropic and thermotropic order-order transitions, as well as phases that are not observed in previously studied materials (Figure 3-10 b, e). At low temperatures, mChPH27 and mChPOE26 first form nonbirefringent lamellar phases upon ordering, with birefringence appearing upon increasing order with increasing concentration.[47,48] Birefringent lamellae exist in a narrow concentration range up to 50 wt.%, above which the solution forms a hexagonally packed cylindrical phase with three or four reflections at q^*, $\sqrt{3}q^*$, $\sqrt{4}q^*$, and $\sqrt{7}q^*$ observed in SAXS. While for mChPH27 this phase is nonbirefringent at low temperatures, in mChPOE26 there is sufficient order to produce a birefringent cylinder phase. Above the thermoresponsive transition temperature, both conjugates form cylinder phases across the entire ordered region, with no birefringence observed at lower concentrations. This thermotropic order-order transition results from an effectively reduced polymer volume fraction in the bioconjugate above the thermoresponsive temperature. In the case of mChPH27, this phase becomes birefringent over a narrow concentration range then loses birefringence as concentration is further increased, suggesting maximal order at an intermediate concentration. However, in mChPOE26, birefringence appears at 60 wt.% and continues to the end of the ordered region.

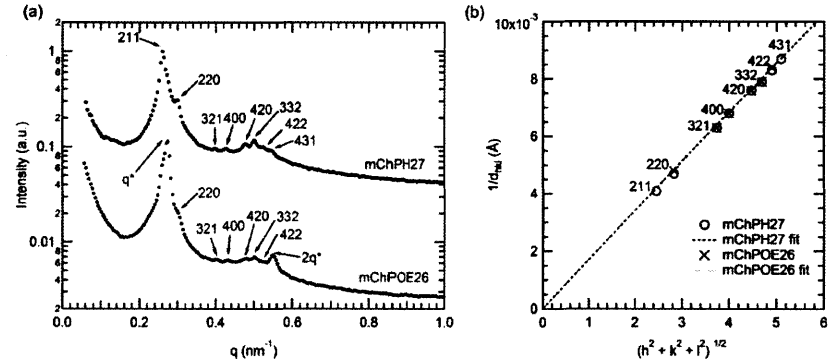

Figure 3-12. (a) SAXS curve of mChPH27 50 wt% solution at 15°C (top) and of mChPOE26 50 wt.% at 20°C (bottom). (b) A plot of *m* vs. $1/d_{hkl}$ based on the reflections observed in the samples showing the validity of the space group assignment. The fitted lines are forced to intercept the origin. The lattice parameter of 58.4 nm is obtained for mChPH27 from the slope value of 0.00171 with R^2=0.9996, and lattice parameter is 58.3 nm for mChPOE26 from the slope 0.00172 with R^2=0.9994.

In a narrow region between 15 and 20°C and 43 and 50 wt.%, mChPH27 forms an intermediate phase with cubic symmetry (Cub) between a lamellar phase at low temperature and a hexagonally packed cyindrical phase at high temperature. Bragg reflections corresponding to $\sqrt{6}$, $\sqrt{8}$, $\sqrt{14}$, $\sqrt{16}$, $\sqrt{20}$, $\sqrt{21}$, $\sqrt{24}$, and $\sqrt{26}q^*$ are indexed (Figure 3-12a, top curve), corresponding to the first 8 allowed reflections for an $Ia\bar{3}d$ phase.[49,50] A plot of reciprocal d spacings versus $m = (h^2 + k^2 + l^2)^{1/2}$ (where h,k, and l are the Miller indices) (Figure 3-12b) shows good agreement between the observed reflections and a crystallographic structure with $Ia\bar{3}d$ symmetry. SAXS analysis alone is generally not sufficient for phase assignment, however, considering the fact that $Ia\bar{3}d$ corresponds to the bicontinuous cubic phase in many different types of block copolymers[49,51,52] and that this phase is located between the hexagonally packed cylindrical phase and lamellar phase, it is likely that this is the first observed gyroid phase made of globular protein-polymer block copolymer.

mChPOE26 displays similar structure at 20°C over the range 47-50 wt.% (Figure 3-12a). The two most prominent reflections at 0.275 and 0.5497 nm^{-1} have a ratio 1:2 and are compatible with lamllar structure, while the rest of the peaks have a peak position ratio of $\sqrt{8}$: $\sqrt{14}$: $\sqrt{16}$: $\sqrt{20}$: $\sqrt{21}$: $\sqrt{24}$. A plot of $1/d_{hkl}$ vs. m shows the second set of peaks matches well with $Ia\bar{3}d$ symmetry as for mChPH27 (Figure 3-12b). The observed reflections suggest the material exhibits coexistance of lamellar and cubic structures. Coexisting lamellar and cubic phases have been observed in other literature,[53,54] and such coexistence is allowed by the phase rule since the copolymer/water mixture is a two component system. Reflections corresponding to $\sqrt{6}$ and $\sqrt{26}$ (211 and 431), which are observed in mChPH27 but not in mChPOE26, are expected to present at 0.2615 and 0.5443 nm^{-1}. However, these peaks are not observed, likely due to an overlap in these regions with the more pronounced peaks from the lamellar phase. The lattice parameter obtained from the plot is 58.3 nm which is very close to the value obtained for mChPH27 (58.4 nm).

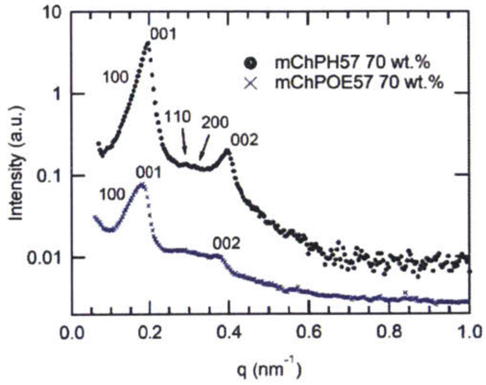

Figure 3-13. Representative SAXS curves for perforated lamellar (PL) phase of 70 wt.% bioconjugate solutions measured at 35°C.

At the largest coil fraction of $\phi_{\text{polymer}} = 0.7$, a lamellar morphology is observed for both conjugates across most of the ordered region (Figure 3-6 c,f). Phase diagrams of mChPH57 and mChPOE57 are qualitatively similar with slight differences in the C_{ODT} and the location of the perforated lamellar (PL) phase. mChPH57 and mChPOE57 initially order into nonbirefringent lamellae upon increasing concentration, and the C_{ODT} of mChPH57 is observed to be 10 wt.% lower than that of mChPOE57. The nonbirefringent lamellar phase becomes birefringent as concentration increases, and the lamellar odering dominates the phase behavior up to 60 wt.%. Although lamellae are formed independent of temperature in this region, ordering decreases slighty with increasing temperature, as evidenced by smaller peak intensities in SAXS, the disappearance of third order reflections, and the gradual loss of birefringence on heating. Both display a perforated lamellar phase at 70 wt.% suggested by an asymmetric primary peak and additional reflections between q* and 2q* (Figure 3-13) as previous observed in mCherry-*b*-PNIPAM.[15,17] mChPH57 forms a perforated lamellar phase (PL) at all temperatures at 70 wt.%, while mChPOE57 maintains the lamellar ordering for most temperatures at 70 wt.% with appearance of the perforated lamellar phase at 35°C.

Common phase behaviors between different protein-polymer conjugates are revealed by the comparison of mCherry-*b*-PHPA, mCherry-*b*-POEGA, and previously reported mCherry-*b*-PNIPAM. Conjugates with the smallest coil fractions exhibit large regions of weakly ordered lamellar or hexagonally packed structures. Conjugates with near symmetric coil fractions display the richest phase behaviors, undergoing a lyotropic ODT from a disordered phase to a lamellar morphology and lyotropic and thermotropic OOTs to form hexagonally packed cylinders. At large polymer volume fractions, the phase behaviors of the conjugates are represented by large regions of lamellar ordering. A re-entrant order-disorder transition to form a nematic phase in highly concentrated solutions is also observed.

Comparison of ordered nanostructures between mCherry-*b*-PHPA and mCherry-*b*-POEGA conjugates and previously studied PNIPAM conjugates shows that changing the chemistry of the polymer block results in both changes in the location of the phase transition lines and the appearance of a cubic phase not observed in previous studies. Concentrated solutions of symmetric mCherry-*b*-PNIPAM bioconjugates tend to form perforated lamellar phases (PL) in a very narrow range between lamellae and hexagonally packed cylinders instead of the cubic phases observed in mCherry-*b*-PHPA and mCherry-*b*-POEGA. In traditional coil-coil block copolymer systems, nonequilibrium perforated lamellar phases or equiilibrium gyroid phases occur within a narrow range of volume fractions between lamellae and cylinders.[55,56] It is possible that perforated lamellae are at least kinetically preferred in mCherry-*b*-PNIPAM[17,25] because of its higher segregation strength and greater packing frustration, consistent with hypothesized stronger repulsive interactions between mCherry and PNIPAM than between mCherry and the other polymers considered.

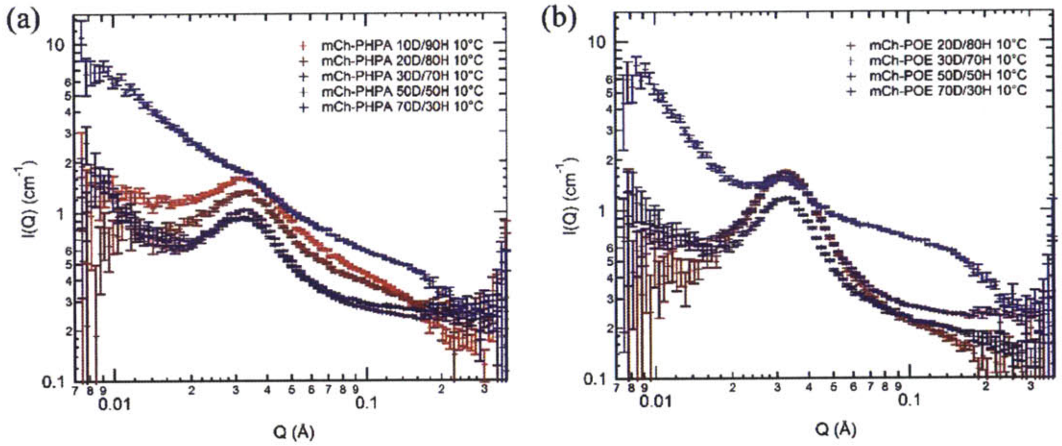

Figure 3-14. Small-angle neutron scattering absolute intensities of (a) mChPH27 and (b) mChPOE26 in different D_2O/H_2O blend compositions at T = 10°C.

Table 3-3. Scattering length densities (SLDs) of molecules. SLDs were computed using the Scattering Length Density Calculator from the NIST Center for Neutron Research.

Molecule	Density (g/cm^3)	Molecular Formula	SLD (Å^2)
Cherry	1.35	$C_{1250}H_{1915}N_{341}O_{377}S_{12}$	1.9e-6
PHPA	1.162	$C_6H_{10}O_3$	1.07e-6
POEGA	1.05	$C_{6.9}H_{11.9}O_{3.5}$ (monomer composition of 53/47)	9.08e-7
H_2O	1.00	H_2O	-5.6e-7
D_2O	1.107	D_2O	6.37e-6

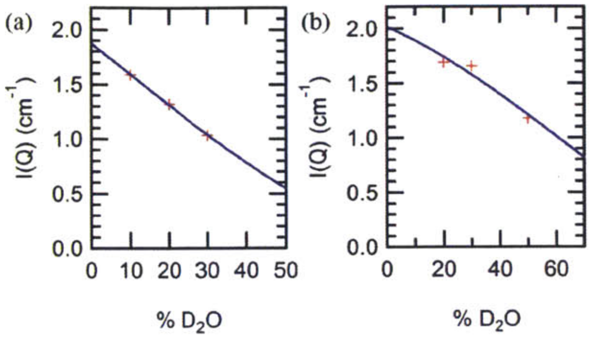

Figure 3-15. Small-angle neutron scattering peak intensities (data points) and curve fits (solid line) for (a) mChPH27 and (b) mChPOE26 in different D_2O/H_2O blend compositions at 10 °C.

Irrespective of the specific polymer block chemistry, the order of apperance of the nanostructured morphologies is similar for all block copolymers: lamellar, perforated lamellar or cubic, and hexagonal phases appear in that order with increasing temperature and concentration, although not all phases are observed in each material. These thermotropic and lyotropic order-order transitions can be understood based upon water partitioning. Hydration of the protein and polymer domains is observed to be similar for the different polymer blocks PNIPAM, PHPA, and POEGA, measured by SANS contrast variation (Figure 3-14). SANS contrast variation was performed using a number of D_2O%/H_2O% solvent compositions from 10/90 to 70/30, but due to macrophase separation observed in solvent compositions comprising a majority percentage of D_2O, data analysis was limited to the results obtained in solvent compositions in which the H_2O/D_2O volume percent ratio was at least 1. Using calculated scattering length densities for each molecular component (Table 3-3), the scattering contrast between protein and polymer domains was was calculated as a function of water partitioning in the block copolymer using a two-parameter model as reported previously for mCherry-*b*-PNIPAM.[17] From SANS contrast variation, fitting results (Figure 3-15) show that approximately 59% of the water is located within both the PHPA and POEGA domains for mChPH27 and mChPOE26, respectively, similar to previous calculations of approximately 64% of the water hydrating the PNIPAM domains for mCherry-*b*-PNIPAM27k. Calculations show that the ratio of the water volume fraction in the polymer domain to that in the protein domain ($\phi_{\mathrm{water,polymer}}/\phi_{\mathrm{water,protein}}$) is 0.75/0.67 for mCherry-*b*-PNIPAM, 0.75/0.70 for mCherry-*b*-PHPA, and 0.72/0.68 for mCherry-*b*-POEGA.

Due to the slightly preferential hydration of the polymer block, as concentration increases, the volume fraction of the polymer domain decreases faster than that of the protein domains. This leads to an order-order transition to a morphology in which the polymer volume fraction is effectively smaller. Because increasing temperature also results in desolvation of the polymer block, increasing temperature and concentration trigger similar phase transitions. Minimal differences in hydration between mCherry and all three different polymer domains at low temperature suggest that the differences in protein-polymer interactions have a greater effect on the observed trend in C_{ODT} than differences in selective hydration.

While not quantitative, the application of polymer solution theory concepts to this system further suggests that a major impact of changing polymer is to tune the protein-polymer interaction. Changing monomers used in the synthetic polymer block is not expected to create a large change in entropy of mixing because coarse-grained theories of polymer solutions (i.e. Flory Huggins theory[57] and Leibler's RPA theory[58] of block copolymers) show that the dominant entropy of mixing contribution is a function of only the relative volume fraction (degree of polymerization) of the two blocks. Because polymer volume fractions in bioconjugates are carefully controlled and the protein block has the same colloidal size and shape in each conjugate, little change in mixing entropy is expected. Each of the polymers also has a similar degree of polymerization and is studied in the vicinity of its thermoresponsive transition temperature, where the Flory-Huggins interaction parameter between polymer and solvent is expected to cross from less than 0.5 to greater than 0.5 upon increasing temperature. Therefore, although POEGA and PHPA are expected to have a somewhat higher χ parameter as a function of temperature than PNIPAM due to their lower transition temperatures, the investigation of all polymers at temperatures in the vicinity of the responsive transition temperature suggests that solvent-mediated polymer-polymer interactions are not a large difference between systems. This is consistent with the similar hydration observed by SANS.

The asymmetric nature of phase space as a function of polymer volume fractions is observed for all three polymers. Based on 50~60 wt.% solution nanostructures where the best ordering is observed, conjugates with a polymer fraction less than approximately 0.5 tend to form hexagonally packed cylinders, while conjugates with polymer volume fractions greater than 0.5 tend to form lamellae. Cylinders are not observed on the high coil fraction side of the phase diagram, and the body-centered cubic spherical phase (BCC) is not observed in all three polymers studied. This is further supported by a detailed study on phase behavior as a function of concentration and coil fraction for mCherry-*b*-PNIPAM where no BCC phase or cylinders with protein core were observed.[25] The asymmetry as well as no occurrence of a spherical phase can be attributed to the geometric molecular asymmetry in the protein-polymer diblock copolymers arising from the presence of the globular and rigidly folded mCherry. The observation that the lamellar phase is thermodynamically favored when polymer volume fracion is much higher than 0.5 is consistent with previous observations of assymmetrically shaped block copolymers.[59–62]

3.5 Conclusion

The self-assembly of globular protein-polymer conjugates comprising the red fluorescent protein mCherry and the thermoresponsive polymers PHPA and POEGA shows that changing polymer-protein interactions by changing polymer block chemistry has a large impact on the type of self-assembled phases formed, the location of phase transitions, and the presence of macrophase separation at high temperatures. Changing polymer chemistry and the resultant protein-interactions affect the order-disorder transition concentration: mCherry-*b*-PNIPAM is observed to have the lowest C_{ODT}, while mCherry-*b*-POEGA conjugates have the highest C_{ODT}. The occurance of the C_{ODT} at symmetric compositions suggests that this behavior is driven by changes in the strength of effective repulsive interactions between protein and polymer. A new phase with $Ia\bar{3}d$ symmetry is observed in mCherry-*b*-PHPA and mCherry-*b*-POEGA, instead of the perforated lamellar (PL) phase formed by mCherry-*b*-PNIPAM near-symmetric conjugates. Macrophase separation occurs more readily in mCherry-*b*-PNIPAM than either mCherry-*b*-PHPA or mCherry-*b*-POEGA, suggesting that the different polymer chemistries and their respective thermoresponsive behaviors affect the stability of a two-phase region at high temperatures.

General features common to the self-assembly of all three conjugates are also revealed. All three bioconjugates have a microphase separation region between approximately 40 and

70 wt.% with lamellar or cylindrical phases, which are commonly observed in traditional coil-coil diblock copolymers, and bioconjugate solutions with higher concentration display a re-entrant ODT behavior. Weakly ordered nematic phases formed by mCherry-*b*-PHPA and mCherry-*b*-POEGA suggest that liquid crystalline ordering at high concentration arises from the presence of protein. The asymmetric nature of the phase diagram as a function of coil fraction is also common among the three bioconjugates. Regardless of coil fraction, bioconjugates always form ordered phases in the order lamellar, perforated lamellar or cubic, and hexagonal as concentration or temperature are increased.

Acknowledgements

This work was supported by Air Force Office of Scientific Research (award number FA9550-12-0259). Department of Energy Office of Basic Energy Sciences (award number DE-SC0007106) supported neutron scattering studies of polymer hydration. We thank Dr. Lixia Rong and Dr. Maya Koga for experimental assistance at NSLS beamline X27C at Brookhaven National Laboratory, and Dr. William T. Heller for experimental assistance with SANS at EQ-SANS at Oak Ridge National Laboratory. The authors are grateful to the Keating lab at MIT for use of CD instrument. NMR was measured in MIT DCIF and polarized optical microscopy was conducted in the Institute for Soldier Nanotechnologies.

3.6 References

(1) Reda, T.; Plugge, C. M.; Abram, N. J.; Hirst, J. Reversible Interconversion of Carbon Dioxide and Formate by an Electroactive Enzyme. *Proc. Natl. Acad. Sci. U. S. A.* **2008**, *105*, 10654–10658.

(2) Hambourger, M.; Gervaldo, M.; Svedruzic, D.; King, P. W.; Gust, D.; Ghirardi, M.; Moore, A. L.; Moore, T. A. [FeFe]-Hydrogenase-Catalyzed H2 Production in a Photoelectrochemical Biofuel Cell. *J. Am. Chem. Soc.* **2008**, *130*, 2015–2022.

(3) Heller, A. Electrical Connection of Enzyme Redox Centers to Electrodes. *J. Phys. Chem.* **1992**, *96*, 3579–3587.

(4) Drevon, G. F.; Russell, A. J. Irreversible Immobilization of Diisopropylfluorophosphatase in Polyurethane Polymers. *Biomacromolecules* **2000**, *1*, 571–576.

(5) Ferreira, M.; Fiorito, P. A.; Oliveira, O. N.; de Torresi, S. I. C. Enzyme-Mediated Amperometric Biosensors Prepared with the Layer-by-Layer (LbL) Adsorption Technique. *Biosens. Bioelectron.* **2004**, *19*, 1611–1615.

(6) He, J. A.; Samuelson, L.; Li, L.; Kumar, J.; Tripathy, S. K. Oriented Bacteriorhodopsin/polycation Multilayers by Electrostatic Layer-by-Layer Assembly. *Langmuir* **1998**, *14*, 1674–1679.

(7) Das, R.; Kiley, P. J.; Segal, M.; Norville, J.; Yu, A. A.; Wang, L.; Trammell, S. A.; Reddick, L. E.; Kumar, R.; Stellacci, F.; *et al.* Integration of Photosynthetic Protein Molecular Complexes in Solid-State Electronic Devices. *Nano Lett.* **2004**, *4*, 1079–1083.

(8) Olsen, B. D. Self-Assembly of Globular-Protein-Containing Block Copolymers. *Macromol. Chem. Phys.* **2013**, *214*, 1659–1668.

(9) Cracknell, J. a.; Vincent, K. a.; Armstrong, F. a. Enzymes as Working or Inspirational Electrocatalysts for Fuel Cells and Electrolysis. *Chem. Rev.* **2008**, *108*, 2439–2461.

(10) Kumar, N.; Hahm, J. I. Nanoscale Protein Patterning Using Self-Assembled Diblock Copolymers. *Langmuir* **2005**, *21*, 6652–6655.

(11) Presley, A. D.; Chang, J. J.; Xu, T. Directed Co-Assembly of Heme Proteins with Amphiphilic Block Copolymers toward Functional Biomolecular Materials. *Soft Matter* **2011**, *7*, 172–179.

(12) Shan, W. J.; He, P. L.; Hu, N. F. Electrocatalytic Reduction of Nitric Oxide and Other Substrates on Hydrogel Triblock Copolymer Pluronic Films Containing Hemoglobin or Myoglobin Based on Protein Direct Electrochemistry. *Electrochim. Acta* **2005**, *51*, 432–440.

(13) Jia, S. S.; Fei, J. J.; Deng, J. J.; Cai, Y. L.; Li, J. A. Direct Electrochemistry and Electrocatalysis of Hemoglobin Immobilized in an Amphiphilic Diblock Copolymer Film. *Sensors and Actuators B-Chemical* **2009**, *138*, 244–250.

(14) Cardoso, M. B.; Smolensky, D.; Heller, W. T.; Hong, K. L.; O'Neill, H. Supramolecular Assembly of Biohybrid Photoconversion Systems. *Energy Environ. Sci.* **2011**, *4*, 181–188.

(15) Thomas, C. S.; Glassman, M. J.; Olsen, B. D. Solid-State Nanostructured Materials from Self-Assembly of a Globular Protein-Polymer Diblock Copolymer. In *ACS Nano*; American Chemical Society, 2011; Vol. 5, pp. 5697–5707.

(16) Thomas, C. S.; Xu, L.; Olsen, B. D. Kinetically Controlled Nanostructure Formation in Self-Assembled Globular Protein–Polymer Diblock Copolymers. *Biomacromolecules* **2012**, *13*, 2781–2792.

(17) Lam, C. N.; Olsen, B. D. Phase Transitions in Concentrated Solution Self-Assembly of Globular Protein–polymer Block Copolymers. *Soft Matter* **2013**, *9*, 2393.

(18) Chilkoti, A.; Chen, G.; Stayton, P. S.; Hoffman, A. S. Site-Specific Conjugation of a Temperature-Sensitive Polymer to a Genetically Engineered Protein. *Bioconjug. Chem.* **1994**, *5*, 504–507.

(19) Heredia, K. L.; Maynard, H. D. Synthesis of Protein–polymer Conjugates. *Org. Biomol. Chem.* **2007**, *5*, 45–53.

(20) De, P.; Li, M.; Gondi, S. R.; Sumerlin, B. S. Temperature-Regulated Activity of Responsive Polymer– Protein Conjugates Prepared by Grafting-from via RAFT Polymerization. *J. Am. Chem. Soc.* **2008**, *130*, 11288–11289.

(21) Lavigueur, C.; Garcia, J. G.; Hendriks, L.; Hoogenboom, R.; Cornelissen, J. J. L. M.; Nolte, R. J. M. Thermoresponsive Giant Biohybrid Amphiphiles. *Polym. Chem.* **2011**, *2*, 333–340.

(22) Boerakker, M. J.; Botterhuis, N. E.; Bomans, P. H. H.; Frederik, P. M.; Meijer, E. M.; Nolte, R. J. M.; Sommerdijk, N. a J. M. Aggregation Behavior of Giant Amphiphiles Prepared by Cofactor Reconstitution. *Chem. - A Eur. J.* **2006**, *12*, 6071–6080.

(23) Xia, Y.; Tang, S.; Olsen, B. D. Site-Specific Conjugation of RAFT Polymers to Proteins via Expressed Protein Ligation. *Chem. Commun.* **2013**, *49*, 2566–2568.

(24) Reynhout, I. C.; Cornelissen, J. J. L. M.; Nolte, R. J. M. Self-Assembled Architectures from Biohybrid Triblock Copolymers. *J. Am. Chem. Soc.* **2007**, *129*, 2327–2332.

(25) Thomas, C. S.; Olsen, B. D. Coil Fraction-Dependent Phase Behaviour of a Model Globular Protein–polymer Diblock Copolymer. *Soft Matter* **2014**, *10*, 3093–3102.

(26) Bates, F. S. Polymer-Polymer Phase Behavior. *Science* **1991**, *251*, 898–905.

(27) Bates, F. S.; Fredrickson, G. H. Block Copolymers—Designer Soft Materials. *Phys. Today* **1999**, *52*, 32–38.

(28) Matsen, M. W.; Bates, F. S. Block Copolymer Microstructures in the Intermediate-Segregation Regime. *J. Chem. Phys.* **1997**, *106*, 2436.

(29) McConnell, G. a; Gast, a P. Melting of Ordered Arrays and Shape Transitions in Highly Concentrated Diblock Copolymer Solutions. *Macromolelcules* **1997**, *30*, 435–444.

(30) Barton, A. F. M. *Handbook of Polymer-Liquid Interaction Parameters and Solubility Parameters*; Taylor & Francis, 1990.

(31) Zengin, A.; Caykara, T. RAFT-Mediated Synthesis of Poly[(oligoethylene Glycol) Methyl Ether Acrylate] Brushes for Biological Functions. *J. Polym. Sci. Part A Polym. Chem.* **2012**, *50*, 4443–4450.

(32) Lam, C. N.; Kim, M.; Thomas, C. S.; Chang, D.; Sanoja, G. E.; Okwara, C. U.; Olsen, B. D. The Nature of Protein Interactions Governing Globular Protein–Polymer Block Copolymer Self-Assembly. *Biomacromolecules* **2014**, *15*, 1248–1258.

(33) Helfand, E.; Tagami, Y. Theory of the Interface between Immiscible Polymers. II. *J. Chem. Phys.* **1972**, *56*, 3592–3601.

(34) Zhang, K.; Khan, A. Phase Behavior of Poly(ethylene Oxide)-Poly(propylene Oxide)-Poly(ethylene Oxide) Triblock Copolymers in Water. *Macromolecules* **1995**, *28*, 3807–3812.

(35) Noolandi, J.; Shi, A.; Linse, P. Theory of Phase Behavior of Poly(oxyethylene)-Poly(oxypropylene)-Poly(oxyethylene) Triblock Copolymers in Aqueous Solutions. *Macromolecules* **1996**, *29*, 5907–5919.

(36) Shibaev, V. P.; Plate, N. A. THERMOTROPIC LIQUID-CRYSTALLINE POLYMERS WITH MESOGENIC SIDE GROUPS. *Adv. Polym. Sci.* **1984**, *60-1*, 173–260.

(37) Robinson, C. Liquid-Crystalline Structures in Polypeptide Solutions. *Tetrahedron* **1961**, *13*, 219–234.

(38) Bawden, F. C.; Pirie, N. W.; Bernal, J. D.; Fankuchen, I. Liquid Crystalline Substances from Virusinfected Plants. *Nature* **1936**, *138*, 1051–1052.

(39) Zweckstetter, M.; Bax, A. Characterization of Molecular Alignment in Aqueous Suspensions of Pf1 Bacteriophage. *J. Biomol. Nmr* **2001**, *20*, 365–377.

(40) Corrigan, A. M.; Müller, C.; Krebs, M. R. H. The Formation of Nematic Liquid Crystal Phases by Hen Lysozyme Amyloid Fibrils. *J. Am. Chem. Soc.* **2006**, *128*, 14740–14741.

(41) Jung, J.-M.; Mezzenga, R. Liquid Crystalline Phase Behavior of Protein Fibers in Water: Experiments versus Theory. *Langmuir* **2009**, *26*, 504–514.

(42) Onsager, L. The Effects of Shape on the Interaction of Colloidal Particles. *Ann. N. Y. Acad. Sci.* **1949**, *51*, 627–659.

(43) Dumetz, A. C.; Chockla, A. M.; Kaler, E. W.; Lenhoff, A. M. Protein Phase Behavior in Aqueous Solutions: Crystallization, Liquid-Liquid Phase Separation, Gels, and Aggregates. *Biophys. J.* **2008**, *94*, 570–583.

(44) Thomson, J. A.; Schurtenberger, P.; Thurston, G. M.; Benedek, G. B. Binary-Liquid Phase-Separation and Critical Phenomena in a Protein Water Solution. *Proc. Natl. Acad. Sci. U. S. A.* **1987**, *84*, 7079–7083.

(45) Gennes, P. G. de; Prost, J. *The Physics of Liquid Crystals*; Clarendon Press, 1995.

(46) Kurut, A.; Persson, B. A.; Akesson, T.; Forsman, J.; Lund, M. Anisotropic Interactions in Protein Mixtures,: Self Assembly and Phase Behavior in Aqueous Solution. *J. Phys. Chem. Lett.* **2012**, *3*, 731–734.

(47) Balsara, N. P.; Garetz, B. a.; Dai, H. J. Relationship between Birefringence and the Structure of Ordered Block Copolymer Materials. *Macromolecules* **1992**, *25*, 6072–6074.

(48) Balsara, N. P.; Perahia, D.; Safinya, C. R.; Tirrell, M. V.; Lodge, T. P. Birefringence Detection of the Order-to-Disorder Transition in Block Copolymer Liquids. *Macromolecules* **1992**, *25*, 3896–3901.

(49) Hajduk, D. A.; Harper, P. E.; Gruner, S. M.; Honeker, C. C.; Kim, G.; Thomas, E. L.; Fetters, L. J. The Gyroid - a New Equilibrium Morphology in Weakly Segregated Diblock Copolymers. *Macromolecules* **1994**, *27*, 4063–4075.

(50) Vigild, M. E.; Almdal, K.; Mortensen, K.; Hamley, I. W.; Fairclough, J. P. A.; Ryan, A. J. Transformations to and from the Gyroid Phase in a Diblock Copolymer. *Macromolecules* **1998**, *31*, 5702–5716.

(51) Matsen, M. W. Gyroid versus Double-Diamond in ABC Triblock Copolymer Melts. *J. Chem. Phys.* **1998**, *108*, 785–796.

(52) Alexandridis, P.; Olsson, U.; Lindman, B. A Record Nine Different Phases (Four Cubic, Two Hexagonal, and One Lamellar Lyotropic Liquid Crystalline and Two Micellar Solutions) in a Ternary Isothermal System of an Amphiphilic Block Copolymer and Selective Solvents (Water and Oil). *Langmuir* **1998**, *14*, 2627–2638.

(53) Conn, C. E.; Ces, O.; Mulet, X.; Finet, S.; Winter, R.; Seddon, J. M.; Templer, R. H. Dynamics of Structural Transformations between Lamellar and Inverse Bicontinuous Cubic Lyotropic Phases. *Phys. Rev. Lett.* **2006**, *96*, 108102.

(54) Crisci, A.; Hay, D. N. T.; Seifert, S.; Firestone, M. A. pH- and Ionic-Strength-Induced Structural Changes in Poly(acrylic Acid)-Lipid-Based Self-Assembled Materials. *Macromol. Symp.* **2009**, *281*, 126–134.

(55) Forster, S.; Khandpur, A. K.; Zhao, J.; Bates, F. S.; Hamley, I. W.; Ryan, A. J.; Bras, W. Complex Phase-Behavior of Polyisoprene-Polystyrene Diblock Copolymers near the Order-Disorder Transition. *Macromolecules* **1994**, *27*, 6922–6935.

(56) Hajduk, D. A.; Takenouchi, H.; Hillmyer, M. A.; Bates, F. S.; Vigild, M. E.; Almdal, K. Stability of the Perforated Layer (PL) Phase in Diblock Copolymer Melts. *Macromolecules* **1997**, *30*, 3788–3795.
(57) Flory, P. J. *Principles of Polymer Chemistry*; Cornell University Press, 1953.
(58) Leibler, L. Theory of Microphase Separation in Block Copolymers. *Macromolecules* **1980**, *13*, 1602–1617.
(59) Thomas, E. L.; Chen, J. T.; ORourke, M. J. E.; Ober, C. K.; Mao, G. P. Influence of a Liquid Crystalline Block on the Microdomain Structure of Block Copolymers. *Macromol. Symp.* **1997**, *117*, 241–256.
(60) Olsen, B. D.; Segalman, R. A. Structure and Thermodynamics of Weakly Segregated Rod-Coil Block Copolymers. *Macromolecules* **2005**, *38*, 10127–10137.
(61) Olsen, B. D.; Segalman, R. a. Nonlamellar Phases in Asymmetric Rod-Coil Block Copolymers at Increased Segregation Strengths. *Macromolecules* **2007**, *40*, 6922–6929.
(62) Olsen, B. D.; Shah, M.; Ganesan, V.; Segalman, R. a. Universalization of the Phase Diagram for a Model Rod- Coil Diblock Copolymer. *Macromolecules* **2008**, *41*, 6809–6817.

Chapter 4. Kinetic Effects on Self-Assembly of Protein-Polymer Bioconjugates in Thin Films Prepared by Flow Coating

4.1 Abstract

The self-assembly of nanostructured globular protein arrays in thin films is demonstrated using protein-polymer block copolymers based on a model protein mCherry and the polymer poly(oligoethylene glycol acrylate). A conjugate block copolymer with polymer volume fraction 0.54 is self-assembled in thin films on a poly(ethylene oxide) grafted Si surface using flow coating, forming cylindrical nanostructures similar to those observed in bulk self-assembly. Selective segregation of the polymer block to the air-film and film-substrate interfaces templates parallel orientation of cylinders. Solvent evaporation rate is essential in determining degree of order and arrangement of cylinders. While films prepared at low relative humidity show a low degree of order and lack of preferred arrangement of cylinders, films prepared at high relative humidity show preferential arrangement of parallel cylinders along the cylinder axis with long range order. Annealing of films prepared at low relative humidity is not effective in achieving well-ordered structures but films coated at high speed show greater long-range order than films coated at low speed due to reduced nucleation per unit area of drying film.

4.2 Materials and Methods

Poly(oligoethylene glycol acrylate) (POEGA) was synthesized as previously reported.[1] The bioconjugation reaction between mCherryS131C and 6 molar equivalent of the deprotected polymer was carried out at 4°C in 20 mM Tris buffer (pH 8.0) overnight and purified using three precipitations in ammonium sulfate and Ni-NTA chromatography. The purity of final bioconjugate is shown in the protein denaturing gel in Figure 4-7 indicating no free mCherry contamination. The small fragment band represents a fragment cleaved off from mCherry due to partial hydrolysis of the mCherry chromophore acylimine bond during boiling process for SDS-PAGE.[2–6] Bioconjugate solutions were concentrated to approximately 250-300 mg/ml using centrifugal filters with a molecular weight cut-off of 10 kDa. Solutions were diluted to a desired concentration based on the concentration estimated from UV-vis absorption at a wavelength 280 nm.

Silicon wafers were purchased from Wafer World (P-type Silicon with boron as dopant, orientation: (100), single-side polished). A wafer was rinsed in acetone and treated with oxygen plasma for 5 minutes immediately before use. Poly(ethylene glycol) methyl ether (PEG) (M_n=750 g/mol) was purchased from Sigma-Aldrich. A cleaned wafer was submerged in PEG melt and heated at 150°C for 24 hours under vacuum to induce the thermal dehydration coupling reaction. Wafers were rinsed in acetone afterwards. The presence of PEG layer was confirmed by X-ray photoelectron spectroscopy (XPS) of a PEG grafted silicon substrate. A high resolution scan shows the dominant presence of a carbon species with binding energy 286.5 eV, as well as a small peak centered at 285.0 eV which corresponds to an aliphatic carbon when calibrated using an internal standard Si2p peak to be 99.0 eV (Figure 4-8a). It has been reported that carbon species in PEO has binding energy 286.45 eV.[7] The presence of the small amount of aliphatic carbon is presumed to be due to an initial contaminant in the bare silicon wafer which was not completely removed after plasma cleaning as shown by survey scans in Figure 4-8b. Thickness of PEG layer was estimated to be 0.656 nm based on ellipsometry.

A flow coater was built following plans from a previously reported design.[8] A humidity chamber was custom-built around the flow coater. A 1-inch wide glass slide was cut into half to generate 0.5-inch wide glass slide, which was used as a blade. The angle of the blade was fixed at 5° throughout experiments. After blade touches the substrate by visual inspection, the 100 TPI fine adjustment screw (254 μm per revolution) that controls the z-position of the blade was turned 180° clockwise to lift the blade by 127 μm. 4 μl of bioconjugate solution of concentration from 15 wt.% to 30 wt.% was injected between the blade and the substrate. Wet films were prepared by moving the stage at a constant speed using CME2 software provided by Copley Controls. Films were allowed to dry in the humidity chamber which was almost instantaneous for RH 10% and took seconds for RH 80%. Films were taken out to ambient air afterwards. Flow coating was conducted at room temperature. Relative humidity was measured using a VWR digital hygrometer (temperature range 0 to 50°C, humidity range 25 to 95% RH, 0.1°C and 1% RH resolution). For annealing, films were immediately cut into small pieces with an approximate dimension 1 cm by 1 cm, and annealed on a 50 ml beaker (5.5 cm high) put upside down in a 180 ml glass jar (8 cm high) filled with 5 ml of 0.5M NaCl solution. The lid for the glass jar was open to terminate annealing process and the films were stored at ambient condition for a few hours to dry. Films were stored in a sealed 6-well plate afterwards, where the structure as measured by GISAXS was stable for at least 5 months.

X-ray photoelectron spectroscopy was conducted using PHI Versaprobe II XPS with a monochromated Al source (50W) with a spot size 200 μm. Chemical composition was analyzed from data measured at three different positions in a film to account for statistical variation across the film surface. Data were corrected using manufacturer-supplied relative sensitivity factors, smoothed using SG7 mechanism, background subtracted to integrate for quantification. Data were calibrated based on binding energy of aliphatic carbon 285.0 eV unless noted otherwise.

Depth profiling experiments were conducted using a C60 cluster-ion gun operated at 10kV and 10nA with a raster scan size 4 by 4 mm and sputtering time with 1 minute interval.

The surface morphologies were studied using a NT-MDT Ntegra Prima scanning force microscope (SFM) in intermittent contact mode. The phase images were post-processed using first order corrections and the height image in Figure 4-10 was processed using fifth order corrections. Film thicknesses were measured using ellipsometry based on wavelengths between 800 and 1000 nm outside the mCherry absorbance/emission range.

Grazing incidence small angle X-ray scattering (GISAXS) experiments were conducted at beamline 8-ID-E at Argonne National Laboratory using X-ray with energy 7.35 keV. Samples were measured under ambient conditions at two incident angles (α_i) 0.20 and 0.22° between the critical angle of silicon 0.24° and the critical angle of bioconjugate film 0.18°, and the reported images are from an incident angle 0.20.

Fluorescence was measured using Horiba Jobin Yvon Fluorolog-3. Films were illuminated at 45° angle with incident light wavelength 550 nm and slitwidth 1, and the emission spectrum between 565 and 750 nm was recorded on front detector. mCherryS131C solution in 20 mM Tris-Cl buffer (pH. 8.0) is measured in a cuvette with 10 mm pathlength, and the fluorescence is measured using the right angle detector. The intensity was divided by a reference signal to correct for lamp intensity variation, and signal from bare Si wafer or 20 mM Tris-Cl buffer (also corrected for lamp intensity variation) was subtracted to account for background signal for films or solution, respectively.

4.3 Results and Discussion

The ability of proteins to catalyze reactions with high specificity at mild temperature in environmentally friendly solvents makes them very attractive candidates for catalytic devices.[9] Many applications require coating the proteins as thin films, such as electrocatalysts or biosensors.[10,11] In addition to careful selection of an immobilization method to preserve protein structures,[9,12] successful application in thin film geometries require control of surface interactions because proteins may undergo denaturation upon interaction with solid surfaces or air.[13–15] A high density of protein loading is generally desirable in order to obtain high activity per film area.[16] Controlling protein orientation and substrate, product, or charge carrier transport through the material is also critical for proper function, which necessitates nanostructural control in protein-immobilized materials.[17]

Many approaches have been developed to prepare nanostructured protein thin films, including lithographic patterning of 2D layers[18] and encapsulation in thicker films. Films solely made of proteins without internal nanostructures can be prepared by laser-assisted[19] or electrospray deposition,[20] and the resultant films have a very high density of proteins. Various enzymes have also been assembled with polyelectrolytes in layer-by-layer fashion.[21–23] Thin films can be prepared from coacervate core micelles with proteins electrostatically complexed in the core,[24] or enzymes can be co-assembled within lipid[25] or polymer templates.[26,27]

Block copolymer self-assembly is a widely used technique to control nanostructure in thin films, and our group has recently demonstrated that this technique may be applied to form nanostructured bulk materials directly using block copolymers containing one enzyme or fluorescent protein block and one polymer block.[6,28–30] These materials can form nanostructures such as lamellae, perforated lamellae, cylinders, and gyroids due to immiscibility between the protein and polymer blocks as a function of coil fraction, temperature, and concentration. This approach to preparing nanomaterials shows great promise in achieving high density protein loading, maintenance of protein activity, and control over the structural arrangement of the proteins.

Translating this bulk self-assembly to thin film coatings requires understanding the effects of surface energy and spatial confinement on nanostructure formation. Surface energetics determine segregation of blocks on each surface, and the block with lower interfacial energy will wet each surface. It is important to control the surface segregation for protein-polymer bioconjugate films as proteins may undergo denaturation upon interaction with solid surfaces or air.[13–15] Incommensurability between block copolymer domain spacing and film thickness is also known to affect structure formation, resulting in the formation of islands or holes or perpendicular orientation of the morphology.[31,32] In protein-polymer bioconjugate self-assembly in thin films, it is expected that kinetics also play a large role due to a narrow range of annealing temperature and limited annealing solvents by considerations of solubility and protein stability.

In this letter, nanostuctures are studied in protein-polymer bioconjugate thin films prepared with different processing approaches. A bioconjugate made of mCherry and poly(oligoethylene glycol acrylate) (POEGA) are selected for thin film study (Figure 4-1a), as the equilibrium phase behavior in concentrated aqueous solution is known from a previous study, which is essential for analyzing thin film behavior. mCherry is selected as a model protein due to its robust structure, high yield expression and purification, and potential application in biolasers.[33,34] POEGA block has an advantage in AFM study due to the mechanical contrast from mCherry. The synthesis of this conjugate has previously been reported in detail.[30] mCherry-POEGA 26 kDa bioconjugate with an average POEGA molar mass of 26,100 g/mol, a protein molar mass of 28,134 g/mol, and a POEGA volume fraction of 0.54, forms a hexagonally packed cylindrical nanostructure in bulk when analyzed using small angle X-ray scattering (SAXS) (Figure 4-1b). The primary peak (q*) of annealed material appears at 0.26095 nm^{-1} which corresponds to inter-cylinder spacing 27.8 nm.

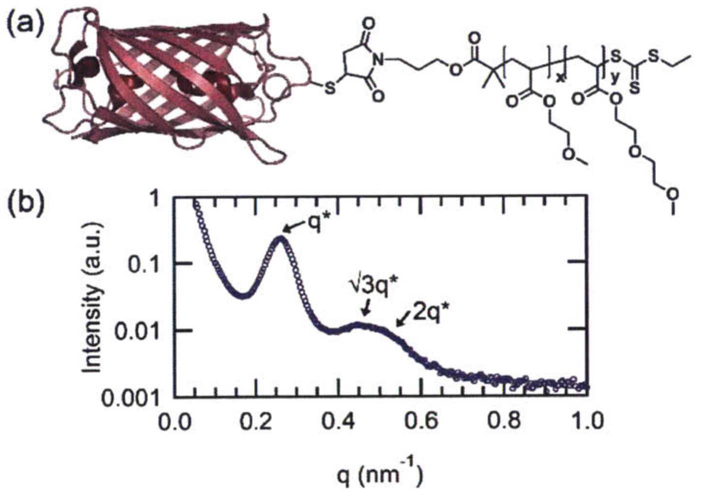

Figure 4-1. Bioconjugate used in this study. (a) Structure of mCherry-*b*-poly(oligoethylene glycol acrylate) (POEGA) 26 kDa. The x:y ratio and molecular formula are indicated in Table 4-1. (b) SAXS curve of a bulk solid sample annealed for 24 hour in water vapor.

Films are prepared from aqueous solution of mCherry-POEGA 26 kDa bioconjugate. From solution study, it has been shown that the conjugate undergoes order-disorder transition at 43 wt.%. Bioconjugate solutions with 5 - 30 wt.% concentration in deionized water are prepared and coated on Si substrates using a flow coater. Si substrates are grafted with short poly(ethylene oxide) (PEO) (M_n = 750 g/mol) prior to coating by a thermal dehydration reaction to render the surface preferential to the POEGA. The presence of PEO moiety is confirmed using X-ray photoelectron spectroscopy (XPS) (Figure 4-8). Film thickness is controlled by varying solution concentration at a constant coating speed of 15 mm/min except where noted. The blade height was kept constant at approximately 127 μm by rotating a 100 TPI fine adjustment screw (254 μm per revolution) for z-axis control by 180° clockwise after making contact between the blade and the substrate.

Table 4-1. Elemental composition of mCherryS131C, POEGA, and bioconjugate used in this study.

	Molecular formula	Theoretical N/C ratio
mCherryS131C	$C_{1250}H_{1915}N_{341}O_{377}S_{12}$	0.2728
POEGA 26 kDa*	$C_{1198}H_{2046}N_{1}O_{596}S_{3}$	0.0008
mCherryS131C-POEGA 26 kDa	$C_{2448}H_{3961}N_{342}O_{973}S_{15}$	0.1397
POEGA 57 kDa*	$C_{2647}H_{4534}N_{1}O_{1320}S_{3}$	0.0004
mCherryS131C-POEGA 57 kDa	$C_{3897}H_{6449}N_{342}O_{1698}S_{15}$	0.0878

* Molecular formulas of POEGA 26 kDa and POEGA 57 kDa are calculated based on the 53:47 and 49:51 ratio, respectively, of two monomers 2-methoxyethyl acrylate (MEA) and 2-(2-methoxyethoxy)ethyl acrylate (MEEA) as determined by nuclear magnetic resonance (NMR) spectroscopy in a previous publication.[1]

For the copolymer mCherry-POEGA, the synthetic polymer block is selective for both the air-film and substrate-film interface under conditions of solvent drying at ambient environment used to prepare the films. The selectivity is established by XPS, which may be used to determine the depth-dependent concentrations of protein and polymer based on the ratio of nitrogen to carbon atoms (N/C). While the protein is rich in nitrogen, the polymer block only has a single nitrogen present in the maleimide linker (Table 4-1). The N/C ratio of mCherry-POEGA 26 kDa is measured to be 0.077 ± 0.005 on a bioconjugate film surface with 120 nm thickness (Figure 4-

2a). The ratio is significantly lower than the theoretical N/C ratio of the bioconjugate (0.140) and the value detected inside a film with thickness 113 nm from a depth-profiling experiment (Figure 4-2b). A similar bioconjugate with larger polymer fraction, 0.72 (theoretical N/C ratio of 0.088), demonstrates an even lower surface N/C ratio of 0.011 ± 0.004 in a 125 nm-thick film. These results suggest that the POEGA blocks preferentially wet the air-film interface, and the slightly higher N/C ratio of mCherry-POEGA 26 kDa can result from XPS penetration depth exceeding the thickness of wetting layer.

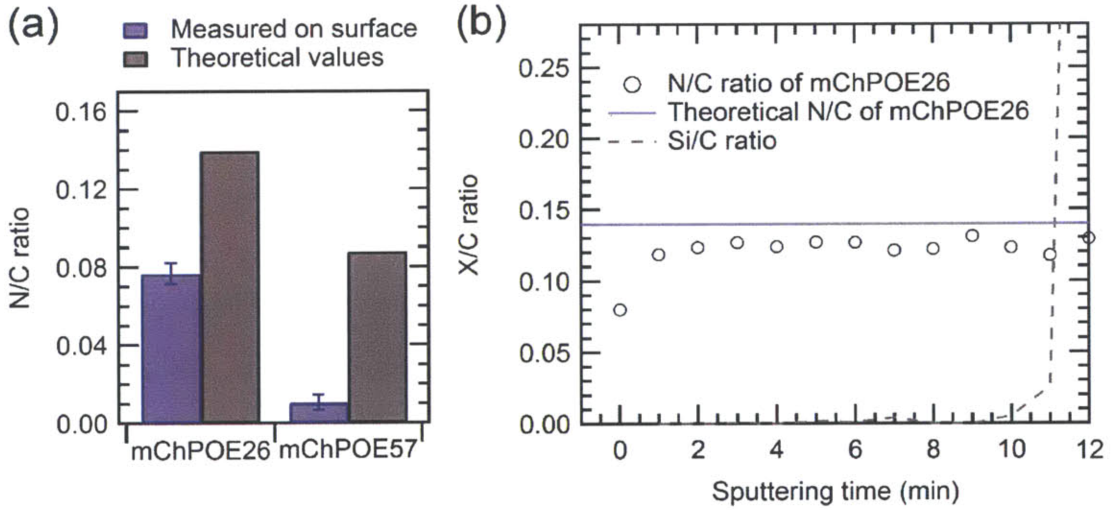

Figure 4-2. Surface segregation of bioconjugate in thin films prepared under ambient conditions analyzed by XPS. (a) Ratios of elements measured at the surface of films of mCherry-POEGA 26 kDa and mCherry-POEGA 57 kDa. Three different spots are measured within a film to account for spatial variation. (b) Elemental ratios recorded in depth profile experiment of a mCherry-POEGA 26 kDa film.

Segregation of the polymer block to the air-film interface is advantageous because interactions of proteins with air-film interface or solid support often lead to denaturation and inactivation.[13–15] Proteins are surface-active molecules due to their amphiphilic nature, and often denature and absorb at interfaces.[13–15,35] In the bioconjugate block copolymers, segregation of the low surface energy block to the air-film interface outcompetes protein segregation and denaturation in this system. The N/C ratio at 80% relative humidity is 25% lower than that at 25% relative humidity (Figure 4-9), suggesting that kinetics plays a role in driving surface segregation of the POEGA block. The stable β-barrel structure of mCherry may also help to prevent denaturing during film casting, reducing the interfacial activity of the protein.

Due to preferential wetting of the polymer block at the free and supported surfaces, cylindrical nanodomains oriented parallel to the substrate are expected to be energetically preferred. However, the solvent evaporation rate during solution casting has been shown to have a large impact on degree of ordering and orientation of nanostructures[36–38] due to kinetic constraints imposed by rapid evaporation of solvent, or from different solvent concentration gradient profile which determines direction of cylinder growth.[38] Therefore, we hypothesized high humidity in surrounding air and the resultant slow evaporation of water from the wet film produced after flow coating would lead to formation of parallel cylinders, which is energetically preferred, while fast evaporation at low humidity would result in poor ordering or perpendicular cylinders.

When films are prepared without humidification of the environment, in which relative humidity is measured to be less than 25% (<RH25, 25% is the minimum limit of hygrometer) and fast drying of films is observed, poorly ordered nanostructures are observed by atomic force microscopy (AFM) and grazing incidence small angle X-ray scattering (GISAXS). An AFM phase image of a film with thickness 49 nm (2.3 L_0 where L_0 = 21.1 nm, Figure 4-3a) shows a microphase separated structure lacking significant long-range order. A film with thickness 72

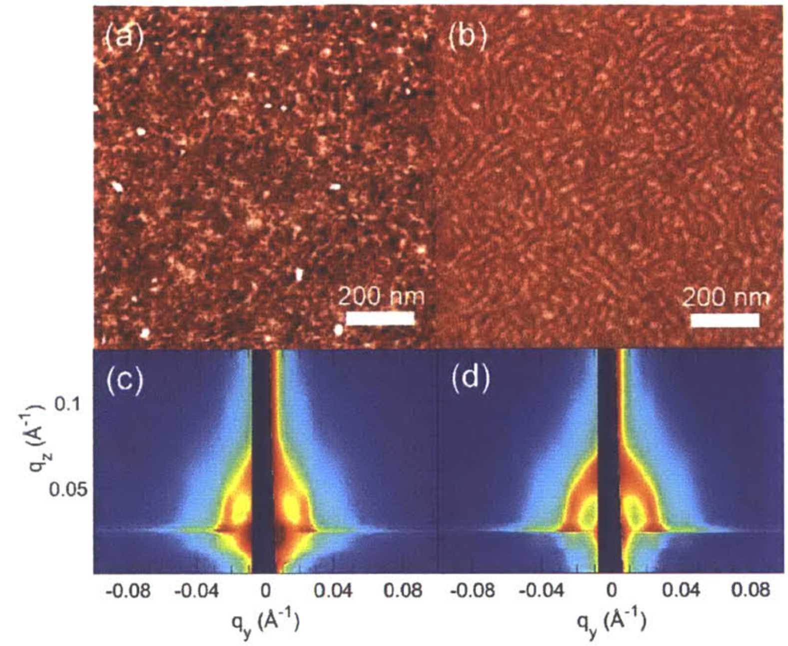

Figure 4-3. AFM phase images and GISAXS patterns showing nanostructures of films prepared at low humidity (<RH25). The thickness of the film shown in (a,c) is 49 nm and the film shown in (b,d) is 72 nm, which corresponds to 2.3 L_0 and 3.4 L_0 (L_0 is taken from qz spacing, 21.1 nm). AFM phase z-range is 16° for (a) and 9° for (b).

nm (3.4 L_0) shows a more defined cylindrical morphology, but the cylindrical segments are short and wavy (Figure 4-3b). Corresponding GISAXS patterns show a scattering ring around the specular peak (Figure 4-3c,d). The ring pattern can arise from tilted cylinders with random orientation, and/or grains of parallel cylinders with the (10) plane randomly oriented with respect to the substrate. The ring is elongated in the q_z direction which suggests uniaxial de-swelling of films during the final stage of the drying process.[37,39] Domain spacing based on vertical q_z peak from the specular position is calculated to be 21.1 nm which is 74 % of the horizontal domain spacing. A horizontal linecut of the 72 nm film at the specular q_z value shows two peaks with 1:√3 ratio with the first peak being more intense than the second peak (Figure 4-4g). This result coincides with the simulated GISAXS pattern for hexagonal cylinders randomly oriented along the cylinder axis.[40] Islands/holes structures are not observed in these films.

Although the brighter block in AFM phase image often corresponds to a mechanically harder block, the phase contrast in these images is thought to be inverted[41] such that the brighter domain represents a polymer-rich domain that forms the core of cylinders, while the darker domain represents a mCherry-rich domain forming matrix. From a geometric consideration based on the previous observations that mCherry prefers a bilayer formation[6] and unfavors the formation of core of cylinder,[42] it can be concluded that the domain with a width approximately 2/3 of the intercylinder spacing is polymer-rich and the domain with a width approximately 1/3 of intercylinder spacing is protein-rich. The fact that the brighter domains in phase images appear lower in a height image supports softness of this block.

When films are forced to dry slowly in a chamber where the relative humidity is maintained at 80% (RH80), cylindrical nanostructures oriented parallel to the substrate with preferred cylinder arrangement along the cylinder axis are observed (Figure 4-4). Bioconjugate films with thickness 55 ± 2 nm (2.9 L_0), 89 ± 3 nm (4.9 L_0), and 171 ± 6 nm (9.1 L_0) show cylinders oriented parallel to the substrate with a similar degree of ordering in AFM phase images (where L_0 is 18.8 nm calculated from the q_z spacing such that $L_0 = q_z/2\pi$). These films display islands/holes structures to accommodate incommensurability between the film thickness and the block copolymer domain spacing (Figure 4-10), except for the film corresponding to 9.1 L_0. The smooth surface observed for the film is attributable to the effects of the thickness of wetting layers on the overall film thickness measured by ellipsometry. Three peaks are indexed as (10), (11), and (21) in the GISAXS patterns (Figures 4-4d-f) based on the simulated GISAXS pattern of in-plane cylinders with their (10) plane aligned parallel to the substrate.[40] It has been previously reported that cylinder domain alignment with their (10) plane parallel to the substrate is energetically preferred.[43] The tilted peak for (10) in 171 nm film suggests the cylinder alignment is slightly more random compared to thinner films. The scattering vector length of the (10) peak, 0.0255 Å^{-1}, of the 89 nm-film calculated using the specularly reflected beam as the origin, corresponds to an inter-cylinder spacing of 28.4 nm, which is comparable to the inter-cylinder spacing of 27.8 nm the annealed bulk material.

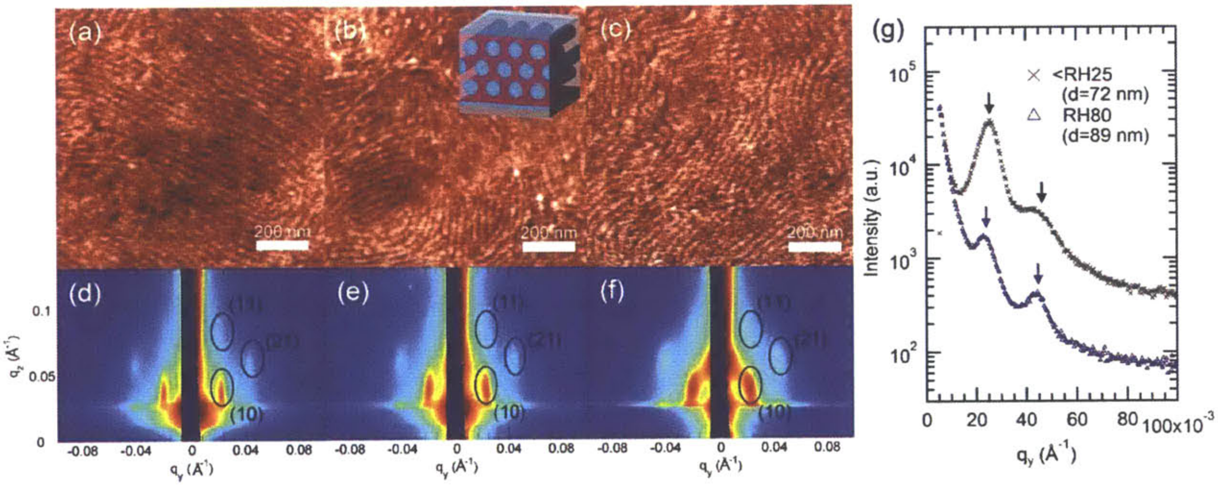

Figure 4-4. AFM phase images (top row) and corresponding GISAXS patterns (bottom row) measured at an incident angle 0.20° of mCherry-POEGA 26kDa bioconjugate films prepared at high relative humidity (RH 80). Thickness of films are measured to be (a)(d) 55 ± 2 nm (2.9 L_0), (b)(e) 89 ± 3 nm (4.8 L_0), and (c)(f) 171 ± 6 nm (9.1 L_0) using ellipsometry. The AFM phase z-range is 9°. Inset in (b): a proposed structure for a grain of the bioconjugate thin films. (g) Horizontal linecuts of representative films prepared under different humidity conditions. Black markers are from a 72-nm film prepared at 10% humidity and blue markers are from 89-nm film prepared at 80% humidity. The linecuts are obtained at q_z= 0.0244 Å^{-1} and q_z= 0.0266 Å^{-1}, respectively, from the GISAXS patterns at α_i=0.20°.

The q_z peak position in the GISAXS image shown in Figure 4-4f is measured to be 0.0335 $Å^{-1}$ which corresponds to a domain spacing 18.8 nm (or an inter-cylinder spacing 21.7 nm), which is 78% of the bulk domain spacing. The 18.8 nm is similar to the q_z-direction domain spacing measured from the GISAXS image shown in Figure 4-3d from a film prepared with fast evaporation. The much shorter z-direction domain spacing and the scattering patterns elongated in the q_z direction is characteristic of the anisotropic de-swelling.[37,39] This effect is later shown to be removed by solvent annealing. Horizontal linecuts of films prepared with slow evaporation show two peaks with 1:2 ratio, with the first peak from the q_y component of scattering from (10) planes and the second peak from the q_y component of scattering from (21) planes (Figure 4-4g).

Based in these results it is hypothesized that the film nanostructure consists of POEGA cylinders embedded in an mCherry matrix, with surface POEGA wetting layers on both film interfaces. This structure is schematically illustrated in the inset of Figure 4-4b. Although it is difficult to clearly identify which domain is forming cylinders from AFM images alone, a previous study on various coil fractions of mCherry-PNIPAM bioconjugate have shown that cylindrical structures with the mCherry core is prohibited even at polymer fraction as high as 0.82.[31] This observation suggests mCherry do not easily form an inward concave curvature while formation of outward concave structure is allowed. Because this conjugate forms cylindrical nanostructures with a POEGA core in the bulk also, the formation of an mCherry continuous phase in films is likely.

Aqueous solvent annealing does not significantly improve ordering in bioconjugate films, but does often lead to changes in domain spacing. Films are annealed in water vapor in a jar containing 0.5 M NaCl solution in order to lower the chemical potential of water to avoid de-wetting. GISAXS patterns of annealed films (Figure 4-11) show decreased q_z domain spacing, which suggests annealing decreases the initial anisotropy by swelling nanostructures in the z-direction. Thinner films prepared at <RH25 and RH80 show 164% and 138% increases, respectively, in domain spacing after annealing, both reaching hexagonal domain spacing of 31.5 nm in z-direction based on the peak in the vertical linecut from the specular position. The increase in domain spacing is less pronounced in thicker films. Despite the changes in domain spacing, films prepared at <25% relative humidity are not able to achieve the preferential cylinder alignment formed in films prepared in humidified condition, even after annealing for up to 40 hours. Annealing of films initially prepared at 80% relative humidity leads to only minor changes in peak ratios in horizontal linecuts and the appearance of a faint ring, suggesting alignment of the (10) plane relative to the substrate becomes more random as a result of annealing. The minimal effect of solvent annealing and evolution of more disordered structures are consistent with our previous observations that solvent annealing of bulk bioconjugate materials using water vapor only minimally increased ordering in previous studies due to a re-entrant order-disorder transition behavior of bioconjugates at high concentration.[28,42] Also, annealing of bioconjugate materials decreases activity of protein due to an additional hydration/dehydration step when a bulk material was tested; mCherry-POEGA 26 kDa material recovered 75% of its original bioconjugate activity when cast to a solid material and rehydrated,[30] while only 50% of activity is recovered when material was annealed in water vapor, dried, and rehydrated. This loss of function on processing emphasizes the importance of structural control directly during the initial film preparation step.

Interestingly, coating speed is found to affect long-range order. Higher coating speed generates a thicker film due to an increased frictional drag.[8] Films with similar thickness can be prepared at different coating speed by varying solution concentration. A 110 nm-thick film (5.9

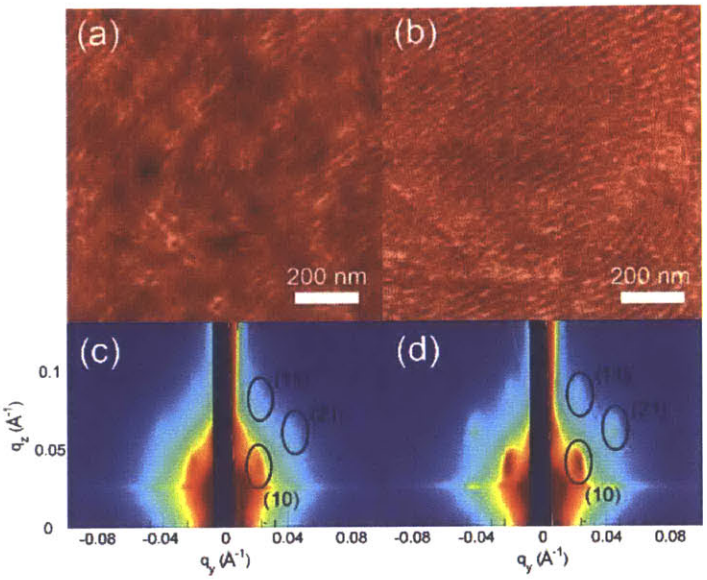

Figure 4-5. AFM phase images and GISAXS patterns of a 110 nm-thick film prepared at 2.5 mm/min from 25 wt.% solution (left), and AFM phase image and GISAXS pattern of a 104 nm-thick film prepared at 50 mm/min from 15 wt.% solution (right) at high relative humidity. GISAXS images are obtained at an incident angle 0.20° and the phase z-scale in (a) is 2° and (b) is 9°.

L_0) is prepared from 25 wt.% solution at 2.5 mm/min (Figure 4-5 a,c), and a 104 nm-thick film (5.5 L_0) is prepared from 15 wt.% solution at 50 mm/min (Figure 4-5 b,d), while films in Figure 4-3 and 4-4 are prepared at 15 mm/min at concentration 15-30 wt.% (L_0 = 18.8 nm). Comparison of AFM images and corresponding GISAXS patterns shows remarkable differences between the three films. The film coated at the highest speed demonstrates sharper peaks in the GISAXS pattern that are consistent with hexagonally packed cylinders ordered parallel to the substrate, while the film coated at the lowest speed shows weaker scattering for the 10, 11, and 21 peaks, which suggests less long-range order. This observation is consistent with AFM images of the upper film surfaces: the film coated at high speed shows a larger grain size composed of straighter cylinders, while the phase image of the film coated at low speed shows short segments of cylinders with considerably less order.

The difference in long-range order is unlikely to originate from flow-induced effects, as the Deborah number for the coating process is much less than 1.0 (shown in 4.4 Supplementary Information) and there is no consistent grain alignment relative to the coating direction (typical grain size of film shown in Figure 4-5b is an order of 0.5 - 1 μm based on AFM images). Presence of grains with multiple directions represented by typical fingerprint-like patterns suggests lack of correlation between the flow direction and cylinder orientation. Instead, the observed difference in grain size can be attributed to the nature of flow coating process. At the highest speed used, 50 mm/min, a wet film with large surface area is formed for a comparatively long distance behind the blade, while at the lower speeds the wet film area is relatively small. Nucleation of nanostructures starts at the surface where the solvent concentration drops below order-disorder transition concentration.[38] Slower coating allows a larger number of nucleation sites to form within a smaller area, which leads to smaller grain sizes and the observed difference in quality of order.

Fluorescence of bioconjugate films shows the presence of a threshold thickness near 20 nm (about one domain spacing) below which no functional protein is retained, followed by a linear increase of normalized fluorescence with increasing film thickness (Figure 4-6). Area under a fluorescence emission curve between 565 nm and 750 nm measured by spectrofluorometry (excitation wavelength: 550 nm) is normalized by the film thickness. Normalized fluorescence displays little dependence on processing conditions or degree of long range order. Instead, the occurrence of threshold thickness as well as the linear increase with increasing film thickness suggests a loss of fluorescent activity due to interactions with surfaces. A small but consistent blue shift in the maximum emission wavelength (610 nm)[44] is observed in films prepared at <RH25 as shown in the inset of Figures 4-12, which suggests that mCherry in films prepared with fast evaporation is slightly more perturbed.

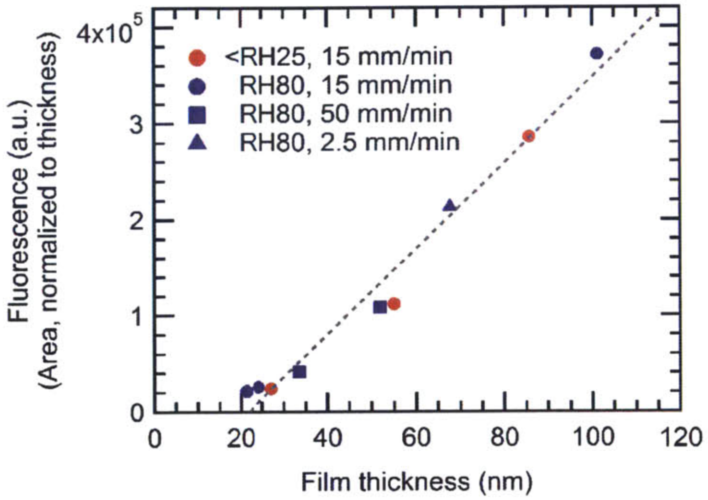

Figure 4-6. Fluorescence activity of mCherry-POEGA 26 kDa bioconjugate films. The y-axis represents fluorescence calculated from the area under emission curves between 565 nm and 750 nm followed by normalization to film thickness. Films are excited at wavelength 550 nm at 45° angle. The gray dotted line denotes a fitted result.

In conclusion, we demonstrate nanostructural control of protein-immobilized thin films with high density of proteins using bioconjugate block copolymer self-assembly. Long-range order of bioconjugates in thin films can be achieved by preparing films at high humidity and with high flow-coating speed, and control over the surface wetting conditions in the films enables the orientation of nanostructures to be controlled. Because the bioconjugate films preserve a high density of protein function, they can be used as a platform to design future protein-immobilized biomaterials.

4.4 Supplementary Information

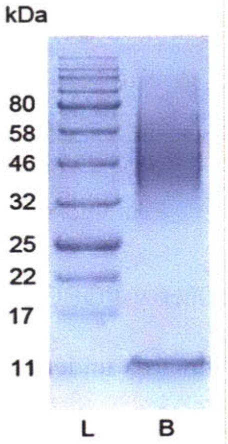

Figure 4-7. SDS-PAGE gel showing the molecular weight and purity of bioconjugate used in this study. L represents protein ladder and B represents bioconjugate sample. The average molecular weight of bioconjugate is 55 kDa and the small fragment represents a hydrolysis product due to boiling process.

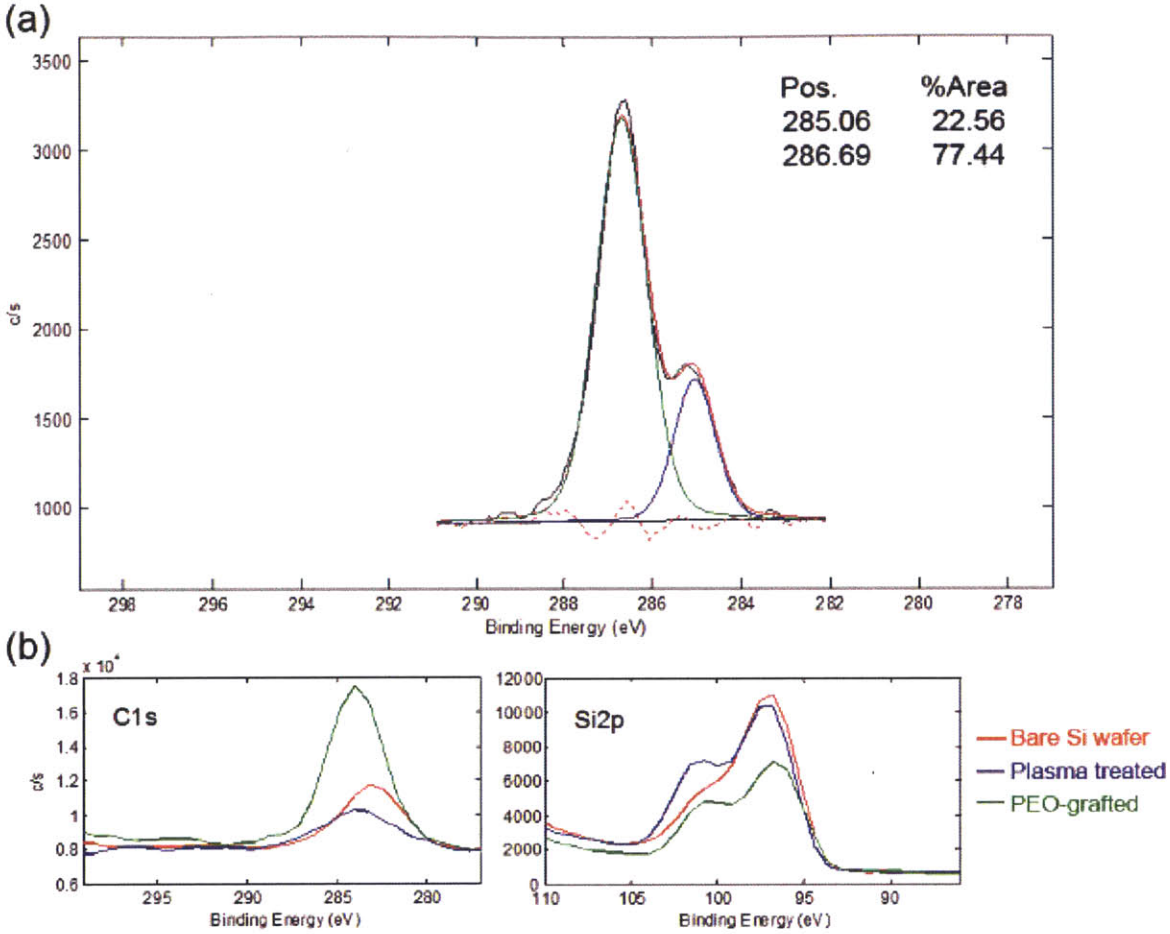

Figure 4-8. (a) A high-resolution XPS spectrum of C1s peak which is calibrated using Si2p as an internal standard. The major Si2p peak is calibrated to 99 eV. The solid red line is the fit to the experimental data (black) resulting from the summation of the blue (aliphatic carbon) and green (high energy carbon) lines. The dashed red line represents a residual between the experimental and the fit data. Peak positions and percent area from the best fit are indicated in the plot. (b) C1s and Si2p spectra zoomed in from a survey scan of bare silicon wafer (red curve), oxygen plasma treated silicon wafer (blue curve), and a PEO-grafted surface after oxygen plasma treatment (green curve), showing changes in relative content of the elements and their chemistry.

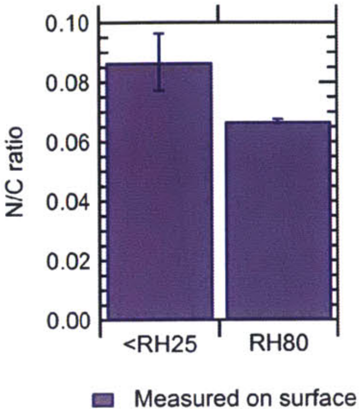

Figure 4-9. N/C ratio of mCherry-POEGA 26 kDa bioconjugate film surface prepared under different relative humidity conditions measured by X-ray photoelectron spectroscopy. Thickness of films are 54 and 42 nm for <RH25 and RH80 films, respectively. Three spots are measured to account for spatial variation within the film. (Student's *t*-test $P < 0.02$, statistically significant difference)

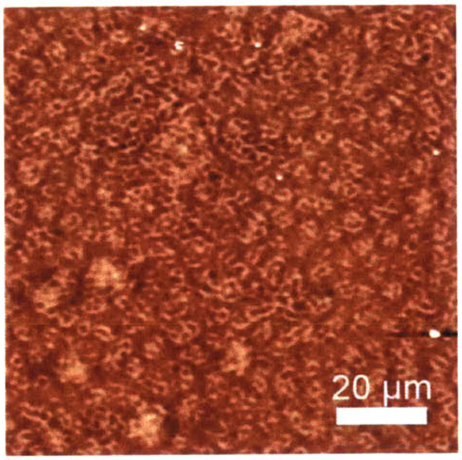

Figure 4-10. An AFM height image of a 64 nm-thick film (3.4 L_0) prepared at RH80 at a coating speed 15 mm/min showing islands/holes structure. The image was processed using 5th order 1-D line flattening. Z-scale is from 0 to 22 nm.

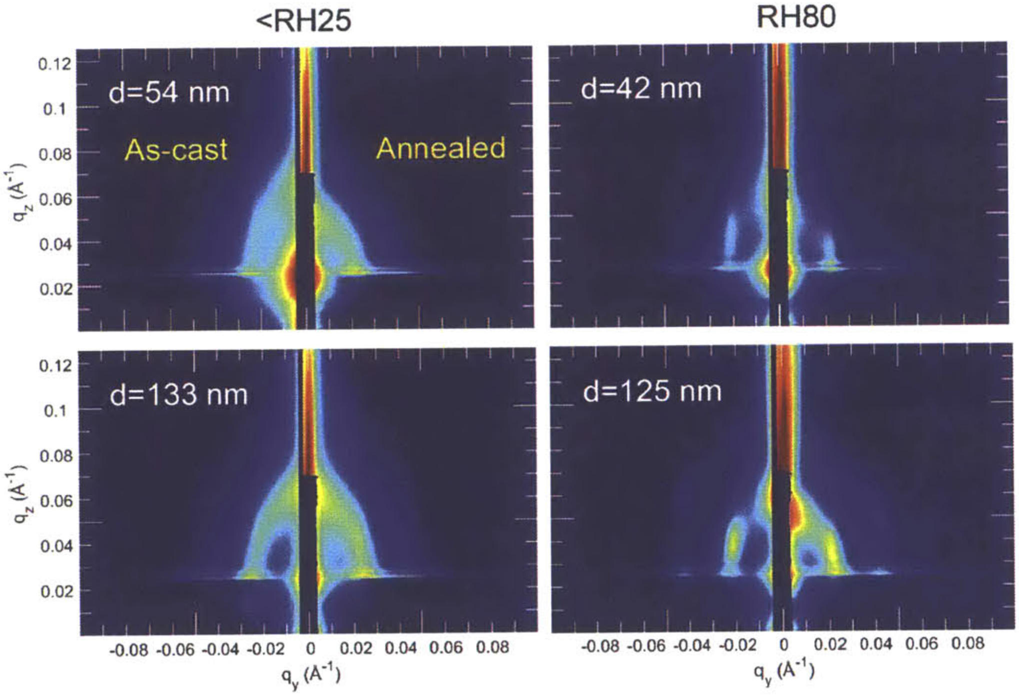

Figure 4-11. GISAXS patterns showing comparison of as-cast and annealed films. The left side of each image is from the as-cast films, and the right side of each image is from films annealed for 40 hours in a jar filled with 0.5 M NaCl solution. Thickness (d) is indicated in each images.

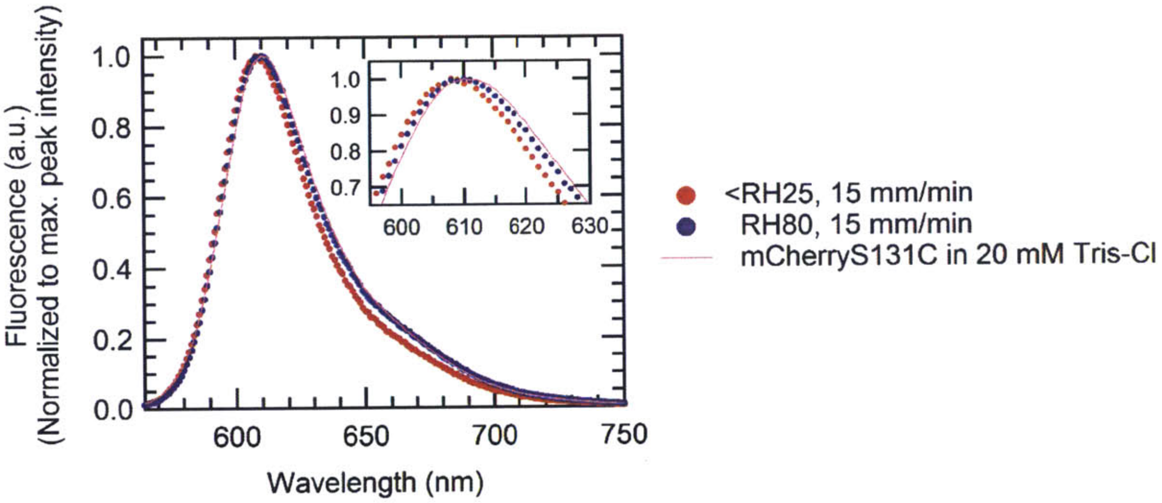

Figure 4-12. Example fluorescence emission spectra of films prepared at <RH25 and RH80 at 15 mm/min coating speed, with thickness 86 nm and 130 nm, respectively. The emission spectrum of mCherryS131C in 20 mM Tris-Cl buffer (pH 8.0) is shown in the pink-colored line, which overlaps closely with the RH80 film emission spectrum. Films are placed at a 45° angle to an incident light, and the fluorescence is measured using the front detector. mCherryS131C solution in a quartz cuvette is measured using the 90° angle detector. Raw signal intensities are corrected as described in method, and normalized to the maximum peak intensity for comparison.

Estimation of Deborah number (De)

De was estimated based on the Rouse model. Bioconjugate solutions with concentrations between 15 and 30 wt.% are assumed to be unentangled, dilute solutions and the molecular shape of bioconjugates is assumed as a sphere. The Rouse time, τ_R, is estimated using $\tau_R = \frac{\zeta}{k_B T} N R^2$ where $\zeta = 6\pi\eta R$ from Stoke's law (ζ: friction, N: number of monomers, η: viscosity of solvent, R: radius of the molecule, k_B: Boltzmann constant, T: temperature).

The viscosity of water (η) was estimated to be 1 cP. The radius of a bioconjugate molecule (R) was estimated from the radius of gyration of a similar molecule, mCherry-*b*-PNIPAM 29 kDa from a previous publication to be 7.5 nm.[28] The degree of polymerization for the POEGA 26 kDa polymer is 173 based on average monomer molecular weight and the N of the bioconjugate was estimated to be double of the degree of polymerization. From the values, Rouse time for the bioconjugate solution is estimated to be 6.7×10^{-4} s.

Three coating speeds at 2.5, 3 and 50 mm/min with a blade height 127 μm correspond to shear rate of 0.33, 1.97 and 6.56 s^{-1} which again correspond to experimental shear time scale of 3.1, 0.51, and 0.15 s. Comparison of the two time scales for three coating speeds confirms that relaxation of bioconjugate molecules occur in much shorter time scale than experimental time scale. De for the maximum coating speed is order of 4.4×10^{-3}.

4.5 References

(1) Chang, D.; Lam, C. N.; Tang, S.; Olsen, B. D. Effect of Polymer Chemistry on Globular Protein–polymer Block Copolymer Self-Assembly. *Polym. Chem.* **2014**, *5*, 4884–4895.

(2) Gross, L. A.; Baird, G. S.; Hoffman, R. C.; Baldridge, K. K.; Tsien, R. Y. The Structure of the Chromophore within DsRed, a Red Fluorescent Protein from Coral. *Proc. Natl. Acad. Sci. U. S. A.* **2000**, *97*, 11990–11995.

(3) Pakhomov, A. A.; Pletneva, N. V; Balashova, T. A.; Martynov, V. I. Structure and Reactivity of the Chromophore of a GFP-like Chromoprotein from Condylactis Gigantea.

Biochemistry **2006**, *45*, 7256–7264.

(4) Shu, X.; Shaner, N. C.; Yarbrough, C. A.; Tsien, R. Y.; Remington, S. J. Novel Chromophores and Buried Charges Control Color in mFruits. *Biochemistry* **2006**, *45*, 9639–9647.

(5) Chung, J. a.; Wollack, J. W.; Hovlid, M. L.; Okesli, A.; Chen, Y.; Mueller, J. D.; Distefano, M. D.; Taton, T. A. Purification of Prenylated Proteins by Affinity Chromatography on Cyclodextrin-Modified Agarose. *Anal. Biochem.* **2009**, *386*, 1–8.

(6) Thomas, C. S.; Glassman, M. J.; Olsen, B. D. Solid-State Nanostructured Materials from Self-Assembly of a Globular Protein-Polymer Diblock Copolymer. In *ACS Nano*; American Chemical Society, 2011; Vol. 5, pp. 5697–5707.

(7) Beamson, G.; Briggs, D. *High Resolution XPS of Organic Polymers: The Scienta ESCA300 Database*; Wiley, 1992.

(8) Stafford, C. M.; Roskov, K. E.; Epps, T. H.; Fasolka, M. J. Generating Thickness Gradients of Thin Polymer Films via Flow Coating. *Rev. Sci. Instrum.* **2006**, *77*, 1–7.

(9) Sheldon, R. a. Enzyme Immobilization: The Quest for Optimum Performance. *Adv. Synth. Catal.* **2007**, *349*, 1289–1307.

(10) Hoshi, T.; Anzai, J.; Osa, T. Controlled Deposition of Glucose Oxidase on Platinum Electrode Based on an Avidin/biotin System for the Regulation of Output Current of Glucose Sensors. *Anal. Chem.* **1995**, *67*, 770–774.

(11) Willner, I.; Katz, E. Integration of Layered Redox Proteins and Conductive Supports for Bioelectronic Applications. *Angew. Chemie Int. Ed.* **2000**, *39*, 1180–1218.

(12) Minteer, S. D. Enzyme Stabilization and Immobilization. *Methods Protoc. Ser. Methods Mol. Biol. 679Springer, Heidelb.* **2010**, *679*, 230.

(13) Nakanishi, K.; Sakiyama, T.; Imamura, K.; Of, A.; On, P.; Solid, T. H. E.; In, S.; Fields, V. On the Adsorption of Proteins on Solid Surfaces, a Common but Very Complicated Phenomenon. *J. Biosci. Bioeng.* **2001**, *91*, 233–244.

(14) Gidalevitz, D.; Huang, Z.; Rice, S. a. Protein Folding at the Air-Water Interface Studied with X-Ray Reflectivity. *Proc. Natl. Acad. Sci. U. S. A.* **1999**, *96*, 2608–2611.

(15) Postel, C.; Abillon, O.; Desbat, B. Structure and Denaturation of Adsorbed Lysozyme at the Air-Water Interface. *J. Colloid Interface Sci.* **2003**, *266*, 74–81.

(16) Cracknell, J. a.; Vincent, K. a.; Armstrong, F. a. Enzymes as Working or Inspirational Electrocatalysts for Fuel Cells and Electrolysis. *Chem. Rev.* **2008**, *108*, 2439–2461.

(17) Olsen, B. D. Self-Assembly of Globular-Protein-Containing Block Copolymers. *Macromol. Chem. Phys.* **2013**, *214*, 1659–1668.

(18) Christman, K. L.; Enriquez-Rios, V. D.; Maynard, H. D. Nanopatterning Proteins and Peptides. *Soft Matter* **2006**, *2*, 928–939.

(19) Ringeisen, B.; Callahan, J.; Wu, P.; Pique, A. Novel Laser-Based Deposition of Active Protein Thin Films. *Langmuir* **2001**, 3472–3479.

(20) Uematsu, I.; Matsumoto, H.; Morota, K.; Minagawa, M.; Tanioka, A.; Yamagata, Y.; Inoue, K. Surface Morphology and Biological Activity of Protein Thin Films Produced by Electrospray Deposition. *J. Colloid Interface Sci.* **2004**, *269*, 336–340.

(21) Lvov, Y.; Ariga, K.; Ichinose, I.; Kunitake, T. Assembly of Multicomponent Protein Films by Means of Electrostatic Layer-by-Layer Adsorption. *J. Am. Chem. Soc.* **1995**, *117*, 6117–6123.

(22) Lvov, Y. M.; Lu, Z. Q.; Schenkman, J. B.; Zu, X. L.; Rusling, J. F. Direct Electrochemistry of Myoglobin and Cytochrome p450(cam) in Alternate Layer-by-Layer

Films with DNA and Other Polyions. *J. Am. Chem. Soc.* **1998**, *120*, 4073–4080.

(23) He, J. A.; Samuelson, L.; Li, L.; Kumar, J.; Tripathy, S. K. Oriented Bacteriorhodopsin/polycation Multilayers by Electrostatic Layer-by-Layer Assembly. *Langmuir* **1998**, *14*, 1674–1679.

(24) Kim, B.; Lam, C. N.; Olsen, B. D. Nanopatterned Protein Films Directed by Ionic Complexation with Water-Soluble Diblock Copolymers. *Macromolecules* **2012**, *45*, 4572–4580.

(25) Laible, P. D.; Kelley, R. F.; Wasielewski, M. R.; Firestone, M. A. Electron-Transfer Dynamics of Photosynthetic Reaction Centers in Thermoresponsive Soft Materials. *J. Phys. Chem. B* **2005**, *109*, 23679–23686.

(26) Cardoso, M. B.; Smolensky, D.; Heller, W. T.; Hong, K. L.; O'Neill, H. Supramolecular Assembly of Biohybrid Photoconversion Systems. *Energy Environ. Sci.* **2011**, *4*, 181–188.

(27) Presley, A. D.; Chang, J. J.; Xu, T. Directed Co-Assembly of Heme Proteins with Amphiphilic Block Copolymers toward Functional Biomolecular Materials. *Soft Matter* **2011**, *7*, 172–179.

(28) Thomas, C. S.; Xu, L.; Olsen, B. D. Kinetically Controlled Nanostructure Formation in Self-Assembled Globular Protein–Polymer Diblock Copolymers. *Biomacromolecules* **2012**, *13*, 2781–2792.

(29) Lam, C. N.; Olsen, B. D. Phase Transitions in Concentrated Solution Self-Assembly of Globular Protein–polymer Block Copolymers. *Soft Matter* **2013**, *9*, 2393.

(30) Chang, D.; Lam, C. N.; Tang, S.; Olsen, B. D. Effect of Polymer Chemistry on Globular Protein-Polymer Block Copolymer Self-Assembly. *Submitted* **2014**.

(31) Fasolka, M. J.; Mayes, A. M. Block Copolymer Thin Films: Physics and Applications. *Annu. Rev. Mater. Res.* **2001**, *31*, 323–355.

(32) Albert, J. N. L.; Epps, T. H. Self-Assembly of Block Copolymer Thin Films. *Mater. Today* **2010**, *13*, 24–33.

(33) Jonas, A.; Kiraz, A. In Vitro and in Vivo Biolasing of Fluorescent Proteins Suspended in Liquid Microdroplet Cavities. *Lab Chip* **2014**, 3093–3100.

(34) Gather, M. C.; Yun, S. H. Bio-Optimized Energy Transfer in Densely Packed Fluorescent Protein Enables near-Maximal Luminescence and Solid-State Lasers. *Nat. Commun.* **2014**, *5*, 5722.

(35) Makievski, A. V.; Loglio, G.; Krägel, J.; Miller, R.; Fainerman, V. B.; Neumann, A. W. Adsorption of Protein Layers at the Water/Air Interface As Studied by Axisymmetric Drop and Bubble Shape Analysis. *J. Phys. Chem. B* **1999**, *103*, 9557–9561.

(36) Turturro, A.; Gattiglia, E.; Vacca, P.; Viola, G. T. Free Surface Morphology of Block Copolymers: 1. Styrene-Butadiene Diblock Copolymers. *Polymer (Guildf).* **1995**, *36*, 3987–3996.

(37) Kim, G.; Libera, M. Morphological Development in Solvent-Cast Polystyrene - Polybutadiene - Polystyrene (SBS) Triblock Copolymer Thin Films. *Macromolecules* **1998**, *31*, 2569–2577.

(38) Phillip, W. A.; Hillmyer, M. A.; Cussler, E. L. Cylinder Orientation Mechanism in Block Copolymer Thin Films upon Solvent Evaporation. *Macromolecules* **2010**, *43*, 7763–7770.

(39) Paik, M. Y.; Bosworth, J. K.; Smilges, D. M.; Schwartz, E. L.; Andre, X.; Ober, C. K. Reversible Morphology Control in Block Copolymer Films via Solvent Vapor Processing: An in Situ GISAXS Study. *Macromolecules* **2010**, *43*, 4253–4260.

(40) Lee, B.; Park, I.; Yoon, J.; Park, S.; Kim, J.; Kim, K. W.; Chang, T.; Ree, M. Structural

Analysis of Block Copolymer Thin Films with Grazing Incidence Small-Angle X-Ray Scattering. *Macromolecules* **2005**, *38*, 4311–4323.

(41) Haugstad, G. *Atomic Force Microscopy: Understanding Basic Modes and Advanced Applications*; Wiley, 2012.

(42) Thomas, C. S.; Olsen, B. D. Coil Fraction-Dependent Phase Behaviour of a Model Globular Protein–polymer Diblock Copolymer. *Soft Matter* **2014**, *10*, 3093–3102.

(43) Wang, Q.; Nealey, P. F.; De Pablo, J. J. Monte Carlo Simulations of Asymmetric Diblock Copolymer Thin Films Confined between Two Homogeneous Surfaces. *Macromolecules* **2001**, *34*, 3458–3470.

(44) Shaner, N. C.; Campbell, R. E.; Steinbach, P. A.; Giepmans, B. N. G.; Palmer, A. E.; Tsien, R. Y. Improved Monomeric Red, Orange and Yellow Fluorescent Proteins Derived from Discosoma Sp. Red Fluorescent Protein. *Nat. Biotechnol.* **2004**, *22*, 1567–1572.

Chapter 5. Self-Assembly of Protein-Zwitterionic Polymer Bioconjugates into Nanostructured Materials

5.1 Abstract

The microphase separation of a bioconjugate made of a globuar protein and a zwitterionic polymer is studied in order to elucidate the role of electrostatic interactions on the self-assembly of protein-polymer bioconjugates. Zwitterionic polymer surfaces are resistant to nonspecific protein adsoprtion due to strong hydration; however, bioconjugates constructed from a red fluorescent protein, mCherry, and a zwitterionic polymer, PDMAPS, show a relatively narrow range of conditions for self-assembly in concentrated systems. The bioconjugates demonstrate weaker segregation strengths compared to previously studied mCherry-polymer conjugates with non-ionic polymers, as demonstrated by higher order-disorder concentrations (C_{ODT}) and narrower range of ordered concentrations in the phase diagram. The results suggest that the protein-repulsive character of zwitterionic polymer is outweighed by electrostatic interactions. Electrostatic segregation of mCherry, which is found to be one of the main parameters governing the self-assembly of protein-nonionic polymer bioconjugates, is perturbed by zwitterionic polymer. Disruption of ordering upong addition of NaCl confirms that electrostatics play a critical role in the bioconjugate self-assembly. Order-disorder-order transitions are observed with increasing concentration of a kosmotropic salt, ammonium sulfate, due to the initial salt-in followed by salt-out effect, suggesting that stabilization of protein domains by enhancing attractive interactions between proteins can significantly improve long range ordering.

5.2 Introduction

The ability of enzymes to catalyse reactions that cannot be easily performed using alternate methods, high specificity towards a target molecule, regio- and stereospecificity, and the mild reaction conditions—temperature, pressure, and mild solvents—make them ideal catalysts. As a result, enzymes are studied as critical components of devices such as biosensors,[1,2] biofuel cells,[3,4] hyrogen fuel cell electrodes,[5] light harvesting materials,[6] and decontamination material for chemical warfare agents.[7,8] Self-assembly of protein-polymer bioconjugates represents a promising new approach to nanopattern proteins in these materials, potentially improving their performance.[9] The self-assembled materials have a very high density of proteins, approximately half of total material mass depending on the size of protein and polymer. The formation of nanostructures provides continuous transport pathways for substrates, products, cofactors, and/or charges, as well as control of protein orientation along the domain interfaces. Potential added advantages include improved stability and longevity of proteins and the low cost of nanopatterning 3-D materials by bottom-up approaches.[9,10]

Understanding the equilibrium phase behaviour in concentrated solution is important to control the type of nanostructure formed in the materials regardless of processing pathways.[11,12] Previous studies from our group on a bioconjugate of a red fluorescent protein, mCherry, and various synthetic homopolymers show that mCherry-polymer conjugates undergo microphase separation in concentrated aqueous solution to form nanostructures such as lamellae, hexagonally packed cylinders, perforated lamellae, or a double gyroid due to solvent-mediated net repulsive interactions.[12,13] Due to the heterogeneous monomer composition, globular and rigid shape, and anisotropic interactions of globular proteins, the phase behaviour is significantly different than that of traditional coil block copolymers.[14] It is hypothesized that the net repulsive interactions between protein and polymer are governed by multiple factors including hydration of protein and polymer, hydrogen bonding interactions, the shape of protein, and attractive electrostatic interactions between proteins.[12,13,15,16]

Zwitterionic polymers have attracted a great deal of attention for their strongly protein-repulsive nature in solution, and they are promising materials for antifouling coatings,[17–20] water filtration membranes,[21–24] and biomedical applications.[25,26] Side chains of zwitterionic polymers are structurally similar to naturally occurring osmolytes,[27] and protein-resistant surfaces are thought to be related to a display of kosmotropes with the tendency to exclude themselves from a protein surface in solution.[28] The mechanism of low protein adsorption is suggested to be related to the strong hydration of the polymers.[27] Recent simulation and experimental studies show that zwitterionic polymers are more strongly hydrated compared to poly(ethylene glycol) (PEG),[29] and the presence of hydration layers between the polymers and proteins is suggested as the reason for their protein-repulsive character.[30,31]

The protein-repulsive nature of zwitterionic polymers in dilute solution suggests that they would have a strong propensity to phase separate from proteins, potentially yielding bioconjugates that microphase separate over a wider range of compositions than other conjugates. However, in a concentrated aqueous solution, polymer chains are crowded to the point where the hydration shells of proteins are overlapping.[32] Hydration of the polymer block and globular protein is expected to be significantly different as the number of available water molecules per protein or polymer decreases as bioconjugate concentration increases. As a result, interactions between polymer blocks and proteins can change from those in dilute solution.

There is also evidence to suggest that a bioconjugate made of protein and zwitterionic polymer would display weaker segregation. Literatures has shown microphase separation arising from electrostatic segregation in ionomers[33,34] and charged-neutral diblock copolymers.[35–41] In our previous studies on bioconjugates made of mCherry and a non-ionic polymer block, it is possible that electrostatic segregation of protein block from the non-ionic polymer block contributes significantly to the driving force for microphase separation. This hypothesis is supported by a recent study showing that increasing ionic strength can lead to a reduction in the quality of order in bioconjugates with non-ionic polymer blocks.[15] Therefore, introduction of a zwitterionic polymer block may perturb the attractive electrostatic interactions between mCherry, thus supressing microphase separation.

In order to test these competing hypotheses, the self-assembly of a protein-polymer bioconjugate with a zwitterionic block, mCherry-poly(3-[*N*-(2-methacroyloyethyl)-*N*,*N*-dimethylammonio]propane sulfonate) (PDMAPS) is studied herein. PDMAPS, also known as poly(sulfobetaine methacrylate) (PSBMA), is a sulfobetaine polymer that displays upper critical solution temperature (UCST) behaviour depending on the molar masses, providing thermally tunable interactions in water, and its hydration has very little dependence on pH. mCherry is chosen as a model protein to represent a globular protein and provide a direct comparison with comparable bioconjguate self-assemblies prepared using non-ionic polymer blocks. Self-assembly of the zwitterionic conjugate is investigated in concentrated solution, illustrating the effect of this polymer on the ability of globular proteins to self-assemble. Studies are also performed with varying salt concentration, clearly elucidating the role of electrostatic interactions on the observed behaviour in these zwitterionic systems.

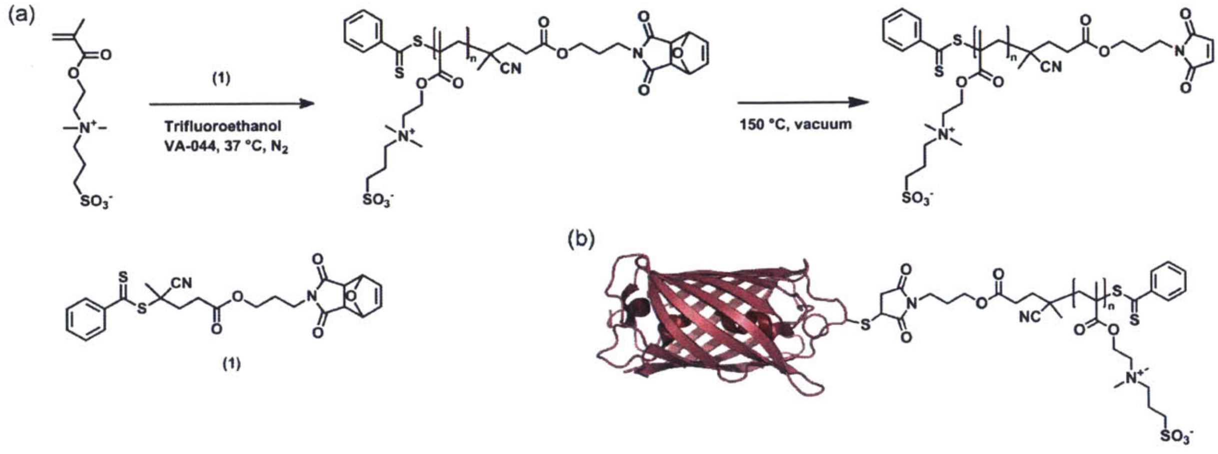

Scheme 5-1. Synthesis of mCherry-*b*-PDMAPS bioconjugates. (a) RAFT polymerization of PDMAPS using a RAFT agent (1) followed by a deprotection. (b) Structure of the final bioconjugates.

5.3 Experimental Methods

Synthesis and characterization of PDMAPS homopolymers

Synthesis of RAFT agent (1). 1.5 g of 4-cyano-4-(phenylcarbonothioylthio)pentanoic acid (CPP) (5.37 mmol, 1 equiv.), 1.36 g of imide (5.91 mmol, 1.1 equiv.) and 67.4 mg of 4-dimethylaminopyridine (DMAP) (0.54 mmol, 0.1 equiv.) were dissolved in 50 ml of dichloromethane. 1.37 g of *N*,*N*′-dicyclohexylcarbodiimide (DCC) (6.44 mmol, 1.2 equiv.) was added to the mixture and stirred under nitrogen overnight. The reaction mixture was washed using water three times, dried under anhydrous sodium sulfate, and concentrated by rotary evaporation. The crude product was further purified using an Isolera One Biotage system with A KP-Sil 50 g cartridge with hexane and ethyl acetate as eluents. 1.5 g of red oil was obtained after drying (yield: 73%). ^{1}H-NMR spectrum of the purified product (Figure 5-6) was recorded on a Bruker 400 MHz spectrometer.

RAFT polymerization and deprotection of PDMAPS. 3-[*N*-(2-methacroyloyethyl)-*N*,*N*-dimethylammonio]propane sulfonate (DMAPS), a chain transfer agent (1), and initiator VA-044 were dissolved in 84 mL of trifluoroethanol. After three freeze-pump-thaw cycles, the flask was filled with nitrogen and heated to 37 °C to initiate polymerization. Polymerization was conducted overnight and terminated by opening the flask to the air. The mixture was precipitated once in acetone and twice in methanol to obtain a pink solid. The polymer was dried in vacuum and deprotected at 150 °C under vacuum overnight. The molar mass and dispersity of the polymer were analysed by gel permeation chromatography using an Agilent Technologies 1260 Infinity system with two Aquagel columns in 0.5 M NaCl (aq) with 0.02% sodium azide as the mobile phase. The signals were collected from a Wyatt DAWN HELEOS II multi-angle light scattering detector and a Wyatt Optilab T-rEX refractometer. Dn/dc value of PDMAPS in 0.5 M NaCl solution was measured using a built-in method; an experimentally determined value of 0.1423 ± 0.0024 mL/g (Figure 5-7a) was used to obtain absolute molar masses. GPC spectra of two PDMAPS homopolymers are shown in Figure 5-7b, and a ^{1}H-NMR spectrum is shown in Figure 5-8. PDMAPS average molar masses (M_n) and dispersities ($Đ$) are listed in Table 5-1.

Cloud point measurement. Cloud points of the polymers and bioconjugates were determined by measuring the transmittance of 10 mg/mL polymer solutions or 10 mg/mL bioconjugate solutions in deionized water at 700 nm using UV-vis spectrometry. The solutions were first cooled and heated back at 0.2 °C per minute. The temperature at which a 10% drop in the initial transmittance is observed in the first cooling step was recorded as the cloud point according to reported methods in the literature.[42] The solution was stirred during measurement to prevent precipitation. The cloud points of PDMAPS homopolymers ($T_{\mathrm{t,\ PDMAPS}}$) and bioconjugates ($T_{\mathrm{t,\ bioconjugates}}$) are listed in Table 5-1, and the corresponding transmittance curves are shown in Figures 5-9.

Table 5-1. Molecular properties of mCherry-PDMAPS bioconjugates.

Bioconjugates	**M_n of PDMAPS (kg/mol)**	**Dispersity (Đ) of PDMAPS (M_w/M_n)**	**$T_{\mathrm{t,\ PDMAPS}}$ [a] (°C)**	**M_n of bioconjugates (kg/mol)**	**ϕ_{PDMAPS} [b]**	**$T_{\mathrm{t,\ bioconjugates}}$ [a] (°C)**
mChPD33	32.8	1.097	27.5	61.0	0.54	7.5
mChPD77	76.5	1.105	39.5	104.7	0.72	25.4

[a] $T_{\mathrm{t,\ PDMAPS}}$ and $T_{\mathrm{t,bioconjugates}}$: thermal transition temperatures for PDMAPS homopolymers and bioconjugates, respectively.

[b] ϕ_{PDMAPS}: volume fraction of PDMAPS in bioconjugates, calculated based on mCherry density 1.35 g/cm^3 (ref. 15) and the polymer density measured to be 1.37 g/cm^3.

Density measurement. The density of PDMAPS was measured using two nonsolvents with known densities, dichloromethane (density 1.326 g/cm^3) and chloroform (density 1.4788 g/cm^3). The two solvents were mixed by volume and the final volume was measured using a graduated cylinder. The final density of mixture was calculated using the measured final volume and the known mass of both solvents added. PDMAPS solid dried in vacuum was finely ground using a mortar and pestle to minimize pores trapped in the solid that may result in underestimation of the density. PDMAPS powder was mixed with solvent mixtures and left undisturbed for a few hours to settle within the solvent. Density of PDMAPS was estimated to be 1.37 based on the result that the PDMAPS solid settled in the solvent mixture with density 1.363 but floated in the mixture with density 1.378.

Synthesis and characterization of mCherry-PDMAPS bioconjugates

Protein expression and bioconjugation. mCherryS131C was expressed and purified according to a previously described method.[10] Bioconjugation was performed by adding a 6-fold molar excess of polymer to mCherryS131C in 20 mM Tris 0.5 M NaCl solution (pH 8). Before the addition of polymer, the protein was pre-incubated with 10-fold molar excess of 3,3′,3″-phosphanetriyltripropanoic acid hydrochloride (TCEP·HCl) for 1 hour to reduce disulphide bonds. The reaction was allowed to proceed overnight at room temperature. The reaction mixture was purified by nickel affinity chromatography to remove unreacted polymers. The eluent containing free protein and bioconjugate was dialyzed into 10 mM Tris-Cl pH 7.0 buffer for FPLC purification. Bioconjugates were purified using a HiTrap Q HP 5 ml anionic exchange column,10 mM Tris-Cl pH 7.0 as buffer A and 10 mM Tris-Cl 0.5 M NaCl pH 7.0 as buffer B in an AKTA pure FPLC system. A slow gradient from 0 to 20% B was applied to elute proteins, followed by a fast gradient from 20 to 100% to elute bioconjugate as a broad peak. The purity of each fraction was analysed using a denaturing protein gel, and the appropriate fractions were collected and dialyzed into deionized water. A native protein gel, circular dichroism spectra, and UV-vis spectra of purified bioconjugates are shown in Figure 5-10, Figure 5-11, and Figure 5-12, respectively, confirming the purity and folded structure of the protein. The average molar masses of bioconjugates (M_n) and PDMAPS volume fractions (ϕ_{PDMAPS}) in the bioconjugates are listed in Table 5-1.

Sample processing. Sample preparation for nanostructure analysis was conducted as previously described.[13] Briefly, bioconjugate solutions were concentrated using centrifugal filters with a molecular weight cut-off (MWCO) of 10,000 kDa, concentrated solutions were cast on Teflon sheets, and conjugates were dried under a controlled vacuum ramp. Solid pellets were weighed, and deionized water was added to hydrate the pellets at a desired concentration which is indicated as wt.% = mass of pellets/mass of solution. Typically, the density of water was assumed to be 1 g/cm^3 and the volume was measured when added to pellets. When making bioconjugate solutions with NaCl or ammonium sulfate, the added mass of salt was not taken into account. For example, to make 50 wt.% bioconjugate solution with 250 mM final concentration of NaCl, 10 mg of bioconjugate was dissolved in a 10 μL of 500 mM NaCl solution.

Nanostructure Characterization. Small angle X-ray scattering (SAXS), birefringence measurements, and turbidimetry were performed as previously described.[12] SAXS experiments were conducted at the Stanford Synchrotron Radiation Lightsource (SSRL) beamline 1-5 (X-ray energy 8 keV) and the Advanced Photon Source (APS) beamline 12-ID-C,D (X-ray energy 12 keV). Samples were exposed to X-rays for 180-120 s at SSRL and 0.5 s at APS. Samples were initially equilibrated at 35 °C for 20 minutes and temperature was decreased to 5 °C in 5 °C intervals with 15 minutes of equilibration prior to measurement at each temperature.

5.4 Results and Discussion

Phase behavior in concentrated aqueous solution.

Despite the protein-repulsive character of zwitterionic polymers in dilute solution, concentrated solutions of mCherry-*b*-PDMAPS conjugates display relatively high order-disorder transition concentrations (C_{ODT}) and a very narrow ordered region, compared to previously studied mCherry-polymer conjugates.[12,13] As previously defined, the lowest concentration at which the conjugate shows ordering when both blocks are well solvated is identified as C_{ODT}. Samples with the narrow primary peak and higher order reflections in SAXS are considered to form ordered nanostructures.

mChPD33 with a polymer volume fraction (ϕ_{PDMAPS}) 0.54 remains disordered in solution up to 47 wt.% and forms an ordered nanostructure at 50 wt.% when analysed by SAXS (Figure 5-1a). The ordered structure is measured to be weakly birefringent and is consistent with a hexagonal lattice based on the 6 peaks with a $1: \sqrt{3}: \sqrt{4}: \sqrt{9}: \sqrt{12}: \sqrt{13}$ ratio in the SAXS curve (indicated with arrows in Figure 5-1a). While the hexagonal symmetry most often corresponds to hexagonally packed cylinders in block copolymers, the unusual relative intensities among peaks suggest that a more complex structure or an unusual volume ratio between the two nanodomains cannot be ruled out. Compared to previously studied mCherry-polymer conjugates which undergo an order-disorder transition somewhere between 30-43 wt.% in a nonselective solvent when polymer volume fraction is approximately 0.5, the C_{ODT} for mChPD33 of 50 wt.% is the highest among all bioconjugates as indicated in a plot of C_{ODT} vs. polymer volume fraction (Figure 5-2). The higher C_{ODT} suggests that the segregation strength between mCherry and PDMAPS may be weaker than previously studied mCherry-polymer conjugates.

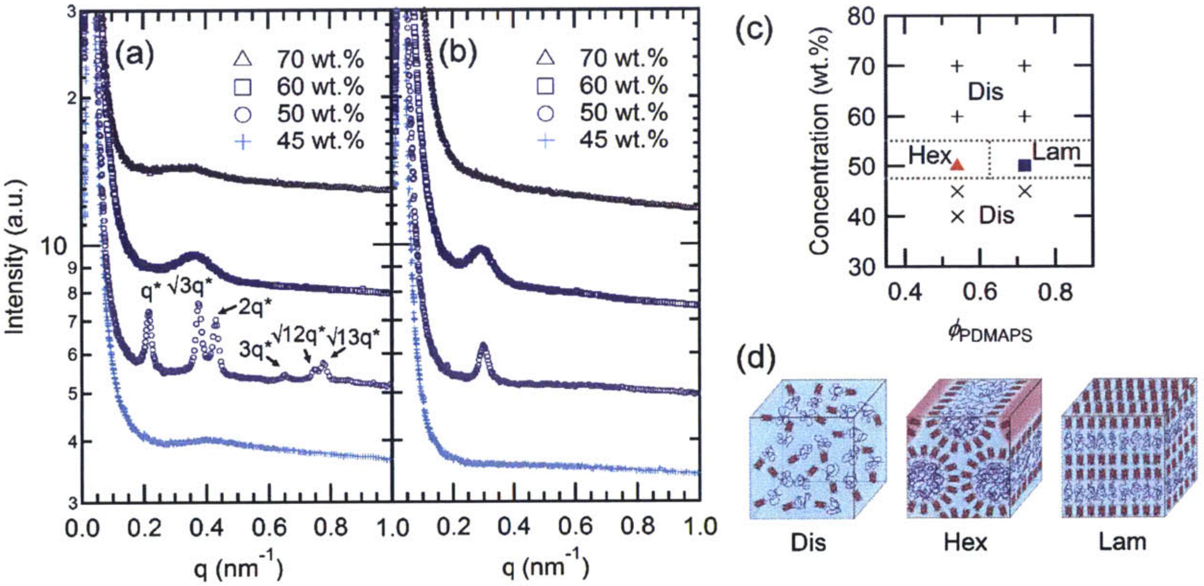

Figure 5-1. The phase behaviors of mCherry-*b*-PDMAPS bioconjugate with two polymer fractions. SAXS curves of conjugates with (a) ϕ_{PDMAPS} = 0.54 and (b) ϕ_{PDMAPS} = 0.72 are measured at 35 °C at which both protein and polymer blocks are well solvated. Curves are vertically offset for clarity. (c) Phase diagram of bioconjugate solutions measured at 35 °C as a function of coil fraction and solution concentration. Dis: a disordered phase, Hex: a hexagonally packed nanostructure, and Lam: a lamellar phase. (d) Schematics showing likely molecular arrangements in the nanostructures indicated in (c), adapted from reference 13.

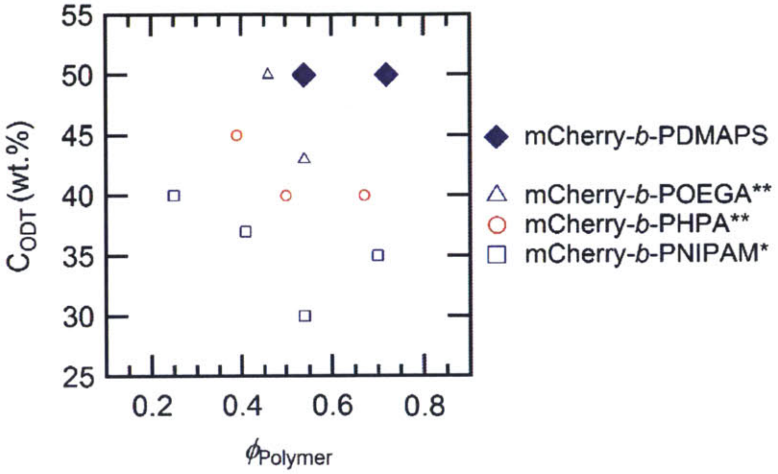

Figure 5-2. Order-disorder transition concentrations (C_{ODT}) of mCherry-polymer bioconjugates with different polymer block chemistry plotted as a function of polymer volume fraction. Open symbols represent previously values. Note that C_{ODT} of mCherry-*b*-PDMAPS at $\phi_{PDMAPS} = 0.72$ overlaps with that of mCherry-*b*-POEGA with ϕ_{POEGA}=0. 72. * from reference 12 ** from reference 13.

mChPD77 with $\phi_{PDMAPS} = 0.72$ also undergoes an order-disorder transition at 50 wt.%. The bioconjugate is not ordered up to a concentration of 45 wt.% based on SAXS, and it displays a narrow primary peak at 50 wt.% (Figure 5-1b). Despite the presence of a sharp primary peak, higher order reflections do not appear in SAXS. Another SAXS pattern obtained from a brighter X-ray source shows the presence of a broad second order peak approximately at 1:2 ratio to the primary peak (q*), suggesting a long-range order similar to a lamellar nanostructure (Figure 5-3b). It is possible that the secondary peak is suppressed due to the symmetry of the phase. A dramatic increase in birefringence as concentration changes from 45 to 50 wt.% further confirms the ordering transition. The strong birefringence intensity (Figure 5-3d) also supports a formation of an anisotropic phase.

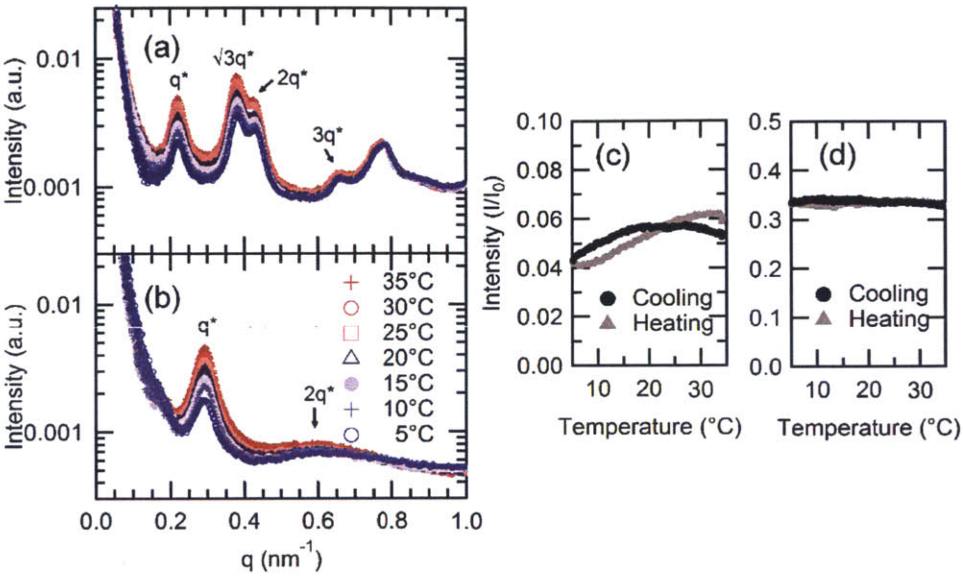

Figure 5-3. Temperature dependence of 50 wt.% solutions shown by SAXS and DPLS for (a) ϕ_{PDMAPS} = 0.54 and (b) ϕ_{PDMAPS} = 0.72. (Note this data were obtained at a different beamline, thus resulting in different resolution.) In birefringence measurement (c,d), the solution was first cooled and then heated.

Given the re-entrant disordering behaviour at high concentrations, both mCherry-*b*-PDMAPS conjugates display a very narrow ordered region in the phase diagram (Figure 5-1c). As concentration increases further from 50 wt.%, the conjugates display a re-entrant transition to a disordered phase which is labelled Dis in the phase diagram (Figure 5-1c). Previously studied mCherry-polymer conjugates also display the re-entrant disordering transition, but at high concentrations near 70-80 wt.%.[13,14] Also, in contrast to the high concentration disordered phases of mCherry-*b*-PHPA and mCherry-*b*-POEGA which were birefringent (suggesting a nematic liquid crystalline order),[13] 70 wt.% solutions of mChPD33 and mChPD77 are not birefringent, indicating there is no preferred orientation for mCherry molecules.

The bioconjugate phase behaviour show little dependence on temperature. The solvent quality for the PDMAPS block at a lower temperature is poorer due to the UCST behaviour as indicated in Table 5-1 and Figure 5-9. Compared to mChPD33 with a T_t of 7.5 °C, mChPD77 is expected to display a clearer structural transition within the temperature range studied from 35 to 5 °C due to a higher T_t of 25.4 °C. However, the ordering of both conjugates at 50 wt.% barely changes as shown by SAXS curves (Figure 5-3). SAXS peak intensities decrease while positions and widths of the peaks remain the same as temperature changes from 35 °C to 5 °C. Both structures are measured to be homogeneous throughout the temperature range, and the birefringence of mChPD33 shows only a slight decrease in intensity upon decreasing temperature (Figure 5-3c) while that of mChPD77 remains constant (Figure 5-3d). Decrease in SAXS peak intensity can be explained by decrease in X-ray scattering contrast between a polymer-rich and protein-rich domains as the water distribution between domains changes. It is expected that water is re-distributed from PDMAPS-rich domains to mCherry-rich domains as temperature decreases. Based on estimated X-ray scattering length density of mCherry, PDMAPS, and water (Table 5-2), scattering contrast is minimized when 58% of water is distributed in PDMAPS domains and 42% of water is distributed in mCherry domains (Figure 5-13). The fact that scattering contrast decreases as water is re-distributed to mCherry domains at low temperature suggests that originally at 35 °C the polymer domain is more hydrated than the mCherry domain is; more than 58% of water is hydrating PDMAPS domain.

Domain spacing of mChPD77 is significantly smaller than those of mChPD33 and previously studied mCherry-polymer conjugates with a similar coil fraction. Domain spacings are calculated from the location of the primary peak in SAXS curves ($d=2\pi/q^*$). The domain spacing of mChPD33 is measured to be 29.7 nm which is comparable to the 26 - 27 nm measured for hexagonally packed cylinders made of mCherry-polymer conjugates with similar coil fraction in solution.[13] However, the domain spacing of mChPD77 in 50 wt.% solution, 21.1 nm, is significantly smaller than lamellar spacings of previously studied mCherry-polymer conjugates with similar coil fractions; 50 wt.% solution of mCherry-polymer conjugates with polymer molar mass approximately 57 kg/mol and coil fraction 0.7 demonstrate well-defined primary and secondary peaks in SAXS with 1:2 ratio, and their lamellar spacings are measured to be 30 - 37 nm at 5 - 10 °C when both blocks are well solvated.[12,13] The substantially smaller domain spacing of mChPD77 than those of mChPD33 and bioconjugates with a similar coil fraction, despite the larger polymer size, suggests a weaker segregation strength which is reminiscent of the highly asymmetric nature of phase diagrams of charged block copolymers.[43,44]

Figure 5-2 summarizes the C_{ODT} values obtained in all mCherry-polymer bioconjugates that have been studied. While previously studied conjugates undergo order-disorder transitions at 30-43 wt.%, mCherry-*b*-PDMAPS conjugates undergo the transition at 50 wt.%. The C_{ODT}s of mCherry-PDMAPS are higher or equal to those of all previously studied mCherry-polymer conjugates.[12,13] The range of ordered concentrations of the mCherry-*b*-PDMAPS conjugates, which is only 50 wt.% in the phase diagram, is substantially narrower than that of other bioconjugates with similar coil fractions, which is approximately 35-60 wt.%. The highest C_{ODT}s and the narrowest ordering range of the mCherry-PDMAPS conjugates suggest that the interactions between mCherry and PDMAPS are least repulsive among the conjugates.

Hydration, which is considered as a key mechanism for the protein-repulsive property of zwitterionic polymer surfaces, is expected to be somewhat limited in the concentrated solution conditions employed in this study. Estimation of hydration level of PDMAPS and mCherry shows that there may not be sufficient water molecules present to mediate repulsive interactions in this regime. If we assume that 50% of total water is distributed in polymer-rich domain in mChPD33, the number of water molecules available per PDMAPS monomer in the case of 50 wt.% solution is approximately 15. While this value is greater than the estimated maximum number of water molecules bound per monomer, 8,[29] it affords proteins an approximately 8 Å-thick hydration shell per mCherry (details of this estimation are shown in 5.6 Supplementary Information). The thickness of the first hydration shell of protein, which is denser than bulk water, is estimated to be 3 Å,[45,46] but recent simulation and experiments suggest that hydration shell extends out to 10 Å from the protein surface.[32] Thus, in this high concentration regime, the hydration shell of protein is likely to be overlapping with hydration shell of other proteins as well as being perturbed by polymers, which can reduce the effectiveness of these hydration layers in promoting protein-polymer repulsion.

Given that the mechanism for antifouling is ineffective, the reduced repulsion may be explained by theories of electrostatic segregation. Having charge asymmetry in a block copolymer can produce a driving force for self-assembly,[43,44] as has been observed in several examples of protonated block copolymers,[41] block copolymers that strongly bind salt,[35–39] sulfphonated block copolymers,[40] and ionomers.[47] Previously studied bioconjugates in our group are constructed from a protein and a non-ionic polymer chain,[10,12,13,15,16,48] in which a protein with a number of charged residues on the surface can act as multivalent charged species which affect local ordering arising from attractive Coulombic interactions, contributing significantly to the driving force for microphase separation. A highly ionic polymer block, PDMAPS, is able to perturb the electrostatic segregation of mCherry, dramatically reducing the window of molecular composition and solution concentration where ordered nanostructures are formed.

Effect of Electrostatic Interactions.

Addition of sodium chloride (NaCl) to an ordered mChPD33 solution induces disordering at very low levels by modulating the relative solubilities of the two blocks of the block copolymer. A 50 wt.% solution of mChPD33 becomes disordered upon addition of NaCl at a final concentration 25 mM as demonstrated by the appearance of a broad peak in the SAXS curve (Figure 5-4a). As the NaCl concentration further increases to 250 mM, the position of the broad peaks shift towards lower q, and the intensity of the peaks gradually increases, indicating an increase in the correlation length (Figure 5-14). mChPD33 solutions display a disordered state at concentrations between 50 and 70 wt.% in the presence of 250 mM NaCl (Figure 5-15). The fact that the ordering is disrupted in the presence of small amount of salt, approximately 0.15 wt.%, suggests that electrostatic interactions play a critical role in the self-assembly of mCherry-*b*-PDMAPS conjugates.

While addition of NaCl affects the solvent quality for both blocks, the improvement of solvent quality upon addition of 25 mM NaCl is greater for PDMAPS than for mCherry. mCherry is soluble in pure water at a concentration greater than 200 mg/mL, possibly due to the relatively stable β-barrel structure as well as its surface properties. However, it has been shown that solubility of PDMAPS increases rapidly in the low salt region.[49] The θ condition for a 0.1 wt.% solution of 440 kg/mol PDMAPS is 0.05% NaCl at 25 °C.[49] Attractive interactions between PDMAPS blocks will then play a significant role in the initial microphase separation in deionized water. The efficacy of the salt in modulating attractive interactions between PDMAPS blocks is further supported by the fact that the cloud point of 1 wt.% solution of PDMAPS 33 kg/mol is measured to be 13.6 °C in the presence of 25 mM NaCl, which is approximately 14 °C lower than the cloud point measured in pure water. The Debye length calculated at each NaCl concentration with or without mChPD33 bioconjugate is shown in Figure 5-16. As the mChPD33 50 wt.% bioconjugate solution have a very small Debye length even without salt, additional salt has a minimal effect on the range of electrostatic interactions.

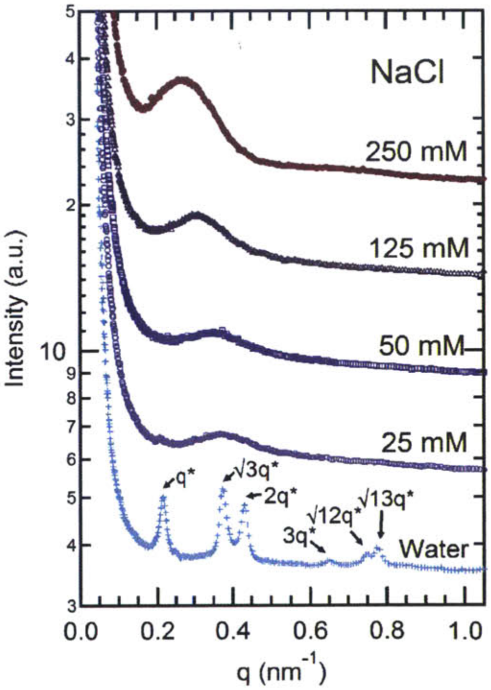

Figure 5-4. SAXS curves of (a) 50 wt.% and (b) 70 wt.% solutions of mChPD33 conjugate (ϕ_{PDMAPS} = 0.54) in the presence of various concentrations of sodium chloride. Curves are vertically offset for clarity.

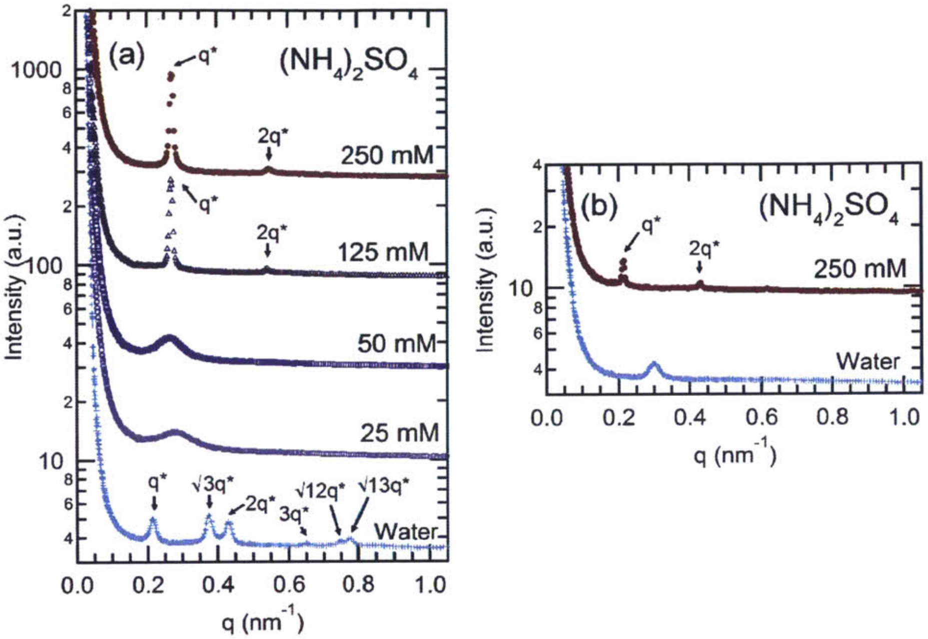

Figure 5-5. SAXS curves of 50 wt.% solution of (a) mChPD33 conjugates and (b) mChPD76 conjugates in the presence of ammonium sulfate at concentrations indicated in the plot. Curves are vertically offset for clarity.

The use of a strongly kosmotropic salt, ammonium sulfate ($(NH_4)_2SO_4$), produces disordering at low concentrations like NaCl but induces the formation of well-ordered phases at high concentrations. Ammonium sulfate is well-known for having a salting-out effect on proteins by increasing the effective attractive interactions between proteins.[50] Ammonium and sulfate ions are both located early in Hofmeister series.[51] Ammonium sulfate solution is a poorer solvent for mCherry than it is for PDMAPS due to the salting-out effect which promotes attractive interactions between proteins. A solubility study in 1 M ammonium sulfate solution (pH 8) shows that PDMAPS remains soluble at 50 mg/mL while protein precipitates at 10 mg/mL, even when ammonium sulfate solution is buffered to pH 8.0 to minimize the effect of decreased protein solubility near its pI (pH 6.2 for mCherry). Meanwhile, an ammonium sulfate solution is a better solvent for PDMAPS than pure water, but a poorer solvent compared to a NaCl solution with the same concentration.[52]

A 50 wt.% solution of mChPD33 first becomes disordered upon addition of 25 of $(NH_4)_2SO_4$ (Figure 5-5a). This disordering effect is similar to the effect of NaCl in that the added salt screens self-attractive electrostatic interactions that are responsible for microphase separation. Proteins typically salt in first as $(NH_4)_2SO_4$ concentration increases, and salt out at a high concentration of $(NH_4)_2SO_4$. The peak position of the 25 mM $(NH_4)_2SO_4$ solution is lower than that of 25 mM NaCl solution (Figure 5-14), which may suggest a greater segregation strength. As the concentration of $(NH_4)_2SO_4$ increases from 25 mM to 50 mM, the peak position shifts towards low q. This shift can be attributed to the increased segregation strength between mCherry and PDMAPS.

When the ammonium sulfate concentration reaches 125 mM, the nanostructure transitions to a lamellar structure indicated by the appearance of a sharp primary peak, q*, and a secondary reflection peak at 2q*. The lamellar phase is macrophase homogeneous as inferred from its bulk optical transparency and has no birefringence despite the sharp primary peak, which may arise from the small grain size. The disorder-to-order transition is expected to be caused mainly by increased attractive interactions between the proteins promoted by $(NH_4)_2SO_4$. The formation of a lamellar structure compared to the structure with an hexagonal symmetry in pure water can be attributed to the decreased effective volume fraction of proteins and increased volume fraction of polymers due to change in hydration.

Interestingly, mChPD76 conjugate solutions undergo a similar structural transition (Figure 5-5b). While 50 wt.% solution in water demonstrates a broad peak in SAXS, the solution transitions to a lamellar structure with much narrower primary and secondary peaks with a larger domain spacing. The lamellar spacing of 29.1 nm is greater than the 23.1 nm measured for 50 wt.% solutions of mChPD33 in the presence of 250 mM $(NH_4)_2SO_4$. The 29.1 nm spacing of mChPD77 also agrees better with the previously observed lamellar structures made of mCherry-polymer conjugates. The structural transition observed in SAXS suggests that attractive interactions of mCherry significantly contribute to long-range ordering.

5.5 Conclusion

The self-assembly of bioconjugates consisting of a red fluorescent protein, mCherry, and a zwitterionic polymer, PDMAPS, shows that despite the anti-fouling character of the polymer block, the bioconjuages have an extremely narrow range for phase separation in concentrated aqueous solutions. Both conjugates with polymer volume fraction (ϕ_{PDMAPS}) 0.54 and 0.70 undergo order-disorder transition at 50 wt.%, which is the highest concentration compared to previously studied mCherry-polymer conjugates. The conjugates show re-entrant disordering at a lower concentration, 60 wt.%, than other mCherry-polymer conjugates. The highest C_{ODT} as well as a very narrow range of ordered region in the phase diagram suggests weak segregation strength between mCherry and PDMAPS, and that the protein-repulsive property of PDMAPS in dilute solution does not translate to the self-assembly of mCherry-*b*-PDMAPS conjugates in a concentrated regime where polymer chains and hydration layers of proteins are highly overlapped. Comparison to previously studied mCherry-polymer conjugates with non-ionic polymer blocks suggests that electrostatic segregation of mCherry is one of the key factors driving the self-assembly; the ionic polymer block results in much weaker segregation in mCherry-*b*-PDMAPS than in previously studied systems.

Studies of salt also show that self-attractive electrostatic interactions are critical in the self-assembly. mChPD33 conjugate disorders upon addition of small amount of NaCl as the attractive interactions between PDMAPS are reduced at even low salt levels. Addition of ammonium sulphate, a salt located later in Hofmeister series, first disrupts the ordering at lower concentration (25-50 mM) due to the similar effect as NaCl salt. The solution then transitions to an ordered phase at higher concentration of ammonium sulphate (125 and 250 mM). The transitions suggest that enhanced attractive interactions between proteins improve long-range order of bioconjugate materials. This study elucidates the role of electrostatic segregation as one of the key mechanisms of the protein-polymer self-assembly, and demonstrates the interactions of salts with bioconjugates can disrupt or enhance the self-assembly.

5.6 Supplementary Information

Materials

3-[*N*-(2-methacroyloyethyl)-*N*,*N*-dimethylammonio]propane sulfonate (DMAPS) monomer (97%, CAS 3637-26-1) was purchased from Sigma-Aldrich. 4-cyano-4-(phenylcarbonothioylthio)pentanoic acid (CPP) (min. 97%) was purchased from Strem Chemicals. 2,2'-Azobis[2-(2-imidazolin-2-yl)propane]dihydrochloride (VA-044) was purchased from Wako Chemicals. Trifluoroethanol (ReagentPlus®, ≥99%) was purchased from Sigma-Aldrich. Deuterium oxide (D, 99.8%, sterility tested) was purchased from Cambridge Isotope Laboratories Inc. Other reagents were purchased from Sigma-Aldrich and used without further purification unless otherwise stated.

Calculations of the hydration of protein and polymer

The number of available water molecules per monomer of PDMAPS ($N_{H2O,DMAPS}$) can be obtained from equation 1, where w is the wt.% of bioconjugate in solution, $M_{n,BC}$ is the average molar mass of bioconjugate, DP is the degree of polymerization of PDMAPS, M_{H2O} is the molar mass of water (18.015 g/mol), and f is the fraction of water hydrating polymer domain. In the case of a 50 wt.% solution of mChPD33 ($M_{n,\,BC}$ 32,800 g/mol and DP 116) and the case of equal hydration ($f = 0.5$), $N_{H2O,DMAPS}$ is 14.6.

$$N_{H2O,DMAPS} = \frac{\frac{(1-w)}{M_{H2O}} f}{\frac{w}{M_{n,BC}} DP} \qquad (1)$$

Similarly, the average number of available water molecules per mCherry molecule ($N_{H2O,mCherry}$) is obtained from the equation 2. 1,691 molecules of water are available for mCherry, which using the bulk density of water of 18.015 g/cm^3 would occupy a volume (V_H) 59.6 nm^3, in the case of mChPD33 and equal hydration between PDMAPS and mCherry domain. The average thickness of the hydration shell of the protein is estimated as a cylindrical shell with this volume. mCherry is assumed to be a cylinder with a length (l) 4.4 nm and radius (R) 1.25 nm based on the crystal structure (PDB 2H5Q).[53] The volume of a hydration layer of mCherry (V_H) with thickness d is given by $V_H = \pi(R + d)^2(l + 2d) - \pi R^2 l$, in which d can be determined based on the V_H obtained above. d is estimated to be 0.84 nm.

$$N_{H2O,mCherry} = \frac{\frac{(1-w)}{M_{H2O}}(1-f)}{\frac{w}{M_{n,BC}}} \qquad (2)$$

Calculation of Debye lengths.

The Debye lengths (κ^{-1}) of salt solutions with various concentration of NaCl and $(NH_4)_2SO_4$ are calculated based on the equation shown below.

$$\kappa^{-1} = \sqrt{\frac{\varepsilon_0 \varepsilon_r k_B T}{\sum \rho_{\infty,i} e^2 z_i^2}} \qquad (3)$$

where ε_0 is vacuum permittivity, ε_r is relative permittivity, k_B is Boltzmann constant, T is temperature in Kelvin, i represents each ionic species, ρ is the number density [m^{-3}], e is the elementary charge, and z is the charge number.

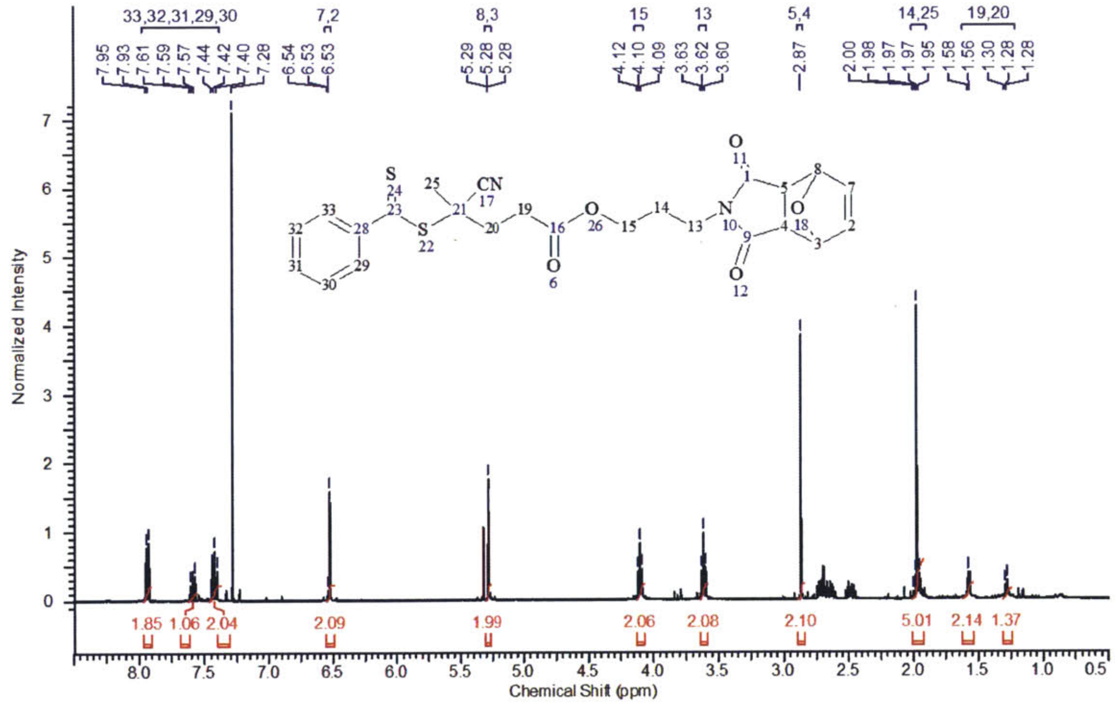

Figure 5-6. H^1-NMR spectrum of CPP-imide in $CDCl_3$ solution.

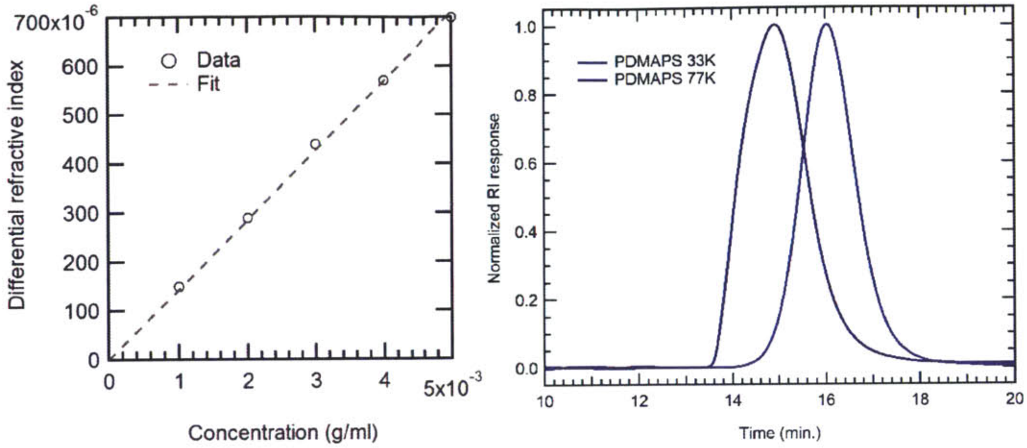

Figure 5-7. Characterization of PDMAPS. (a) Plot of differential refractive index of PDMAPS. dn/dc value is measured using a built-in batch mode software provided by Wyatt Technology. 1,2,3,4, and 5 mg/mL of polymer solutions were prepared in 0.5 M NaCl solution. The dn/dc was measured to be of 0.1423 ± 0.0024 mL/g (R^2=0.9979). (b) GPC trace of PDMAPS used in this study.

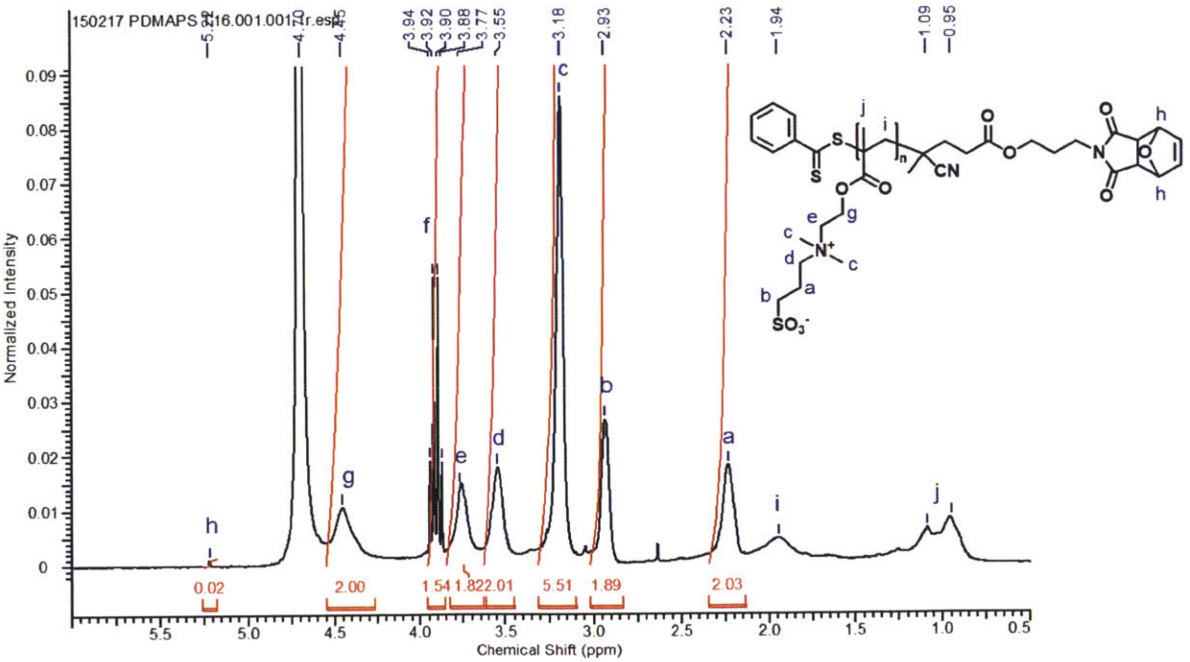

Figure 5-8. ^{1}H-NMR spectrum of PDMAPS with M_n 32,880 g/mol dissolved in D_2O.

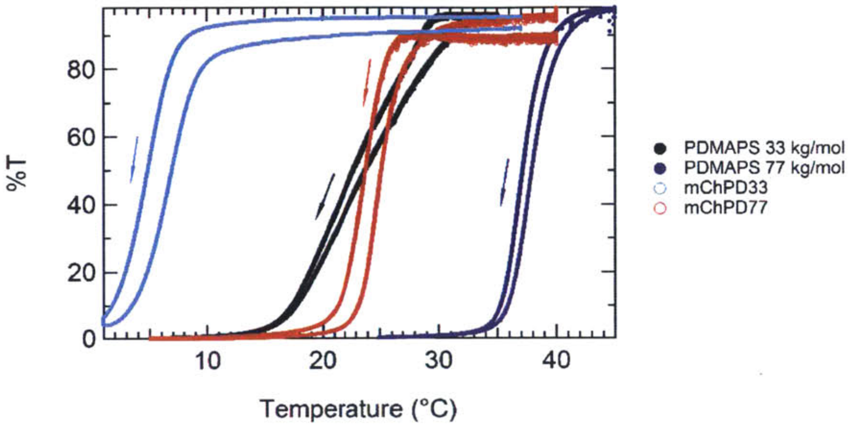

Figure 5-9. Thermal transition of PDMAPS homopolymers and corresponding bioconjugates. 10 mg/mL polymer solution in Milli-Q water was cooled down first and heated. Cooling traces are marked with arrows pointing downwards. The differences between cloud point measured from 10% reduction in transmittance and that from 50% reduction are 12.3, 1.8, 2.8, and 1.8 °C for PDMAPS 33 kg/mol, PDMAPS 77 kgm/mol, mChPD33, and mChPD77, respectively, which represents the breadth of their thermal transitions. The broad transition of PDMAPS 33 kg/mol homopolymer is thought to be due to kinetic effects, as the slope changes with a ramp rate.

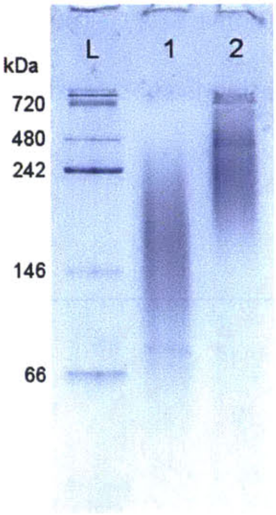

Figure 5-10. Native gel of purified products. Lane L, lane 1, and lane 2 represent protein ladder, mChPD33 conjugate, and mChPD77 conjugate, respectively. Lanes between the ladder and bioconjugates are omitted for clarity.

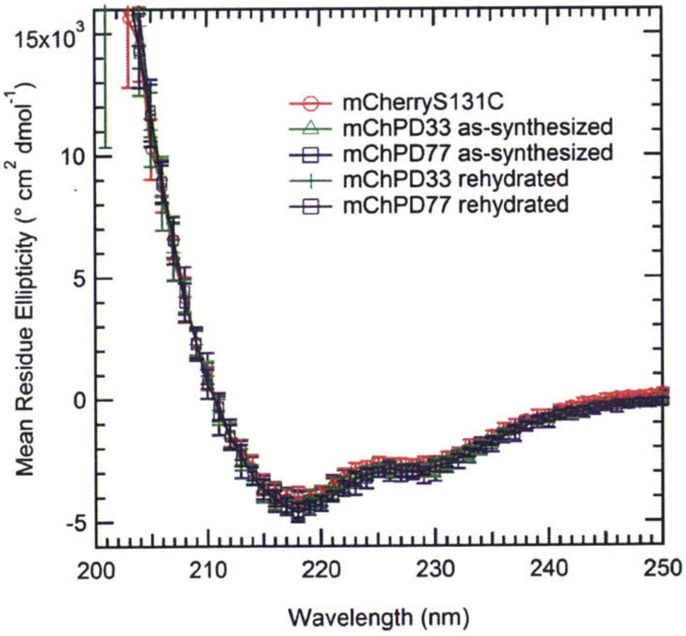

Figure 5-11. CD spectra of mCherryS131C and bioconjugates measured at 25 °C. mCherryS131C is measured in 20 mM Tris Cl (pH 8.0), and the bioconjugates are measured in

50 mM NaCl solution. Signal from 20 mM Tris Cl (pH 8.0) is subtracted from mCherryS131C data, and signal from 50 mM NaCl solution is subtracted from bioconjugate data.

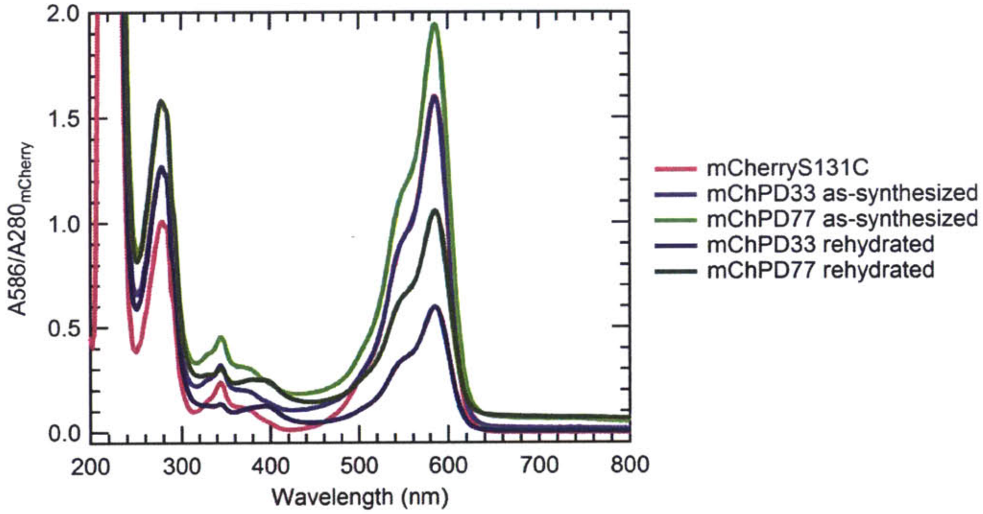

Figure 5-12. UV-vis spectra of mCherryS131C, mChPD33 conjugate, and mChPD77 conjugate. Protein activity of bioconjugates is analyzed by accounting for PDMAPS absorption at 280 nm with molar attenuation coefficients 8,190 M^{-1} cm^{-1} and 9,715 M^{-1} cm^{-1} for PDMAPS 33 kg/mol and 77 kg/mol polymers, respectively. The signal is normalized using an estimated absorbance of mCherry at 280 nm ($A280_{mCherry}$). Plot of $A586/A280_{mCherry}$ show that 98% of mCherry activity is preserved in mChPD33. The activity of mCherry in mChPD77 conjugate is estimated to be 109% of the original mCherry activity. mChPD33 and mChPD77 retain 38% and 54% of activity of as-synthesized conjugates after drying and rehydration after accounting for polymer absorption.

Table 5-2. Scattering length density of each component calculated at 8 keV and 12 keV from https://www.ncnr.nist.gov/resources/activation/

	Compound Formula	**Mass density (g/cm^3)**	**X-ray SLD (real part) (10^{-6} Å^2)**
mCherryS131C	$C_{1250}H_{1915}N_{341}O_{377}S_{12}$	1.35	12.245
PDMAPS	$C_{11}H_{21}NO_5S$	1.37	12.521
Water	H2O	1.00	9.444

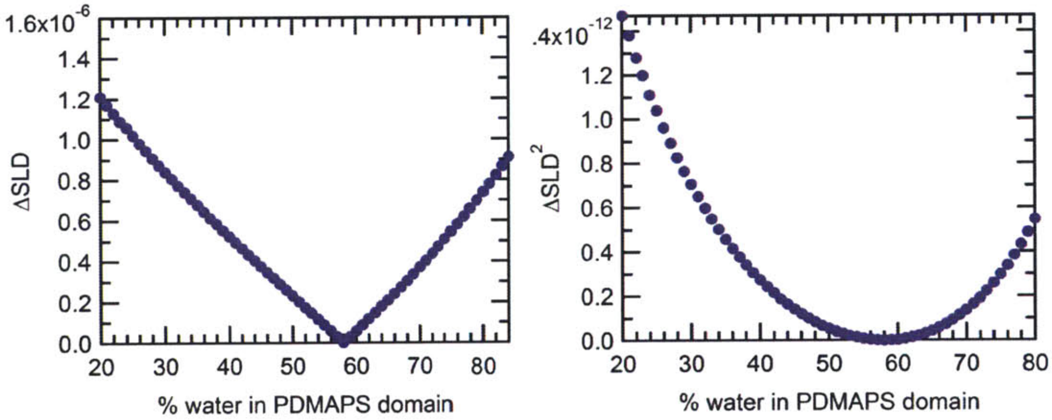

Figure 5-13. A plot of calculated X-ray scattering contrast (ΔSLD) and ΔSLD^2 as water distribution changes.

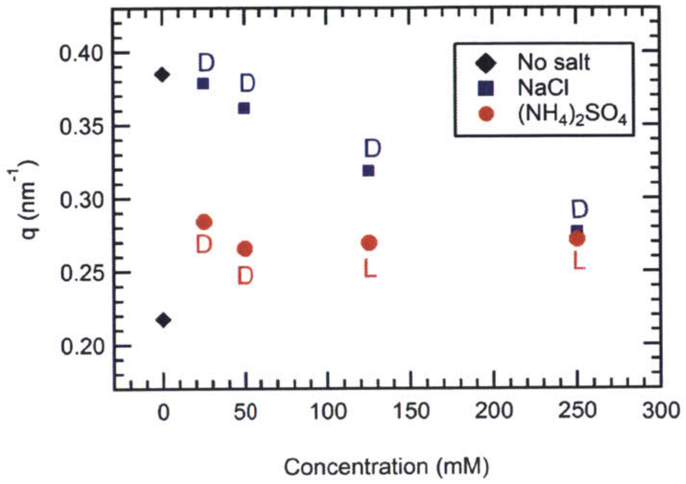

Figure 5-14. Peak positions at the maximum intensity as a function of salt concentrations of mChPD33 bioconjugate at 50 wt.%. Phase formed at each point is indicated as a letter, D denoting disordered phase, and L denoting a lamellar phase. The first two peaks from mChPD33 in pure water are indicated in black diamond markers.

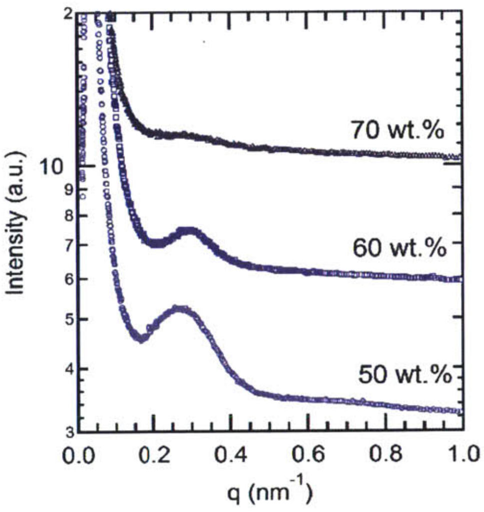

Figure 5-15. SAXS curves of mChPD33 solutions in the presence of 250 mM NaCl.

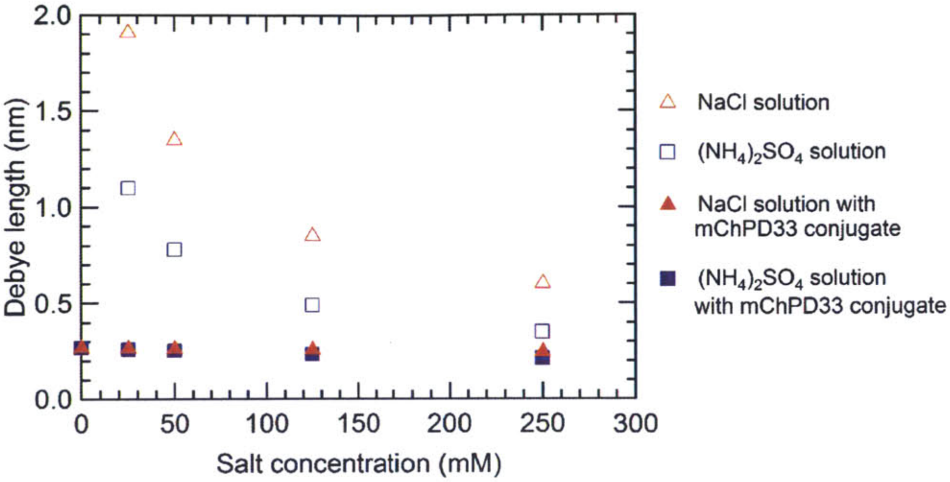

Figure 5-16. The Debye lengths in bioconjugate solutions in the presence of either NaCl or $(NH_4)_2SO_4$.

5.7 References

(1) Heller, A. Electrical Connection of Enzyme Redox Centers to Electrodes. *J. Phys. Chem.* **1992**, *96*, 3579–3587.

(2) Yehezkeli, O.; Yan, Y.-M.; Baravik, I.; Tel-Vered, R.; Willner, I. Integrated Oligoaniline-Cross-Linked Composites of Au Nanoparticles/Glucose Oxidase Electrodes: A Generic Paradigm for Electrically Contacted Enzyme Systems. *Chem. – A Eur. J.* **2009**, *15*, 2674–2679.

(3) Minteer, S. D.; Liaw, B. Y.; Cooney, M. J. Enzyme-Based Biofuel Cells. *Curr. Opin. Biotechnol.* **2007**, *18*, 228–234.

(4) Leech, D.; Kavanagh, P.; Schuhmann, W. Enzymatic Fuel Cells: Recent Progress. *Electrochim. Acta* **2012**, *84*, 223–234.

(5) Karyakin, A. A.; Morozov, S. V; Karyakina, E. E.; Varfolomeyev, S. D.; Zorin, N. A.; Cosnier, S. Hydrogen Fuel Electrode Based on Bioelectrocatalysis by the Enzyme Hydrogenase. *Electrochem. commun.* **2002**, *4*, 417–420.

(6) Das, R.; Kiley, P. J.; Segal, M.; Norville, J.; Yu, A. A.; Wang, L.; Trammell, S. A.; Reddick, L. E.; Kumar, R.; Stellacci, F.; *et al.* Integration of Photosynthetic Protein Molecular Complexes in Solid-State Electronic Devices. *Nano Lett.* **2004**, *4*, 1079–1083.

(7) Drevon, G. F.; Russell, A. J. Irreversible Immobilization of Diisopropylfluorophosphatase in Polyurethane Polymers. *Biomacromolecules* **2000**, *1*, 571–576.

(8) Russell, A. J.; Berberich, J. A.; Drevon, G. F.; Koepsel, R. R. Biomaterials for Mediation of Chemical and Biological Warfare Agents. *Annu. Rev. Biomed. Eng.* **2003**, *5*, 1–27.

(9) Olsen, B. D. Self-Assembly of Globular-Protein-Containing Block Copolymers. *Macromol. Chem. Phys.* **2013**, *214*, 1659–1668.

(10) Thomas, C. S.; Glassman, M. J.; Olsen, B. D. Solid-State Nanostructured Materials from

Self-Assembly of a Globular Protein-Polymer Diblock Copolymer. In *ACS Nano*; American Chemical Society, 2011; Vol. 5, pp. 5697–5707.

(11) Thomas, C. S.; Xu, L.; Olsen, B. D. Kinetically Controlled Nanostructure Formation in Self-Assembled Globular Protein–Polymer Diblock Copolymers. *Biomacromolecules* **2012**, *13*, 2781–2792.

(12) Lam, C. N.; Olsen, B. D. Phase Transitions in Concentrated Solution Self-Assembly of Globular Protein–polymer Block Copolymers. *Soft Matter* **2013**, *9*, 2393.

(13) Chang, D.; Lam, C. N.; Tang, S.; Olsen, B. D. Effect of Polymer Chemistry on Globular Protein–polymer Block Copolymer Self-Assembly. *Polym. Chem.* **2014**, *5*, 4884–4895.

(14) Thomas, C. S.; Olsen, B. D. Coil Fraction-Dependent Phase Behaviour of a Model Globular Protein–polymer Diblock Copolymer. *Soft Matter* **2014**, *10*, 3093–3102.

(15) Lam, C. N.; Kim, M.; Thomas, C. S.; Chang, D.; Sanoja, G. E.; Okwara, C. U.; Olsen, B. D. The Nature of Protein Interactions Governing Globular Protein–Polymer Block Copolymer Self-Assembly. *Biomacromolecules* **2014**, *15*, 1248–1258.

(16) Huang, A.; Qin, G.; Olsen, B. D. Highly Active Biocatalytic Coatings from Protein-Polymer Diblock Copolymers. *ACS Appl. Mater. Interfaces* **2015**, *7*, 14660–14669.

(17) Cho, W. K.; Kong, B.; Choi, I. S. Highly Efficient Non-Biofouling Coating of Zwitterionic Polymers: Poly((3-(methacryloylamino)propyl)-dimethyl(3-Sulfopropyl)ammonium Hydroxide). *Langmuir* **2007**, *23*, 5678–5682.

(18) Vaisocherová, H.; Yang, W.; Zhang, Z.; Cao, Z.; Cheng, G.; Piliarik, M.; Homola, J.; Jiang, S. Ultralow Fouling and Functionalizable Surface Chemistry Based on a Zwitterionic Polymer Enabling Sensitive and Specific Protein Detection in Undiluted Blood Plasma. *Anal. Chem.* **2008**, *80*, 7894–7901.

(19) Cheng, G.; Li, G.; Xue, H.; Chen, S.; Bryers, J. D.; Jiang, S. Zwitterionic Carboxybetaine Polymer Surfaces and Their Resistance to Long-Term Biofilm Formation. *Biomaterials* **2009**, *30*, 5234–5240.

(20) Quintana, R.; Gosa, M.; Jańczewski, D.; Kutnyanszky, E.; Vancso, G. J. Enhanced Stability of Low Fouling Zwitterionic Polymer Brushes in Seawater with Diblock Architecture. *Langmuir* **2013**, *29*, 10859–10867.

(21) Zhai, G.; Toh, S. C.; Tan, W. L.; Kang, E. T.; Neoh, K. G.; Huang, C. C.; Liaw, D. J. Poly(vinylidene Fluoride) with Grafted Zwitterionic Polymer Side Chains for Electrolyte-Responsive Microfiltration Membranes. *Langmuir* **2003**, *19*, 7030–7037.

(22) Sun, Q.; Su, Y.; Ma, X.; Wang, Y.; Jiang, Z. Improved Antifouling Property of Zwitterionic Ultrafiltration Membrane Composed of Acrylonitrile and Sulfobetaine Copolymer. *J. Memb. Sci.* **2006**, *285*, 299–305.

(23) SHI, Q.; SU, Y.; ZHAO, W.; LI, C.; HU, Y.; JIANG, Z.; ZHU, S. Zwitterionic Polyethersulfone Ultrafiltration Membrane with Superior Antifouling Property. *J. Memb. Sci.* **2008**, *319*, 271–278.

(24) Yang, Y.-F.; Li, Y.; Li, Q.-L.; Wan, L.-S.; Xu, Z.-K. Surface Hydrophilization of Microporous Polypropylene Membrane by Grafting Zwitterionic Polymer for Anti-Biofouling. *J. Memb. Sci.* **2010**, *362*, 255–264.

(25) Keefe, A. J.; Jiang, S. Poly(zwitterionic)protein Conjugates Offer Increased Stability without Sacrificing Binding Affinity or Bioactivity. *Nat. Chem.* **2011**, *4*, 59–63.

(26) Cao, Z.; Jiang, S. Super-Hydrophilic Zwitterionic Poly(carboxybetaine) and Amphiphilic Non-Ionic Poly(ethylene Glycol) for Stealth Nanoparticles. *Nano Today* **2012**, *7*, 404–413.

(27) Shao, Q.; Jiang, S. Molecular Understanding and Design of Zwitterionic Materials. *Adv.*

Mater. **2015**, *27*, 15–26.

(28) Kane, R. S.; Deschatelets, P.; Whitesides, G. M. Kosmotropes Form the Basis of Protein-Resistant Surfaces. *Langmuir* **2003**, *19*, 2388–2391.

(29) Wu, J.; Lin, W.; Wang, Z.; Chen, S.; Chang, Y. Investigation of the Hydration of Nonfouling Material Poly(sulfobetaine Methacrylate) by Low-Field Nuclear Magnetic Resonance. *Langmuir* **2012**, *28*, 7436–7441.

(30) Leng, C.; Hung, H.-C.; Sieggreen, O. A.; Li, Y.; Jiang, S.; Chen, Z. Probing the Surface Hydration of Nonfouling Zwitterionic and Poly(ethylene Glycol) Materials with Isotopic Dilution Spectroscopy. *J. Phys. Chem. C* **2015**, *119*, 8775–8780.

(31) Leng, C.; Hung, H.-C.; Sun, S.; Wang, D.; Li, Y.; Jiang, S.; Chen, Z. Probing the Surface Hydration of Nonfouling Zwitterionic and PEG Materials in Contact with Proteins. *ACS Appl. Mater. Interfaces* **2015**, *7*, 16881–16888.

(32) Ebbinghaus, S.; Kim, S. J.; Heyden, M.; Yu, X.; Heugen, U.; Gruebele, M.; Leitner, D. M.; Havenith, M. An Extended Dynamical Hydration Shell around Proteins. *Proc. Natl. Acad. Sci. U. S. A.* **2007**, *104*, 20749–20752.

(33) Lantman, C. W.; MacKnight, W. J.; Lundberg, R. D. Structural Properties of Ionomers. *Annu. Rev. Mater. Sci.* **1989**, *19*, 295–317.

(34) Grady, B. P. Review and Critical Analysis of the Morphology of Random Ionomers across Many Length Scales. *Polym. Eng. Sci.* **2008**, *48*, 1029–1051.

(35) Ruzette, A.-V. G.; Soo, P. P.; Sadoway, D. R.; Mayes, A. M. Melt-Formable Block Copolymer Electrolytes for Lithium Rechargeable Batteries. *J. Electrochem. Soc.* **2001**, *148*, A537.

(36) Epps, T. H.; Bailey, T. S.; Pham, H. D.; Bates, F. S. Phase Behavior of Lithium Perchlorate-Doped Poly(styrene- B -Isoprene- B -Ethylene Oxide) Triblock Copolymers. *Chem. Mater.* **2002**, *14*, 1706–1714.

(37) Wang, J.-Y.; Chen, W.; Russell, T. P. Ion-Complexation-Induced Changes in the Interaction Parameter and the Chain Conformation of PS- B -PMMA Copolymers. *Macromolecules* **2008**, *41*, 4904–4907.

(38) Young, W.-S.; Epps, T. H. Salt Doping in PEO-Containing Block Copolymers: Counterion and Concentration Effects. *Macromolecules* **2009**, *42*, 2672–2678.

(39) Wanakule, N. S.; Virgili, J. M.; Teran, A. A.; Wang, Z.-G.; Balsara, N. P. Thermodynamic Properties of Block Copolymer Electrolytes Containing Imidazolium and Lithium Salts. *Macromolecules* **2010**, *43*, 8282–8289.

(40) Park, M. J.; Balsara, N. P. Phase Behavior of Symmetric Sulfonated Block Copolymers. *Macromolecules* **2008**, *41*, 3678–3687.

(41) Stewart-Sloan, C. R.; Olsen, B. D. Protonation-Induced Microphase Separation in Thin Films of a Polyelectrolyte-Hydrophilic Diblock Copolymer. *ACS Macro Lett.* **2014**, *3*, 410–414.

(42) Boutris, C.; Chatzi, E. G.; Kiparissides, C. Characterization of the LCST Behaviour of Aqueous poly(N-Isopropylacrylamide) Solutions by Thermal and Cloud Point Techniques. *Polymer (Guildf).* **1997**, *38*, 2567–2570.

(43) Sing, C. E.; Zwanikken, J. W.; Olvera de la Cruz, M. Electrostatic Control of Block Copolymer Morphology. *Nat. Mater.* **2014**, *13*, 694–698.

(44) Sing, C. E.; Zwanikken, J. W.; de la Cruz, M. O. Theory of Melt Polyelectrolyte Blends and Block Copolymers: Phase Behavior, Surface Tension, and Microphase Periodicity. *J. Chem. Phys.* **2015**, *142*, 034902.

(45) Svergun, D. I.; Richard, S.; Koch, M. H. J.; Sayers, Z.; Kuprin, S.; Zaccai, G. Protein Hydration in Solution: Experimental Observation by X-Ray and Neutron Scattering. *Proc. Natl. Acad. Sci.* **1998**, *95*, 2267–2272.

(46) Merzel, F.; Smith, J. C. Is the First Hydration Shell of Lysozyme of Higher Density than Bulk Water? *Proc. Natl. Acad. Sci.* **2002**, *99*, 5378–5383.

(47) Breretont, G.; Vilgis, T. a. Compatibility and Phase Behavior in Charged Polymer Systems and Ionomers. *Macromolecules* **1990**, *23*, 2044–2049.

(48) Qin, G.; Glassman, M. J.; Lam, C. N.; Chang, D.; Schaible, E.; Hexemer, A.; Olsen, B. D. Topological Effects on Globular Protein-ELP Fusion Block Copolymer Self-Assembly. *Adv. Funct. Mater.* **2015**, *25*, 729–738.

(49) Schulz, D. N.; Peiffer, D. G.; Agarwal, P. K.; Larabee, J.; Kaladas, J. J.; Soni, L.; Handwerker, B.; Garner, R. T. Phase Behaviour and Solution Properties of Sulphobetaine Polymers. *Polymer (Guildf).* **1986**, *27*, 1734–1742.

(50) Moon, Y. U.; Curtis, R. A.; Anderson, C. O.; Blanch, H. W.; Prausnitz, J. M. Protein—Protein Interactions in Aqueous Ammonium Sulfate Solutions. Lysozyme and Bovine Serum Albumin (BSA). *J. Solution Chem.* **2000**, *29*, 699–718.

(51) Ball, P.; Hallsworth, J. E. Water Structure and Chaotropicity: Their Uses, Abuses and Biological Implications. *Phys. Chem. Chem. Phys.* **2015**, *17*, 8297–8305.

(52) Lowe, A. B.; McCormick, C. L. Synthesis and Solution Properties of Zwitterionic Polymers. *Chem. Rev.* **2002**, *102*, 4177–4189.

(53) Shu, X.; Shaner, N. C.; Yarbrough, C. A.; Tsien, R. Y.; Remington, S. J. Novel Chromophores and Buried Charges Control Color in mFruits. *Biochemistry* **2006**, *45*, 9639–9647.

Chapter 6. Conclusions

6.1 Summary

This thesis built upon the knowledge of the self-assembly of a globular protein-polymer diblock copolymer composed of mCherry and PNIPAM previously established in the research group and explored the effect of polymer block chemistry, electrostatic interactions in solution, and the self-assembly in thin films. It began with describing the effect of polymer block chemistry on the phase behavior of mCherry-polymer bioconjugates in concentrated aqueous solution. Two new polymer blocks, PHPA and POEGA, which were capable of hydrogen bonding interactions were selected to modulate interactions between protein and polymer. It was discovered that change in polymer block chemistry resulted in different types of nanostructures and different order-disorder concentrations (C_{ODT}). mCherry-*b*-PHPA and mCherry-*b*-POEGA displayed higher C_{ODT} at all coil fractions compared to previously studied mCherry-*b*-PNIPAM, which suggested weaker segregation strengths between these polymers and mCherry compared to that between PNIPAM and mCherry. The nanostructure observed between thermotropic transitions from lamellae to hexagonally packed cylinders for these conjugates was a double gyroid structure with $Ia\bar{3}d$ symmetry as opposed to hexagonally perforated lamellae formed by mCherry-*b*-PNIPAM. The observation of a double gyroid structure in the weakly segregated bioconjugates was consistent with the fact that hexagonally perforated lamellae are at least kinetically preferred over a double gyroid structure in block copolymers with strong segregation. Common phase behaviors among the hydrogen bonding capable neutral polymer blocks were discovered, including a re-entrant disordering transition at high concentration. The disordered phase at high concentration was found to be birefringent, which suggested the presence of directional orientation. The nematic liquid crystalline ordering could be attributed to the excluded volume effect arising from the cylindrical mCherry block despite its low aspect ratio. The degree of hydration of different polymer blocks relative to mCherry domain was quantified using SANS. PHPA and POEGA were slightly more hydrated than mCherry at low temperature at which both blocks are well-solvated, but their differences were not statistically significant based on the analysis method employed.

The knowledge of the concentrated solution phase behavior was applied next to the self-assembly of the bioconjugates in thin films. mCherry-*b*-POEGA was selected for the study due to the mechanical contrast between the two blocks for AFM imaging. Due to limited annealing conditions as well as activity loss of proteins after annealing, understanding the nanostructures of as-cast films, which was largely affected by processing conditions, was critical. Films were prepared using a flow coater, and it was found that the POEGA block preferentially wetted the air-film interface under the solvent drying condition, which was advantageous because interactions of proteins at an air-film interface or a solid support often lead to denaturation and inactivation. The relative humidity of the environment, which affects the evaporation rate, and coating speed were found to be important parameters controlling long range order in bioconjugate thin films. Well-ordered hexagonally packed cylinders with the (10) plane aligned parallel to the substrate were observed in films prepared under 80% relative humidity, while parallel cylinders with the (10) plane randomly oriented with respect to the substrate were observed in films prepared under <25% relative humidity. Also, a high coating speed was found to result in a hexagonally packed cylindrical structure with a much longer range order, whereas a slow coating speed hindered crystal growth. This study identified the important kinetic processing parameters necessary in the preparation of well-ordered protein-polymer bioconjugate films

In the last study, the effect of electrostatic interactions on protein-polymer conjugate self-assembly was studied using a zwitterionic polymer block, PDMAPS. While mCherry-*b*-PDMAPS conjugates were expected to have a greater window of ordered region in the phase diagram due to the resistance to nonspecific protein adsorption of a zwitterionic polymer block, which makes it a promising material for antifouling coating and biomedical applications, it was also hypothesized that the reduced charge asymmetry between mCherry and PDMAPS would reduce the tendency toward microphase separation. The charge asymmetry was confirmed to be one of the governing parameters in the self-assembly based on the observation of weaker segregation between mCherry and PDMAPS, demonstrated by a high C_{ODT} and a very narrow ordered region in the phase diagram. Salt studies further demonstrated the role of electrostatics in the self-assembly. Attractive electrostatic interactions between PDMAPS were found to play a critical role in the microphase separation based on the fact that the ordering was disrupted even at a very low concentration of NaCl. Addition of a kosmotropic salt, $(NH_4)_2SO_4$, was found to result in an initial disordering followed by a transition to a lamellar structures as the salt concentration increased, which was attributed to the protein-stabilizing nature of the salt.

The results in this thesis have contributed to our understanding of the self-assembly of globular protein-polymer bioconjugates in bulk and in thin films with a goal to improve current protein nanopatterning technologies. The effects of polymer block chemistry, charge cohesion, and electrostatic interactions on the self-assembly of protein-polymer bioconjugates in concentrated solution were studied. This thesis also provides guidance for the preparation of well-ordered bioconjugate thin films, which is essential for numerous future applications.

6.2 Outlook

This thesis, along with the works of colleagues, reveals many interesting areas for future investigation. First, a re-entrant disordering transition at high concentration has been consistently observed in all mCherry-polymer bioconjugates, which is not predicted in traditional theories of synthetic diblock copolymers. The re-entrant disordering transition limits the formation of nanostructures in solid materials by resulting in a highly disordered solid if kinetic effects are not properly understood and controlled. Understanding the fundamental physics governing the re-entrant transition would be valuable, and the knowledge can be used to identify strategies to prevent or minimize the re-entrant behavior.

Among many factors governing the self-assembly of protein-polymer conjugates that have been identified, the cylindrical shape of mCherry or a similar fluorescent protein, eGFP, arising from their β-barrel structure, has been observed to lead to better well-ordered nanostructures compared to enzymes with an irregular shape, such as myoglobin or P450. It has been shown in the literature that the shape of a particle affects the self-assembly due to various entropic considerations, including excluded volume interactions and depletion forces. Although defining a parameter that can describe the numerous different shapes of proteins is not trivial and is further complicated by the protein shape being coupled with anisotropic surface interactions, a modelling study would reveal the relative importance of geometrical criteria in the self-assembly of protein-polymer block copolymers.

In the continuation of studies on protein-polymer interactions, it would be interesting to study the phase behavior of linear protein-protein or linear protein-polymer diblock copolymers in comparison to the phase behavior of globular protein-polymer block copolymers described in this thesis. Interactions between protein and polymer are complex due to the heterogeneous primary sequence, anisotropy, and globular shape of proteins. Simply denaturing mCherry may not be sufficient to construct a linear protein block, as the denaturation would reveal internal hydrophobic residues which do not participate in interactions in the native state. Careful design of a linear polypeptide which can mimic the composition of the surface amino acid residues of mCherry will help decouple the effect of the globular shape and anisotropy of the protein from the chemical incompatibility between protein and polymer. Without a denaturing transition, this system will also allow thermal annealing to achieve a state closer to the true equilibrium.

Finally, to utilize the full potential of nanostructured polymer domains and demonstrate the role of various nanostructures within materials on the protein activity, incorporation of polymer blocks that can have synergistic effects with an enzyme would be interesting. For example, conjugated polymers can aid charge transfer of a redox protein in self-assembled materials. A polymer bearing chemical moieties that can be crosslinked using an external stimulus such as UV light would allow one to study the transport properties of the materials and activity of solid materials more easily.

Self-assembly of protein-polymer bioconjugates is a promising technology for protein nanopatterning, which results in nanostructured materials with a high density of proteins. Knowledge of the physics and thermodynamics governing their self-assembly is essential for the rational design of globular protein-polymer block copolymers and control over their nanostructures targeted for specific materials applications. This technology will allow catalytic devices to achieve a greater performance. The results presented in this thesis will help guide future development of novel protein-polymer systems for applications.

Appendix A. List of Abbreviations

AFM	Atomic force microscopy
AgBe	Silver behenate
AIBN	Azobisisobutyronitrile
BHT	Butylated hydroxytoluene
BME	β-mercaptoethanol
$CDCl_3$	Deuterated chloroform
CPP	4-cyano-4-(phenylcarbonothioylthio)pentanoic acid
CTA	Chain transfer agent
CD	Circular dichroism
C_{ODT}	Order-disorder transition concentration
CV	Colume volume
Đ	Dispersity of a polymer
DCC	*N,N'*-dicyclohexylcarbodiimide
DMAP	4-dimethylaminopyridine
DMF	Dimethylformamide
DP	Degree of polymerization
DPLS	Depolarized light scattering
DSC	Differential scanning calorimetry
EMP	2-ethylsulfanylthiocarbonyl sulfanyl-2-methylpropionic acid
FPLC	Fast protein liquid chromatography
GISAXS	Grazing incidence small angle X-ray scattering
GPC	Gel permeation chromatography
HQ	Hydroquinone
Imide	exo-3a,4,7,7a-tetrahydro-2-(3-hydroxypropyl)-4,7-epoxy-14-isoindole-1,3(2H)-dione
LC-MS	Liquid chromatography–mass spectrometry
MEA	2-methoxyethyl acrylate
MEEA	2-(2-methoxyethoxy)ethyl acrylate
M_n	Average molar mass of a polymer
NMR	Nuclear magnetic resonance
PDMAPS	Poly(3-[*N*-(2-methacroyloyethyl)-*N,N*-dimethylammonio]propane sulfonate)
PEG	Poly(ethylene glycol)
PETG	Polyethylene terephthalate glycol-modified
PHPA	Poly(hydroxypropyl acrylate)
PNIPAM	Poly(*N*-isopropylacrylamide)
POEGA	Poly(oligoethylene glycol acrylate)
RAFT	Reversible addition-fragmentation chain-transfer
SANS	Small-angle neutron scattering
SAXS	Small-angle X-ray scattering
SDD	Sample to detector distance
SDS-PAGE	Sodium dodecyl sulfate polyacrylamide gel electrophoresis
TLC	Thin layer chromatography
T_t	Thermal transition temperature

VA-044	2,2'-Azobis[2-(2-imidazolin-2-yl)propane]dihydrochloride

Appendix B. List of Buffers and the Components Used for Synthesis and Purification of mCherryS131C and Bioconjugates

<u>Lysis buffer</u>

3.45 g $NaH_2PO_4 \cdot H2O$ (50 mM)
8.77 g NaCl (300 mM)
0.34 g imidazole (10 mM)
352 μL BME (10 mM)
500 mL water
pH = 8.0

<u>Wash buffer (reducing condition for mCherryS131C purification)</u>

3.45 g $NaH_2PO_4 \cdot H2O$ (50 mM)
8.77 g NaCl (300 mM)
0.56 g imidazole (20 mM)
352 μL BME (10 mM)
500 mL water
pH = 8.0

<u>Elution buffer (reducing condition for mCherryS131C purification)</u>

3.45 g $NaH_2PO_4 \cdot H2O$ (50 mM)
8.77 g NaCl (300 mM)
8.50 g imidazole (250 mM)
352 μL BME (10 mM)
500 mL water
pH = 8.0

<u>Elution buffer (native condition for bioconjugate purification)</u>

3.45 g $NaH_2PO_4 \cdot H2O$ (50 mM)
8.77 g NaCl (300 mM)
8.50 g imidazole (250 mM)
500 mL water
pH = 8.0